SYNTHESIS & CHARACTERIZATION OF MESOPOROUS $LiCoO_2$ and $LiMn_2O_4$ THIN FILMS

A THESIS SUBMITTED TO

THE GRADUATE SCHOOL OF ENGINEERING AND SCIENCE

OF BILKENT UNIVERSITY

IN PARTIAL FULFILLMENT OF THE REQUIREMENTS FOR

THE DEGREE OF

MASTER OF SCIENCE

IN

CHEMISTRY

By

Gülbahar Saat

January 2017

SYNTHESIS & CHARACTERIZATION OF MESOPOROUS $LiCoO_2$ and $LiMn_2O_4$ THIN FILMS

By Gülbahar Saat

January 2017

We certify that we have read this thesis and that in our opinion it is fully adequate, in scope and in quality, as a thesis for the degree of Master of Science.

_____

Ömer Dağ (Advisor)

_____

Ferdi Karadaş

_____

Emren Nalbant Esentürk

Approved for the Graduate School of Engineering and Science:

_____

Ezhan Karaşan

Director of the Graduate School

ABSTRACT

SYNTHESIS & CHARACTERIZATION OF MESOPOROUS $LiCoO_2$ and $LiMn_2O_4$ THIN FILMS

Gülbahar Saat
M.S. in Chemistry
Advisor: Ömer Dağ
January 2017

This work focuses on the adaptation of molten salt assisted self-assembly (MASA) method for the synthesis and characterization of mesoporous $LiCoO_2$ and $LiMn_2O_4$ materials without a polymerizing agent in the media. The MASA process is a new method to synthesize mesoporous thin films and monoliths. Fresh gel and calcined solid samples were characterized by using XRD, Raman, N_2 sorption, FTIR POM, SEM, TEM and UV-Vis measurements.

The first step of the process involves the preparation of clear solutions that contain two hydrated salts, $LiNO_3.xH_2O$ and $Co(NO_3)_2.6H_2O$ (or $Mn(NO_3)_2.6H_2O$), CTAB (cethyltrimethylammonium bromide, ionic surfactant) (or CTAN), 10- lauryl ether ($C_{12}EO_{10}$, ionic surfactant) and ethanol (or H_2O) as volatile solvents. Additionally, HNO_3 is needed in the case of $LiMn_2O_4$ to prevent formation of $[Mn(OH)_2(H_2O)_4](s)$ complex during and/or before the assembly process.

The clear solutions are spin coated over various substrates to produce the salt-surfactant LLC mesophase that resists to high temperature treatments (300-550 ^oC) in air to form first examples of mesoporous metal lithiates. Thesis is designed to give the insights on how to change several parameters that control the features like purity, pore size, surface area and crystallinity of the $LiCoO_2$ and

$LiMn_2O_4$ mesostructures by determining solvent type, thickness of the LLC film, acid amount, salt uptake, calcination temperature, calcination time and surfactant used for the synthesis.

Ethanol was determined to be a good solvent to prepare the clear solutions. The samples, prepared by spin coating gave better results than the ones prepared by drop casting to obtain uniform pores with less side products. Addition of HNO_3 has no effect on side product formation in the synthesis of $LiCoO_2$ but it is vital to obtain a stable, homogenous solution in the case of $LiMn_2O_4$ preparation. $LiCoO_2$ samples, prepared using CTAB are semicrystalline at lower temperatures and stable up to 550 ^oC but it undergoes decomposition to Co_3O_4 and Li_2O at higher temperatures. Presence of CTAB in the reaction media has a positive effect on the uniformity pores. However; due to the role of Br^- ion on formation of side products, CTAN has been used for further experimentation. Thin films of the calcined samples showed small angle diffraction corresponds to preserved order of the mesophase during calcination. Mesoporous pure HT- $LiCoO_2$ synthesized with MASA is the first example in the literature, having a 65 m^2/g specific surface area and 15 nm pore size. Moreover; mesoporous pure $LiMn_2O_4$ could be obtained both using CTAB and CTAN with 82 m^2/g specific surface area and 11 nm pore size.

Keywords: ***Molten Salt Assisted Self-assembly, Mesoporous Thin Films, Lithium Ion Batteries, $LiCoO_2$, $LiMn_2O_4$***

ÖZET

MEZOGÖZENEKLİ $LiCoO_2$ ve $LiMn_2O_4$ İNCE FİLMLERİN SENTEZİ VE KARAKTERİZASYONU

Gülbahar Saat
Kimya, Yüksek Lisans
Tez Danışmanı: Ömer Dağ
Ocak 2017

Bu çalışma; tuz ve yüzey aktiflerin kendiliğinden oluşumu olan EYKO (eriyik tuz yardımlı kendiliğinden oluşma) metodunun ortamda bir polimerizasyon aracı olmadan mezogözenekli $LiCoO_2$ ve $LiMn_2O_4$ ince filmlerin sentezi ve karakterizasyonuna uyarlanmasına odaklanmıştır. EYKO işlemi, ince filmleri ve monolitleri sentezlemek için yeni bir metottur. Sıvı kristal faz ve yakılmış örnekler x- ışını kırınımı, XRD, Raman ve FTIR spektroskopi, N_2 sorpsiyon ve POM, SEM, TEM görüntüleme ve UV-Görünür bölge soğurma spektroskopi cihazları kullanılarak karakterize edilmiştir.

Bu işlemin ilk adımı; içinde sulu tuzlar olan $LiNO_3.xH_2O$ ve $Co(NO_3)_2.6H_2O$ (yada $Mn(NO_3)_2.6H_2O$), CTAB (setiltrimetilamonyum bromür, iyonlu yüzey aktif madde) (yada CTAN, setiltrimetilamonyum nitrat), 10- laurik eter ($C_{12}EO_{10}$, nötür yüzey aktif madde) ve uçucu çözücüler olarak etanol (yada H_2O) içeren berrak çözeltiler hazırlamaktır. Buna ek olarak; $LiMn_2O_4$ sentezi için hazırlanan çözeltide $[Mn(OH)_2(H_2O)_4](s)$ kompleks oluşumunu önlemek için HNO_3'e ihtiyaç duyulur. Sonra çözelti döngülü kaplama ile cam alttaş üzerine kaplanarak fazla çözücünün uçmasıyla yüksek sıcaklık (300 ile 550 ^oC) uygulamalarına maruz bırakılarak, mezogözenekli metal lithiates'in ilk örnekleri sentezlenir. Bu tez; mezogözenekli

$LiCoO_2$ ve $LiMn_2O_4$'ın saflık, yüzey alanı, duvarların kristalliği gibi özelliklerinin, kullanılan çözücü, film kalınlığı, asit miktarı, tuz miktarı, yanma sıcaklığı ve süresi ve kullanılan yüzey aktiflerin değişimi ile nasıl kontrol edilebileceğini anlatmaktadır.

Çözelti hazırlama kısmında; yüksek çözünürlüğü ve sentez verimliliği açısından çözücü olarak etanol tercih edilmiştir. Döngülü kaplama ile hazırlanan örneklerde damlatılarak yayma yöntemi ile hazırlananlara kıyasen daha düzenli gözenekler ve daha az miktarda yan ürün oluşumu gözlendi. $LiCoO_2$ sentezinde yan ürün oluşumunda HNO_3'ün herhangi bir etkisinin olmadığı belirlendi. Fakat $LiMn_2O_4$'ın sentezinde kararlı ve homojen bir çözelti elde etmek için gerekli olduğu saptandı. CTAB ile hazırlanan . $LiCoO_2$ örnekleri düşük sıcaklıklarda yarı kristal bir yapı gösterir, mezoyapı 550 ^oC'ye kadar dayanıklıdır, sonrasında bozunarak Co_3O_4 ve Li_2O'e parçalanır. CTAB'ın mezogözenekli $LiCoO_2$ sentezinde düzenli gözenek oluşumundaki etkisi gözlemlenmiştir. Ama Br^- iyonunun yan ürün oluşumundaki etkisinden dolayı; ilerki deneylerde CTAN sentezlenip kullanılmıştır. Kalsine edilmiş ince film örneklerinin düşük açılı XRD ölçümlerinde kırınım göstermesi, yanma süresince mezoyapının düzenliliğinin korunduğunu göstermektedir. EYKO metodunun uyarlanmasıyla sentezlenen mezogözenekli HT- $LiCoO_2$, yanma sıcaklığı 900 ^oC'den 300 ^oC'ye kadar düşürülebildiği için yüzey alanı 65 m^2/g ve gözenek boyutu 15 nm olan literatürdeki ilk örnektir. Ayrıca, 82 m^2/g yüzey alanı ve 11 nm gözenek boyutuna sahip mezogözenekli saf $LiMn_2O_4$ hem CTAB hem de CTAN kullanılarak sentezlenebilmektedir.

Anahtar sözcükler: ***Eriyik Tuz Yardımlı Kendiliğinden Oluşma, EYKO, Mezogözenekli İnce Filmler, Lityum İyon Pilleri, $LiCoO_2$, $LiMn_2O_4$***

Acknowledgement

First and foremost, I would like to thank to my advisor Prof. Ömer Dağ for his excellent supervision and guidance throughout my studies.

I would like to express my sincere appreciations to Fadime Mert Balci and Elif Berna Olutaş for valuable scientific discussions and emotional support.

I want to express my thanks to our group members Muammer Yaman, Nüveyre Canbolat, Ezgi Yılmaz, Tuluhan Olcayto Çolak, Doruk Ergöçmen, Işıl Uzunok and Irmak Karakaya. We shared lots of memories in the Dağ group.

I also wish to acknowledge chemistry department members, Satya Vijaya Kumar, Özge Bayrak, Pınar Alsaç, Ethem Anber, Deniz Gökçeaslan who have provided my memories.

I also would like to acknowledge TUBITAK for financial support.

I am immeasurably indebted to my mom and brother " Hamdi Oğuz" who supported and encouraged me during my graduate study.

I also want to thank my little cutie pie "Azra".

Contents

List of Figures

List of Table

List of Abbreviations

BET: Brunauer-Emmett-Teller

TEOS: tetra ethyl ortho-silicate

FTIR: Fourier Transform Infrared Spectroscopy

IR: Infrared

JCPDS: Joint Committee on Powder Diffraction Standards

LLC: lyotropic liquid crystalline

TMS: Transition Metal Salt

MASA: Molten Salt Assisted Self Assembly

CTAB: Cetyl Trimethyl Ammonium Bromide

CTAN: Cetyl Trimethyl Ammonium Nitrate

OER: Oxygen evolution reaction)

ORR: Oxygen reduction reaction

RT: Room Temperature

HT: High Temperature

LT: Low Temperature

LMO: Lithiated Manganese Oxide

SSA: Specific Surface Area

POM: Polarized Optical Microscopy

EISA: Evaporation-Induced Self-Assembly

WSS: Water Salt Surfactant

SAXS: Small Angle X-ray Scattering

WAXS: Wide Angle X-ray Scattering

Chapter 1

Introduction

1.1 Ordered Mesoporous Materials

Mesoporous materials have drawn attention due to their extensive variety of applications with the discovery of ordered mesoporous silicas (*e.g.* KSW-1, MCM-41) in the 1990s[1, 2]. Mesopores (2-50 nm in diameter) increase the surface area and pore volume in a material that provide an increase in reactive sites, significant interfacial area and size selectivity for molecules[3]. These structural properties offer potential applications in a wide range like adsorption, separation, energy storage and conversion, drug delivery, catalysis, photonics, nanodevices and etc.[4-7].

Depending on the synthesis conditions, silica source or type of surfactant used, many different types of silica mesostructures have been investigated due to controllable hydrolysis and condensation processes of the silica precursors (*e.g.*, TEOS: tetra ethyl ortho-silicate in water) and stability of the resulting mesostructure during calcination[8]. However; pure silica materials have low chemical activities and all the synthesized mesoporous silicas have amorphous walls[9]. As a result of these obstacles, synthesis of ordered non-siliceous mesostructures gain importance.

However; in the case of synthesis of non-siliceous mesoporous materials by using surfactants, the process is hard to control due to the sensitivity of the

precursors to hydrolysis-condensation steps (*e.g.*, metal alkoxides), redox reactions and structural collapse occur as a result of rapid crystallization during calcination at elevated temperatures[10]. These difficulties incline scientists to develop alternative synthesis routes using hard templates.

Over the past few decades; substantial developments have been made in the preparation and application of ordered non-siliceous mesoporous materials[9], [11-13]. For instance; Yang and coworkers in 1998 reported used a soft templating method to produce a series of semi-crystalline mesoporous metal oxides[14]. Ryoo *et. al.* found and developed so called "hard templating method" for the synthesis of ordered mesoporous carbons in early 200s[15-17]. In 2003, Zhu *et. al.* synthesized ordered mesoporous Cr_2O_3 by using hard templating pathway[18]. Grosso and coworkers obtained ordered crystalline mesoporous $SrTiO_3$, $MgTa_2O_6$ and $Co_xTi_{1-x}O_{2-x}$ by using soft templating method in 2004[19].

Among the other non-silica mesoporous materials, ordered mesoporous transition metal oxides are receiving intense interest due to their exclusive applications emerging due to their d-shell electrons being confined to nanosized walls, redox active internal surfaces and connected pore networks[20]. Within the scope of this study; the synthesis methods of ordered mesoporous metal oxides will be covered in detail in the next sections.

1.2 Preparation of Ordered Mesoporous Metal Oxides Using Hard Templates

Hard templating is a millennium old method of metal casting. A rigid, porous object with nm or μm-scale features is called as "template" or "mold"[21]. Generally, a liquid precursor adheres to the surface of the template or fills the

vacancies within the template is called as “cast” in the “mold”. Then, precursor is transformed into a solid-phase material by a series of chemical and thermal treatments. In order to obtain templated, inorganic oxides via sol-gel chemistry, a common mechanism includes the following steps[22];

Step 1: $M\text{-}X + H_2O \rightarrow M\text{-}OH + ROH$, X=Anion (1)

or $M\text{-}OR + H_2O \rightarrow M\text{-}OH + ROH$

Step 2: $M\text{-}OH + XO\text{-}M \rightarrow M\text{-}O\text{-}M + X\text{-}OH$, X=H or R (2)

or $M\text{-}OH + M\text{-}OX \rightarrow M\text{-}(OH)\text{-}M\text{-}OX$, X=H or R

The process is initiated by hydrolysis of the salt or alkoxides. Then, hydroxylated metal species react with other metal centers and go into acid or base catalyzed condensation reactions, followed by oxo- or hydroxo-linkages between metal and metalloid atoms form colloidal oxides(oligomers dispersed in a liquid)[23]. An inorganic framework and a 3-D gel are obtained via further condensation at higher temperatures. Finally, the template is removed by dissolution using an aqueous NaOH or HF solution (for silica templates) or combustion (for carbon templates) to acquire a cast as a hollow replica or the negative replica of the template[24]. Synthetic procedure for the hard templating method for the preparation of mesoporous materials is shown in figure 1[25].

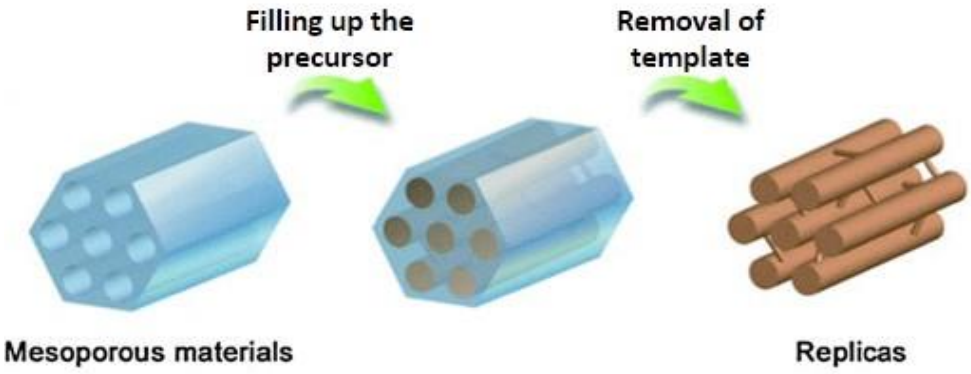

Figure 1: Synthetic route for the hard-templating to prepare porous mesostructures (Copyright © 2008 Wiley. Reprinted with permission from ref[25]).

In the early studies; porous Al_2O_3 membranes obtained by anodic oxidation method were used as a template to produce nanostructures of carbon, metal etc. with a pore size range of 15 to 150 nm by using electrodeposition, Chemical Vapor Deposition or Atomic Layer Deposition methods[25-27]. Then, ordered mesoporous silicas having diverse wall thickness, pore size and pore structure symmetries like hexagonal P6mm (MCM-41, SBA-15, SBA-3), cubic Ia3d (MCM-48, KIT-6, FDU-5), cubic Im3m (SBA-16) and cubic Fm-3m (FDU-12) and mesoporous carbons having symmetries like cubic $I4_132$ (CMK-1) and cubic Pm3n (CMK-3) have been also used as mold materials[13], [16-18], [28, 29].

The pioneering study for preparation of ordered highly crystalline mesoporous transition metal oxides by using hard template was the synthesis of Cr_2O_3 and reported in 2003 by Zhu *et. al*[18]. Yue *et al.* produced mesoporous WO_3 and a-Fe_2O_3 by using a similar pathway in 2005[31]. In 2007, Rumplecker *et. al.* synthesized several mesoporous Co_3O_4 with wall thickness changing from 4 to 10 nm and pore size from 3 to 10 nm by using cubic Ia3d symmetry KIT-6 templates having different wall thicknesses and pore sizes [32]. Later in 2010,

Ren *et al.* prepared a series of ordered mesoporous β-MnO_2 with varying pore size from 3nm to 11nm and wall thickness changing from 4.7 to 10.1 nm by using a similar procedure[33]. Since then; this method has been developed to synthesize highly crystalline ordered mesoporous metal oxides with systematically controlled wall thickness and pore size[33-35].

Hard templating method has advantages like choosing hard templates with respect to acquired structure of the target material, obtaining highly crystalline walls and eligibility for post synthesis solid-solid conversion to prepare low-valence metal oxides and lithiated mesoporous transition metal oxides[11], [36-38].

However; this method also has remarkable drawbacks. First, target materials must be stable in NaOH and HF solutions to remove the silica template. Secondly, stability of the transition metal ion precursors in the solution is curtail. Also, materials like lithiated mesoporous metal oxides, ZnO or Al_2O_3 cannot be synthesized due to the side reaction of precursors with the mesoporous template. Furthermore; filling the pores with filtrated metal ion precursor is difficult due to complex interactions between silica and precursor, and poor wetting of the pore walls of carbon template by the aqueous precursor solution are noticeable problems[20].

1.3 Preparation of Ordered Mesoporous Metal Oxides Using Soft Templates

Soft templating is a useful method to synthesize mesoporous metal oxides using amphiphilic molecules as templates. These molecules are known as surfactants and have both hydrophilic and hydrophobic domains on their

structure. When these surfactants are placed in polar solvents, they can self-assemble into supramolecular aggregates as the hydrophilic domains in contact with surrounding solvent and hydrophobic tails through the micelle center. For certain surfactant concentration, temperature and pressure values, these micelles may organize further and form lyotropic liquid crystalline (LLC) phase. This phase has long ranged orientational order of the micelles like crystal structure of solids and mobility like liquids. It has been investigated that certain inorganic precursors may collaborate with the surfactants by filling up the hydrophilic domains of the micelles to form a mesostructure. In other words; inorganic precursor acts as “cast” surrounded by “mold” of the liquid crystalline template. After hydrolysis, condensation and removal of the surfactants, a mesoporous negative replica of the LLC template is obtained[24, 40]. Figure 2 shows the synthetic route of the soft templating method for the preparation of mesoporous materials[25].

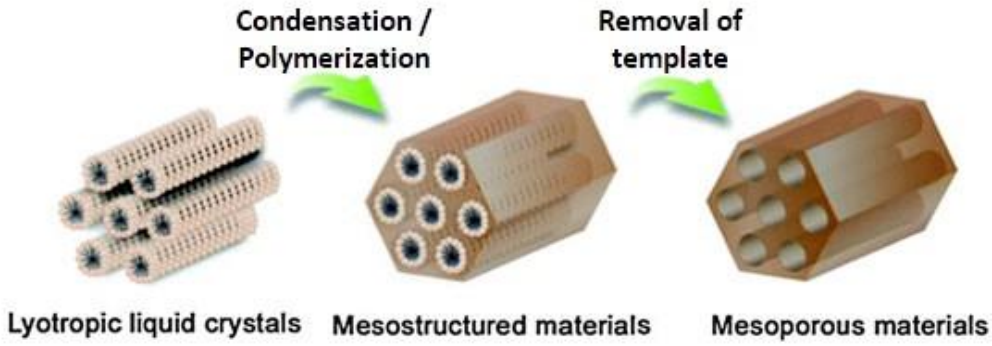

Figure 2: Synthetic procedure for the soft-template process for the preparation of porous mesostructures (Copyright © 2008 Wiley. Reprinted with permission from ref[25]).

Addition of inorganic precursor into a surfactant containing solution causes significant changes to the liquid crystal formation due to new interactions among

the surfactant, solvent and precursor species. These complex interactions make the process hard to control during hydrolysis, condensation and calcination steps[40].

Firstly; the ordered mesoporous silicas were discovered in 1992 by using soft templating method[1, 14]. In 1994, Huo *et al.* reported synthesis of ordered mesoporous metal oxides (WO_3, Sb_2O_5, Fe_2O_3, etc.) by using soft templating. However; during the removal of surfactants by calcination, mesoporous structure could not be preserved and collapsed[41]. Later on, it has been realized that the precursor should not condense too rapidly before the LC phase is formed, since untemplated precursor causes the formation of disordered mesostructures or bulk materials[40].

Later, so called "ligand assisted method" has been explored by Antonelli *et. al.* to prepare ordered mesostructure of TiO_2, wherein ligands attached to the metals decrease the rate of hydrolysis and the reaction proceed safely preserving the mesostructure during the removal of the template by calcination[42]. In 1996, the same group adopted the method for the synthesis of ordered mesostructure of Nb_2O_5[43]. Some other groups also used ligand assisted method for the synthesis of ordered mesoporous VO_x, Ta_2O_5 and phosphated ZrO_2 with amorphous walls[43-46].

Another important pathway for the formation of ordered semicrystalline mesoporous metal oxides was demonstrated by Yang *et. al* in 1998 [14, 48]. Amphiphilic poly(alkylene oxide) block copolymers were used as templates and inorganic salts as precursors to establish the network-forming metal-oxide species and obtained mesoporous oxides of TiO_2, ZrO_2, Al_2O_3, Nb_2O_5, Ta_2O_5, WO_3,

HfO_2, SnO_2, and mixed oxides of $SiAlO_{3.5}$, $SiTiO_4$, $ZrTiO_4$, Al_2TiO_5 and ZrW_2O_8 containing nanocrystalline domains within amorphous walls[48]. Brinker *et. al.* named this process as "evaporation-induced self-assembly" or EISA [49].

In a typical EISA synthesis, a homogeneous solution consisting of surfactant, soluble metal alkoxide or metal salt, a volatile solvent (like ethanol) and often acid (usually HCl) are mixed thoroughly. Nanoparticles smaller than 5nm could also be used as precursors to contribute the self-assembly[40]. The solution is spread over a large area by spray, spin, or dip coating and is given time for the evaporation of volatile components. During evaporation; concentration of the surfactant increases and in due course, the critical micelle concentration (cmc) is reached where the liquid crystalline phase nucleates. After further evaporation, water concentration of the phase reaches equilibrium with the relative humidity (RH) of the surrounding atmosphere in which can change the structure of the non-rigid mesophase. This stage is called as tunable steady state. With further condensation, solidified inorganic network of precursor is formed and template is removed by thermal or chemical treatments[50].

Majority of the previous studies conducted using classical templates in soft templating method ended up with moderate crystallinity or disordered and damaged mesostructures. Then, Sanchez and coworkers optimized the process by performing in- situ experiments in order to understand the structural changes using simultaneous small and wide angle X-ray scattering (SAXS/WAXS). Novel amphiphilic block copolymers (KLE polymers) were also preferred which are more robust, hydrophobic and applicable with a broader range of solvent systems. By using this method, they obtained mesoporous transition metal oxides (*e.g.,* MO_2, where M= Ti, Zr, Ce), mixed oxides (*e.g.,* SiO_2-TiO_2, TiO_2-ZrO_2,

ZrO_2-CeO_2) and complex metal oxide nano-crystalline films (*e.g.,* $SrTiO_3$, $MgTa_2O_3$) with high control of multiscale porosity and much higher thermal stability[19, 51].

Soft templating method has advantages like using low cost, non-toxic organic molecules and is easy to apply. Shape, size and morphology of the target material can be tuned by changing the composition of the solution[20]. However, there are also many disadvantages that should be taken into account; like complicated sol-gel process during the synthesis and high sensitivity to the environment conditions (*e.g.,* relative humidity). Slow hydrolysis and polymerization; especially of the transition metal ions are not easy steps to control the formation of oxides. If condensation proceeds too fast before the LC phase is formed, disordered worm-like mesopores or untemplated bulk materials may form[40]. The resulting mesostructures generally have amorphous or semi-crystalline walls and poor thermal stability. High temperature treatment may cause crystallites to grow uncontrollably, destroy the pores by collapsing the mesostructure. Although; using surfactants like amphiphilic block KLE copolymers may give high crystallinity and high thermal stability, the products have large pores and thick pore walls. The main weakness of soft templating is the metal salt to surfactant ratio is too low which prevents obtaining a stable mesostructure and makes the method not an efficient one to form a mesostructure[19, 52, 53].

1.4 Salt- Surfactant LLC Mesophase

The Lyotropic Liquid Crystalline (LLC) mesophases of oligo- (ethylene oxide) nonionic surfactants ($C_nH_{2n+1}(CH_2CH_2O)_mOH$, shortly symbolized as C_nEO_m) with H_2O have been investigated and improved by materials community

since the second half of the 20th century [1]. The LLC systems of H_2O, C_nEO_m and CTAB, ($C_{16}H_{33}N(CH_3)_3Br$) or SDS ($C_{12}H_{25}OSO_3Na$) have been attempted and their micellar solutions and the LC phase diagrams have been established[54, 55]. The effects of particular salt ions to the LLC properties of H_2O and C_nEO_m have also been studied and realized that these WSS (water-salt-surfactant) systems lose their stable structures after certain salt amounts[56–59]. The limiting salt quantity changes according to the counter anions of the specific salts. Also; the evaporation of water causes collapse of the system before mesophase is formed[60].

A new LLC mesophase of C_nEO_m and particular transition metal aqua complex salts ($[M(H_2O)_6]X_2$ (M= Co^{2+}, Ni^{2+}, Zn^{2+},etc.) and $[M'(H_2O)_4]^{2+}$ (M′= Cd^{2+} and Mn^{2+}; X= Cl^-, NO_3^-, and ClO_4^-) has been explored by Dag *et. al.* which has a very high $MX_2/C_{12}EO_{10}$ mole ratio[61–63]. Some of these salts practically form LC phases, which are compatible with the Hofmeister's series (the ordered list of the ions according to their solubilities). The Hofmeister series is;

$$SO_4^{2-} > HPO_4^{2-} > CrO_4^{2-} > CO_3^{2-} > Cl^- > Br^- > NO_3^- > I^- > ClO_4^- > SCN^-$$

On the left hand side of the series, there are lyotropic anions which make the surfactant molecules more hydrophobic and on the right hand side there are hydrotropic anions which make the surfactant molecules more hydrophilic and more soluble[63].

According to the list; ClO_4^- ions are expected to be more soluble than NO_3^- ions in an H_2O–surfactant system. However, transition- metal perchlorate salts are found to be harder to dissolve compared to the transition metal-nitrate salts (TMS) in a [TMS]- surfactant system because of the efficiency of the coordination of the

NO_3^- ions to metal ions, which decreases the ionic strength of the medium. Therefore; decrease in the ionic strength prevents the crystallization of the salt[62].

Later; Dag *et. al.* reported that NO_3^- salts of $[Ni(H_2O)_6]^{2+}$, $[Co(H_2O)_6]^{2+}$, $[Zn(H_2O)_6]^{2+}$ and $[Cd(H_2O)_4]^{2+}$ form lyotropic liquid crystal (LLC) phase with C_nEO_m surfactant easily. However; the Cl^- and SO_4^{2-} salts of these transition metals do not form LC phase since they are not soluble in C_nEO_m surfactant with an exception of $[Co(H_2O)_6]Cl_2$ [56–58]. The LC mesophases could have hexagonal 2D, hexagonal 3D or cubic structures depending on the type and the amount of the complex salt. The coordinated H_2O molecules in transition metal aqua complexes induce C_nEO_m to form the LC mesophase by hydrogen bonding. Furthermore, the ion-dipole and ion-ion interactions have an effective role on the self-assembling of LC mesophases [63–66].

In 2010; the presence of new types of LLC mesophases which are based on mixture of two surfactants of $C_{12}EO_{10}$-CTAB and $C_{12}EO_{10}$-SDS have been investigated by Dag *et. al.* [68]. $[Zn(H_2O)_6](NO_3)_2$ has been used as salt maintaining minimum H_2O concentration to increase the stability of the systems. In the resulting new phase; the TMS/ $C_{12}EO_{10}$ mole ratio increased up to 8.0, which has been the highest metal ion density in a lyotropic liquid crystalline (LLC) system[68]. Since CTAB is a cationic surfactant, the interaction between the alkyl tails of surfactants (CTAB and $C_{12}EO_{10}$) increases the hydrophobicity of the core and the interaction of the charged head groups enhances the hydrophilicity of the EO shell. There occurs a $NS^{+}(A^{-})_xM^{+}$ interaction where NS^+ is the micelle of $C_{12}EO_{10}$-CTA^+ complex cation, A^- is the counter anion (it is NO_3^- for this system), and M^+ is $[Zn(H_2O)_6]^{2+}$ or $[Zn(H_2O)_x(O_2NO)]^+$ ions. In the case

of SDS (sodium dodecyl sulfate), there occurs a $NS^-M^+A^-$ interaction, where the NS^- is a micelle of $C_{12}EO_{10}$ - DS^- complex anion. Both of these charged surfactants stimulate the system to dissolve more TMS at the hydrophobic-hydrophilic interface of the lyotropic liquid crystalline mesophase[69]. Figure 3 shows the representation of the LLC phase before and after addition of CTAB and $[Zn(H_2O)_6](NO_3)_2$.

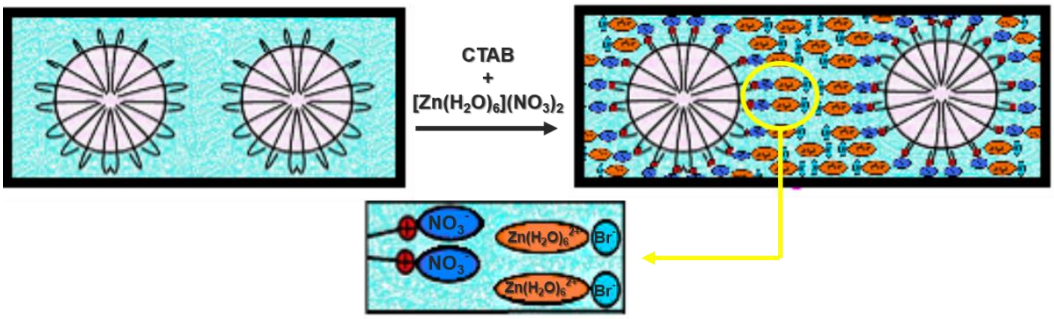

Figure 3: Representation of self-assembly of $C_{12}EO_{10}$ - CTAB - $[Zn(H_2O)_6](NO_3)_2$ species in LLC phase.

These studies illustrate that in order to increase the TMS concentration, the amount of the charged surfactant and water must also be increased and that there is a linear correlation between the mole ratio of TMS/$C_{12}EO_{10}$ and the mole ratio of CTAB/$C_{12}EO_{10}$ for higher water contents[63, 64]. It is also important that for two surfactant systems, free water is necessary to avoid the crystallization of TMS ions; however, water concentration must be minimized since presence of extra water decreases the stability of the system. Therefore, in order to stabilize the system back, excess water could be evaporated or addition of more surfactants is required[63, 64].

1.5 Preparation of Ordered Mesostructures Using Molten Salt Assisted Self Assembly (MASA) Method

In 2011, Dag *et.al.* developed a new pathway of soft templating to synthesize mesoporous materials with higher surface area and thinner pore walls by using small non-ionic surfactants, named as molten salt assisted self-assembly (MASA) approach[70, 71]. First, mesoporous ZnO (or CdO) coated silica thin films were prepared with different salt/silica ratios[70]. These thin films were then used as metal ion precursors to react with H_2S or H_2Se producing mesoporous silica metal sulfide or silica metal selenide thin films wherein the pore walls are made up of silica covered by metal sulfide or metal selenide nanoflakes. Then, the silica was removed by chemical etching with dilute HF solution to obtain metal chalcogenide nanoflake thin films[71]. Later, the polymerizing agent was changed from silica to titania source to produce mesoporous metal chalcogenide-titania thin films by using the same pathway[72].

In the MASA method, salt and non-ionic surfactant (10-lauryl ether or pluronics) can form lyotropic liquid crystalline self-assembly after evaporation of the volatile solvent (ethanol or water). Since the salt is confined in the hydrophilic domains of the mesophase, its melting point decreases below room temperature and solubility increases due to soft confinement effect and the molten salt acts as a second solvent in the self-assembly. Salts (alkaline metal, alkaline earth metal, transition metal or lanthanide salts) that have low melting point and high hygroscopicity are more suitable for the formation of mesophase [55].

The first step of the MASA process involves the preparation of a clear solution that contains salt, 10- lauryl ether ($C_{12}EO_{10}$, as non-ionic surfactant),

CTAB (cetyl trimethyl ammonium bromide as ionic surfactant), polymerizing agent (*e.g.*, titanium(IV)butoxide or tetra methyl ortho silicate), acid and ethanol (or H_2O) as a volatile solvent. The resulting solution has a low viscosity and hence could be spin or spray coated over a glass substrate to evaporate the volatile solvent forming a mesophase. After calcination, optically transparent mesoporous thin films or monolithic powders are obtained[72]. Figure 4 depicts the formation mechanism of metal oxide coated silica (or titania) mesostructures via MASA approach.

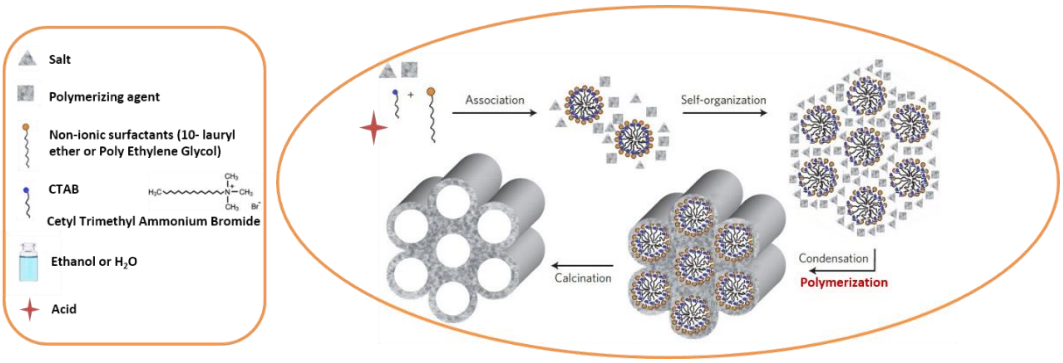

Figure 4: The formation mechanism of the mesoporous metal oxide coated silica (or titania) thin films by MASA method. (Copyright © 2012 Nature. Modified with permission from ref [73]).

The MASA approach has many advantages over the previously mentioned synthesis methods. First of all; in this method molten salt is used as a second solvent to form a LLC phase with the surfactants. Also; addition of an ionic surfactant (CTAB) to the media, stabilizes the interface of charged hydrophilic-hydrophobic domains and increases the salt uptake of the mesophase. Moreover; polymerizing agent forms a stable 3-D framework and prevents suffering from high temperature treatments, compared to the other soft templating methods. Finally; precursors like metal salts, titania, and silica are very common,

additionally synthesis of certain mesoporous ternary oxides is possible without any side reaction. Therefore, the MASA is a promising method, with potential applicability in preparing many other mesoporous materials that have not been synthesized yet [55].

1.6 Lithiated Transition Metal Oxides

Certain lithiated transition metal oxides are used as high performance materials in energy storage devices like Li ion batteries, rechargeable metal- air batteries, redox supercapacitors and catalysts for water splitting reactions [74-77] These materials are useful as cathodes for lithium batteries due to their high cell voltage of 4V and high charge capacity from a given amount of electrode material (120 mAh/g)[74]. They exhibit high electrocatalytic activity and stability in both OER (Oxygen evolution reaction) and ORR (Oxygen reduction reaction)[75]. In the case of supercapacitors, they have high energy density ascribed to their multiple valence state changes[76]. The valence fluctuation of transition metals and diffusivity of Li^+ ion make these materials also ideal for the water-splitting[77].

Recent studies show that, in all these fields of applications, with their higher specific surface area and ordered pore structures, mesoporous lithiated transition metal oxides show higher efficiency than that of nanoparticulate or bulk materials [77-84].

For the scope of this thesis, the synthesis methods and properties of $LiCoO_2$ and $LiMn_2O_4$ mesostructures from the literature are stated briefly in the next section.

1.7 Literature on $LiCoO_2$ and $LiMn_2O_4$

$LiCoO_2$ is the most widely used cathode material due to its high charge capacity and outstanding cycle life[84]. It is a semiconductor with a band-gap value of 1.7 eV [85]. $LiCoO_2$ has two forms, hexagonal and cubic structure. The cubic structure (referred as layered structure) is ideal for energy storage devices providing a 2D pathway for Li^+ diffusion in-out of the lattice during charge–discharge cycling. The theoretical capacity of layered $LiCoO_2$ is 272 mAh/g, but the reversible capacity is 140 mAh/g when the $LiCoO_2$ cathode is cycled between 3 and 4.2 V (measured with respect to Li metal)[86]. The layered HT (HT stands for high temperature) phase of $LiCoO_2$ is formed at high temperatures such as 900 ^oC and usually crystallizes in bulk form[74]. On the other hand, the hexagonal-spinel LT (LT stands for low temperature) phase which is more applicable as catalysts for water splitting reactions, is formed at low temperatures (like 350 ^oC) and can be tailored into nanostructures[75]. In other words; both phases have their own advantages and disadvantages in terms of applications.

In 2005, synthesis of mesoporous low temperature spinel $LiCoO_2$ and $LiCoO_2$ nanowire were first reported by Bruce *et.al.*[87]. It is difficult to use hard templating to synthesize mesoporous Li containing ternary oxides since Li source reacts with the template. Hence, post templating method was preferred. First mesoporous Co_3O_4 has been synthesized using mesoporous silica and after removal of the template, lithiation was carried out by reacting with LiOH at 400 ^oC for 1 hour. Surface area of the synthesized material was measured by low temperature isothermal adsorption/desorption of N_2 via the five point Brunauer-Emmett-Teller (BET) method and pore size distribution and the average pore size were determined by Barrett-Joyner-Halenda calculations from the desorption isotherms of the

samples. The resulting ordered mesoporous LT-$LiCoO_2$ (LT stands for low temperature) has crystalline walls with a thickness of 8 nm, a narrow pore size distribution around 3.7 nm and a BET surface area of 92 m^2/g. They also synthesized crystalline $LiCoO_2$ nanowires with a broad pore size distribution [68]. There is no other method that has been proposed for the synthesis of mesoporous $LiCoO_2$ in the literature yet.

Secondly; the cubic spinel $LiMn_2O_4$ (lithium manganese oxide, LMO) was reported to be a promising material due to its low cost, high energy density, high thermal stability, and nontoxicity[88]. $LiMn_2O_4$ exhibits only cubic-spinel structure. Tetrahedral and monoclinic-spinel phases have also been reported, but being highly unstable, these structures transform into cubic-spinel phase in time[88]. The band gap of this semiconductor is 1.3 eV[89]. The theoretical capacity of spinel $LiMn_2O_4$ is 120 mAh/g[90].

The first synthesis of well-ordered mesoporous spinel $LiMn_2O_4$ was reported by Luo *et.al.* in 2007[91]. After obtaining the mesoporous MnO_2 via hard templating, lithiated mesoporous MnO_2 was annealed at 350 ^oC for 2 hours to obtain the final product. The BET surface area of the mesostructure was found to be 55 m^2/g, wall thickness and pore size were 4.9 nm and 18 nm, respectively[91]. several studies were reported, using the same pathway to synthesize different mesostructures by changing the template, optimizing the temperature and calcination time[33, 92]. In 2013; Hwang and coworkers obtained mesoporous LMO by using soft templating[93]. P123 was used as a surfactant, $LiNO_3$ and $Mn(NO_3)_2$ as metal sources obtaining a product with 3.8 nm pore size, 31 nm wall thickness and 13.8 m^2/g BET surface area[93]. Chen *et. al.* used P123,

$Mn(CH_3COO)_2.4H_2O$ and $LiOH.H_2O$ as ingredients that resulted a material with a pore size of 5.5 nm and BET surface area of 42.5 m^2/g[74].

In this thesis, we adopted the MASA approach to synthesize first two metal oxides without a polymerizing agent in the media. The first step involves preparation of a clear solution of all the ingredients. Then, the solution is spin coated over a substrate producing the salt-surfactant LLC mesophase that resists to high temperature treatments to form first examples of mesoporous metal lithiates. Thesis is designed to give the insights of synthesis steps, like mesophase formation and structural changes during the heat treatments. Figure 5 depicts the proposed formation mechanism of the mesoporous $LiCoO_2$ / $LiMn_2O_4$ by using MASA method.

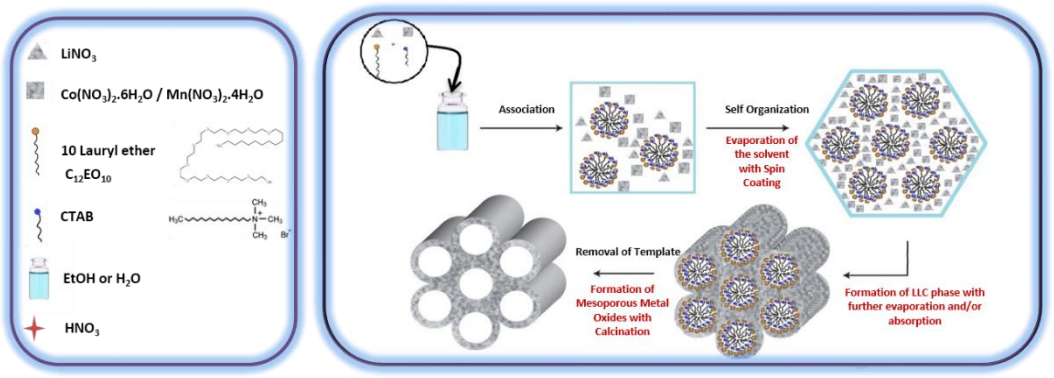

Figure 5: The formation mechanism of the mesoporous $LiCoO_2$ / $LiMn_2O_4$ by using MASA method. (Copyright © 2012 Nature. Modified with permission from ref [73]).

Chapter 2

Experimental

2.1 Sample Preparation

The process is initiated with preparation of clear solutions that contain two hydrated salts, $LiNO_3.xH_2O$ and $[Co(H_2O)_6](NO_3)_2$ (or $[Mn(H_2O)_4](NO_3)_2$), CTAB ($C_{16}H_{33}N(CH_3)_3Br$, ionic surfactant), 10-lauryl ether ($C_{12}EO_{10}$, non-ionic surfactant), HNO_3 and ethanol (or H_2O) as a volatile solvent. Solution is homogenized for 12 hours by stirring over a magnetic stirrer and spin coated over a glass substrate to form lyotropic liquid crystalline (LLC) films. The LLC films are calcined at temperatures ranging from 300 ^oC to 700 ^oC in air. Figure 6 briefly illustrates preparation of the samples.

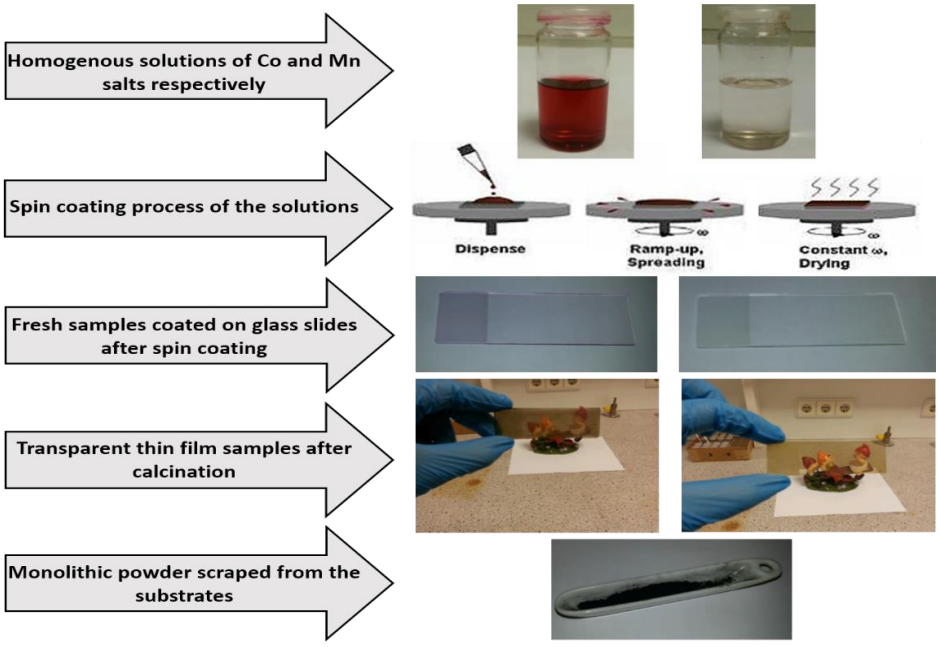

Figure 6: Schematic illustration of sample preparation via MASA method.

2.2 General Optimizations

2.2.1 Determination of salt uptake of LLC fresh films

The amount of salts has been optimized for the $LiCoO_2$ as prepared samples. The general pathway in Figure 6 has been followed for the preparation of the samples. Seven homogenized solutions containing 0.8 mmol $C_{12}EO_{10}$, 0.8 mmol CTAB, 6 g of ethanol with different amounts of salts have been prepared. The salt amounts were 4.5, 6, 9, 12, 15, 16 and 17 (Li + Co):$C_{12}EO_{10}$ mole ratios. The samples were prepared by spin coating above solutions over glass substrates at 1500 rpm for 7 seconds. The POM (polarized optical microscope) images of the fresh samples have been recorded. The small angle x-ray diffraction (XRD) patterns of the fresh samples have been collected. Then high angle XRD patterns of the 60 minutes aged samples were collected.

2.2.2 Determination of solvents (H_2O vs Ethanol)

The effect of the solvent used in solution has been tested. The general process in Figure 6 has been used for the preparation of the samples. 2 homogenized solution containing 2.4 mmol $LiNO_3.xH_2O$, 2.4 mmol $[Co(H_2O)_6](NO_3)_2$, 0.8 mmol $C_{12}EO_{10}$, 0.8 mmol CTAB but different solvents (S1: 6g of ethanol, S2: 6g H_2O) have been prepared. 2 sets (each set consists of 60-80 slides) have been prepared by spin coating on glass substrates at 1500 rpm for 7 seconds. Then these samples were calcined at 300 ^oC for 3 hours in an oven. Powders were obtained by scraping the slides carefully. High angle X-ray diffraction (XRD) patterns of the samples have been measured from 10^o to 80^o with 0.5 ^{o}/min scan rate. Raman spectra of the samples with 100 scans have been measured.

2.2.3 Determination of spin rate (LLC film thickness)

The effect of film thickness on the structure of products has been measured for $LiCoO_2$ samples. The general process in Figure 6 has been used for the preparation of the samples. A homogenized solution containing 1.8 mmol $LiNO_3.xH_2O$, 1.8 mmol $[Co(H_2O)_6](NO_3)_2$, 0.8 mmol $C_{12}EO_{10}$, 0.8 mmol CTAB and 6g of ethanol has been prepared. Three sets (each set consists of 60-80 slides) have been obtained by spin coating on glass substrates at 1000 rpm, 1500 rpm and 2000 rpm, respectively. Then these samples were calcined at 300 ^oC for 3 hours in air. Powders were obtained by scraping the slides carefully. High angle x-ray diffraction (XRD) patterns of the samples have been measured from 10^o to 80^o with 0.5 ^{o}/min scan rate.

2.2.4 Determination of the method (drop casting vs spin coating)

The method of coating on the formation of products has been tested for the $LiCoO_2$ samples. A homogenized solution containing 3.6 mmol $LiNO_3.xH_2O$, 3.6 mmol $[Co(H_2O)_6](NO_3)_2$, 0.8 mmol $C_{12}EO_{10}$, 0.8 mmol CTAB and 6g of ethanol has been used for 2 different sets (each set consists of 60-80 slides). Set I was obtained by spin coating on glass substrates at1500 rpm for 7 seconds. Set II was obtained by using drop casting method. For each substrate; 5 drops of the solution have been used for coating. Samples waited for 1 hour for the formation of ordered LLC phase. Then both sets were calcined at 450 ^oC for 1 hour. Powders were obtained by carefully scraping the slides. High angle XRD patterns and N_2 sorption isotherms of the samples have been collected.

2.2.5 Determination of the amount of Concentrated Nitric Acid

The effect of amount of concentrated nitric acid on the structure of products has been tested for the $LiCoO_2$ samples. The general process in Figure 6 has been used for the preparation of the samples. Fife homogenized solutions containing 2.4 mmol $LiNO_3.xH_2O$, 2.4 mmol $[Co(H_2O)_6](NO_3)_2$, 0.8 mmol $C_{12}EO_{10}$, 0.8 mmol CTAB, 6g of ethanol but different amounts of concentrated HNO_3: 500 mg, 375 mg, 250 mg, 125 mg, 0 mg have been prepared. Another solution containing 500 mg concentrated HNO_3 without CTAB (other compositional ratios are same with others) have been prepared and used to prepare six sets (each set consists of 60-80 slides) of samples by spin coating on glass substrates at 1500 rpm for 7 seconds. The small angle x-ray diffraction (XRD) patterns of the samples have been recorded after spin coating (1 sample in each set) over glass slides. Then these samples were calcined at 300 ^oC for 3 hours. Powders were obtained by scraping the slides carefully. High angle XRD patterns of the samples have been measured from 10^o to 80^o with $0.5\ ^o$/min scan rate.

2.2.6 Optimization of the calcination temperature

The effect of the temperature during calcination on the formation and structure of products has been tested for the $LiCoO_2$ samples. A homogenized solution containing 3.6 mmol $LiNO_3.xH_2O$, 3.6 mmol $[Co(H_2O)_6](NO_3)_2$, 0.8 mmol $C_{12}EO_{10}$, 0.8 mmol CTAB and 6g of ethanol has been used for fife different sets (each set consists of 60-80 slides). Sample sets prepared by spin coating on glass substrates at 1500 rpm for 7 seconds, were calcined at 400, 450, 500, 550, and 600 ^oC for 1 hour. The powder samples were obtained by carefully scraping

the slides. The high angle XRD patterns, N_2 sorption isotherms, and Raman spectra of the samples have been collected.

2.2.7 Optimization of the calcination time

The optimization of the calcination time on the structure of products has been done for the $LiCoO_2$ samples. A homogenized solution containing 1.8 mmol $LiNO_3.xH_2O$, 1.8 mmol $[Co(H_2O)_6](NO_3)_2$, 0.8 mmol $C_{12}EO_{10}$, 0.8 mmol CTAB and 6g of ethanol has been used for three different sets (each set consists of 60-80 slides). The sample sets were prepared by spin coating on glass substrates at 1500 rpm for 7 seconds, and then calcined at 300 ^oC for 1, 5, and 10 hours in air, respectively. The powder sample were obtained by carefully scraping the slides. The high angle XRD patterns and N_2 sorption isotherms of the samples have been measured.

2.2.8 Optimization of the pore size and surface area with respect to salt amounts

The amount of salts has been optimized for the $LiCoO_2$ samples. The general pathway in Figure 6 has been followed for the preparation of the samples. Fife homogenized solutions containing 0.8 mmol $C_{12}EO_{10}$, 0.8 mmol CTAB, 6g of ethanol with different amounts of salts have been prepared. The salt amounts were 4.5, 6, 9, 12, and 15 (Li + Co):$C_{12}EO_{10}$ mole ratios. Fife sets (each set consists of 60-80 slides) of samples were prepared by spin coating above solutions over glass substrates at1500 rpm for 7 seconds. Then these samples were calcined at 300 ^oC for 3 hours. The POM (polarized optical microscope) images of the calcined samples have been recorded. The small angle x-ray diffraction (XRD) patterns of

the calcined samples have been collected (1 sample in each set). The powder samples were collected by carefully scraping the slides. The high angle XRD patterns and N_2 sorption isotherms of the powders were collected.

2.3 $LiCoO_2$ preparation with/without CTAB

The effect of CTAB on the structure of products has been tested for the $LiCoO_2$ samples. The general pathway in Figure 6 has been followed for the preparation of the samples. 3 homogenized solutions containing 0.8 mmol $C_{12}EO_{10}$, 0.8 mmol CTAB, 6g of ethanol but different (Li + Co):$C_{12}EO_{10}$ mole ratios: 4.5, 6, and 9 have been prepared, respectively. Three more solutions having same compositional ratios as the previous group without CTAB have also been prepared. Six sets (each set consists of 60-80 slides) have been obtained by spin coating on glass substrates at 1500 rpm for 7 seconds. Then these samples were calcined at 450 ^oC for 1 hour. The powder samples were collected by carefully scraping the slides. The high angle XRD patterns and N_2 sorption isotherms of the powders have been collected.

2.4 $LiCoO_2$ preparation using $CoBr_2$ as cobalt source

The general pathway has been followed for sample preparation in Figure 6. Two solutions have been prepared with the mole ratios, given in Table 1 (amounts of components were set by using 0.8 mmol of $C_{12}EO_{10}$ as a reference) with 6g of ethanol.

	$CoBr_2$:$C_{12}EO_{10}$ mole ratio	$Co(NO_3)_2.H_2O$:$C_{12}EO_{10}$ mole ratio	CTAB:$C_{12}EO_{10}$ mole ratio	Co :$C_{12}EO_{10}$ mole ratio
S1	**0**	**4.5**	**1**	**4.5**
S2	**2**	**2.5**	**0**	**4.5**

Two sets (each set consists of 60-80 slides) of samples have been prepared by spin coating above solutions on glass substrates at 1500 rpm for 7 seconds. Then these samples were calcined at 450 ^oC for 3 hours. The powder samples were collected by carefully scraping the slides. The high angle XRD patterns of the samples have been collected. Then, the powder obtained from the solution containing $CoBr_2$ (S2) has been washed up by suction and dried out. The high angle XRD pattern of the dry sample has been measured.

2.5 Synthesis of CTAN ($C_{16}H_{33}N(CH_3)_3NO_3$)

The cationic surfactant cetyltrimethylammonium nitrate (CTAN) has been synthesized by following a literature method.[94] A $AgNO_3$ methanol–water (1:1 ratio) solution has been prepared in dark by using 9.157g $AgNO_3$, 100g methanol and 100g distilled water. A solution of cetyltrimethylammonium bromide (CTAB) has been prepared by dissolving 20 g of CTAB in 100 g of methanol. These two homogenized solutions have been mixed in the dark slowly and was stored in the dark (by covering the bottle with aluminum foil), for 10 days at low temperature (+4 ^oC in the fridge). The solution was filtered with a Millipore TM system with a pore diameter of 1 micron and AgBr was removed by filtration. Methanol and water were evaporated first by a rotating evaporator and then by using a vacuum oven. The resulting product was dissolved in methanol and was recrystallized two

times. The XRD patterns and FTIR spectra of the powders of CTAB and CTAN were measured.

2.6 $LiCoO_2$ preparation with CTAN vs CTAB

The general pathway in Figure 6 has been followed for the preparation of the samples. Three homogenized solutions containing 3.6 mmol $LiNO_3.xH_2O$, 3.6 mmol $[Co(H_2O)_6](NO_3)_2$, 0.8 mmol $C_{12}EO_{10}$ and 6 g of ethanol has but different ionic surfactants with same mole ratio (S1 containing 0.8 mmol CTAB, S2 containing 0.8 mmol CTAN, S3 containing no ionic surfactant) have been used for 3 different sets (each set consists of 60-80 slides). Sample sets were prepared by spin coating on glass substrates at 1500 rpm for 7 seconds, were calcined at 450 ^oC for 10 hours in air. The powder samples were obtained by carefully scraping the slides. The high angle XRD patterns and N_2 sorption isotherms of the powders have been collected.

2.7 Optimization of the calcination temperature of the $LiCoO_2$ prepared with CTAN

The calcination temperature has been optimized for the $LiCoO_2$ samples. A homogenized solution containing 3.6 mmol $LiNO_3.xH_2O$, 3.6 mmol $[Co(H_2O)_6](NO_3)_2$, 0.8 mmol $C_{12}EO_{10}$, 0.8 mmol CTAN and 6 g of ethanol has been used for 3 different sets (each set consists of 60-80 slides). Sample sets prepared by spin coating on glass substrates at 1500 rpm for 7 seconds, were calcined at 350, 400 and 450 ^oC for 10 hours in air, respectively. The powder samples were obtained by carefully scraping the slides. The high angle XRD patterns and N_2 sorption isotherms of the samples have been collected.

2.8 $LiMn_2O_4$ preparation with CTAN vs CTAB

The general pathway in Figure 6 has been followed for the preparation of the samples. Two homogenized solutions containing 1.6 mmol $LiNO_3.xH_2O$, 3.2 mmol $[Mn(H_2O)_4](NO_3)_2$, 0.8 mmol $C_{12}EO_{10}$ and 6 g of ethanol has but different ionic surfactants with same mole ratio (S1 containing 0.8 mmol CTAB, S2 containing 0.8 mmol CTAN) have been used for 2 different sets (each set consists of 60-80 slides). Sample sets, prepared by spin coating on glass substrates at1500 rpm for 7 seconds, were calcined at 350 ^oC for 10 hours. The powder samples were obtained by carefully scraping the slides. The high angle XRD patterns of the powders have been collected.

2.9 Determination of solvents (H_2O vs Ethanol) for $LiMn_2O_4$ synthesis

The effect of the solvent used in solution has been tested. The general process in Figure 6 has been used for the preparation of the samples. Two homogenized solution containing 2.0 mmol $LiNO_3.xH_2O$, 4.0 mmol $[Mn(H_2O)_4](NO_3)_2$, 0.8 mmol $C_{12}EO_{10}$, 0.8 mmol CTAB but different solvents (S1: 6 g of ethanol, S2: 8g H_2O) have been prepared. Two sets (each set consists of 60-80 slides) have been obtained by spin coating on glass substrates at 1500 rpm for 7 seconds. Then these samples were calcined at 350 ^oC for 1 hour. The powder samples were obtained by carefully scraping the slides. The high angle x-ray diffraction (XRD) patterns of the samples have been measured from 10^o to 80^o with 0.5 ^{o}/min scan rate. Raman spectra of the samples with 100 scans have been measured.

2.10 Optimization of the salt amounts for $LiMn_2O_4$ samples

The effect of change in the amount of salts on the structure of products has been measured for the $LiMn_2O_4$ samples. The general pathway in Figure 6 has been followed for the preparation of the samples. Five- homogenized solutions containing 0.8 mmol $C_{12}EO_{10}$, 0.8 mmol CTAB, 6 g of ethanol but different amounts of salts have been prepared. The salt amounts were optimized by using (Li + Co):$C_{12}EO_{10}$ mole ratios of 4.5, 6, 7.5, and 9. Four sets (each set consists of 60-80 slides) have been obtained by spin coating on glass substrates at 1500 rpm for 7 seconds. The POM images of the fresh samples have been recorded. The small angle XRD patterns of the fresh samples have been recorded (1 sample in each set). Then these samples were calcined at 350 ^oC for 1 hour. The powder samples were collected by carefully scraping the slides. The high angle XRD patterns of the samples were recorded from 10^o to 80^o with 0.5 ^{o}/min scan rate. Raman spectra of the samples with 100 scans have been measured. N_2 sorption isotherms of the powders have been collected.

2.11 Instrumentation

2.11.1 TEM Analysis

Homogenized solution of the required sample has been spin coated over a glass substrate at 6000 rpm for 10 seconds to obtain a LLC thin film. Fresh sample was calcined at certain temperature and time, scraped from the substrate and grinded in a mortar for 10 minutes to obtain smaller particles. The sample was then placed in a solution of ethanol and sonicated for 2 hours to disperse the particles. The dispersed mixture was dropped on a carbon coated Cu grid with 300

mesh under an UV lamp. The dried grid was placed into the high resolution transmission electron microscope (HRTEM) of JEOL JEM 2100 F operating at a voltage of 200 kV for imaging.

2.11.2 XRD Measurements

Thin film and powder x-ray diffraction (XRD) patterns were recorded by using a Rigaku Miniflex diffractometer, equipped with a Miniflex goniometer and an x-ray source with Cu $K\alpha$ radiation, at λ = 1.5405 Å, 30 kV and 15 mA. XRD pattern of the thin films were collected between 1 and 4^{o} with 0.5 ^{o}/min. For certain fresh samples, Cu block (sometimes 2 or 3 blocks) was inserted in front of the detector to decrease the intensity of the diffraction line in order to protect the detector. Each Cu block decrease the intensity of the line by a factor of ten. The powder sample was packed into a standard glass sample holder and the pattern was collected between 10 and 80^{o}, 2θ, values with a scan rate of 0.5 ^{o}/min. The diffraction patterns were indexed using the Joint Committee on Powder Diffraction Standards (JCPDS) cards.

2.11.3 N_2 (77.4 K) Sorption Measurements

Specific Surface Area (SSA) and pore size of the certain samples were measured by low temperature isothermal adsorption/desorption of N_2 via the five point Brunauer, Emmett, and Teller (BET) and the average pore size were determined by Barrett-Joyner-Halenda calculations from the desorption isotherms of the samples respectively. Before the measurement, the samples were dehydrated at 573 K for 2 h in vacuum. The samples were measured by using a TriStar 3000 automated gas adsorption analyzer (micrometrics) in a relative

pressure range, P/P_o, from 0.01 to 0.99 atm. The saturated pressure was measured over 120 minutes' intervals. The surface areas of the different samples measured were calculated in the range 0.05 to 0.3 atm relative pressure with 5 points.

2.11.4 Polarized Optical Microscopy (POM) Measurements

The POM images were recorded by using ZEISS Axio Scope.A1 polarizing optical microscope in transmittance mode.

2.11.5 FT-IR Measurements

The FT-IR spectra were recorded using a Bruker Tensor 27 model FT-IR spectrometer. A Digi Tect TM DLATGS detector was used with a resolution of 4.0 cm^{-1} from 400 cm^{-1} to 4000 cm^{-1} range. The data obtained after 256 scans were recorded.

2.11.6 Micro-Raman Measurements

LabRam confocal raman microscope with a 300 mm focal length has been used for the measurements. The device has a Ventus LP 532, 50 mW, diode pumped solid-state laser operator at 20 to 34 Mw with a polarization ratio of 100:1, a wavelength of 532.1 nm and a 1024x256 element CCD camera. The signal collected was transmitted via a fiber optic cable into the spectrometer with 600 g/mm grating. The Raman spectra of the samples were recorded by placing the probe tip on the desired point of the sample over the glass or silicon wafer.

Chapter 3

Results & Discussion

3.1 The general synthesis method for the mesoporous $LiCoO_2$ thin films.

Certain mixture of salts ($LiNO_3$ and $[Co(H_2O)_6](NO_3)_2$) and surfactants are homogenously dissolved in ethanol. The solution is stirred on a magnetic stirrer at least for 6 hours and spin coated on glass substrates to obtain a thin LLC mesophase on the substrates. Small angle XRD patterns and POM images of the fresh samples were recorded to identify the liquid crystalline mesophases. These fresh LLC films are then calcined at certain temperatures for 1-3-5 or 10 hours to obtain mesoporous $LiCoO_2$ monoliths and powders. The small angle XRD measurements and POM images of the calcined films were also collected to determine the order of the mesostructure. Powder of these samples were collected by scraping 60-80 calcined films over the glass substrates and used to collect the high angle XRD, Raman, TEM and BET data for the characterization of the samples.

During the synthesis, several parameters that control the features like purity, pore size, surface area and crystallinity of the $LiCoO_2$ mesostructure have been optimized by determining solvent type, thickness of the LLC film, acid amount, salt uptake, calcination temperature, calcination time and surfactant used for the synthesis.

In the next section; determination of salt uptake of the LLC fresh films of the solutions will be discussed briefly.

3.1.1 Determination of salt uptake of LLC fresh films

MASA approach states that melting point of the salt confined in the hydrophilic domains of the mesophase decreases even down to cryogenic temperatures and molten salt acts like a second solvent in the LLC media. The hydrophobic forces between alkyl tails and hydrogen bonding network in the hydrophilic domains of the surfactant molecules hold the micelle units of the mesophase together. Compositional ratio determines the geometric arrangement of the micelles as cubic, 2D hexagonal or 3D hexagonal and etc. Increasing salt amount, the micellar hydrophilic domains expand, and are pushed further apart. As a result, lattice parameters and d-spacing values of the mesophase increase, see Figure 7(a). There is a certain salt uptake of each transition metal LLC system at which above this ratio, the system cannot form ordered mesophase, since the weak attractive forces among the micelles cannot hold the mesostructure anymore. Order and uniformity of the structure is important for the formation of the mesoporous materials. Hence, the small angle XRD measurement and POM measurement were used to determine maximum salt uptake of the liquid crystalline phase and also the order of the mesostructure of $LiCoO_2$ fresh films. Figure 7 illustrates the small angle XRD patterns, POM images and calculated d-spacing values of the samples with increasing salt:surfactant mole ratios.

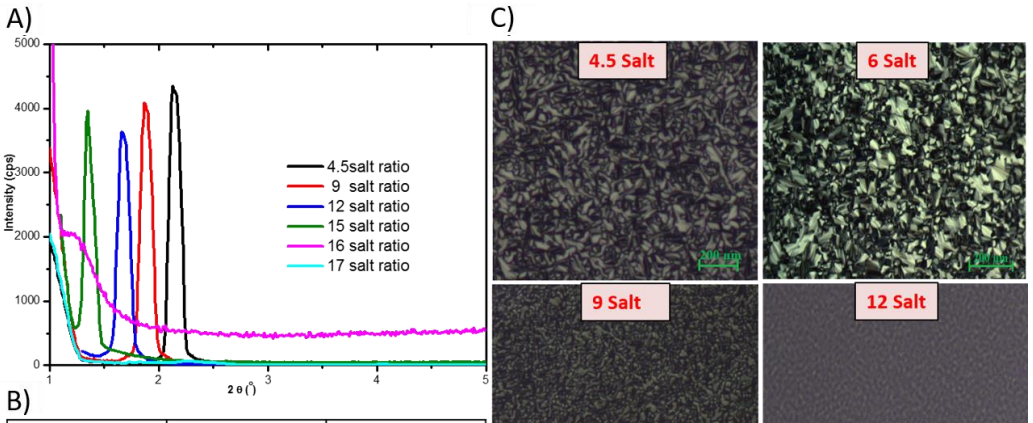

B)

Salt:$C_{12}EO_{10}$	Bragg Angle (°)	d- Spacing (Å)
4.5	2.15	41.2
9	1.88	46.9
12	1.67	52.7
15	1.35	65.3
16	1.21	73.0

Figure 7: A) Small angle XRD pattern of the fresh samples B) The Bragg angle and the d-spacing values of the samples C) POM images of the fresh samples prepared using different salt:$C_{12}EO_{10}$ mole ratios (as indicated in the patterns and images).

Up to 15 mole ratio, the diffraction lines of fresh samples are highly intense and sharp, indicating a long range order in the mesophase. Hence, Cu blocks have been inserted in between the source and detector in order to protect the detector of the diffractometer. Bragg's law has been used to calculate d-spacing values of each sample, tabulated in Figure 7(b). The XRD patterns and the calculated d-spacing values confirmed the increase in the lattice parameters of the fresh samples with ascending amount of salt in the media. The last sample containing 17 salt:surfactant ratio did not diffract since there is no ordered stable mesophase formed due to excess amount of salt loaded to the media. The POM images of the fresh samples shown in Figure 7(c) are also consistent with the XRD data. First 4

samples exhibit hexagonal geometry and the sample containing 17 salt:surfactant ratios did not show any pattern. That might be due to mixed geometry or cubic geometry of the mesophase.

In order to find out whether there was any salt leached out of the mesophase, the high angle XRD patterns of the samples have also been measured from the aged samples, see Figure 8.

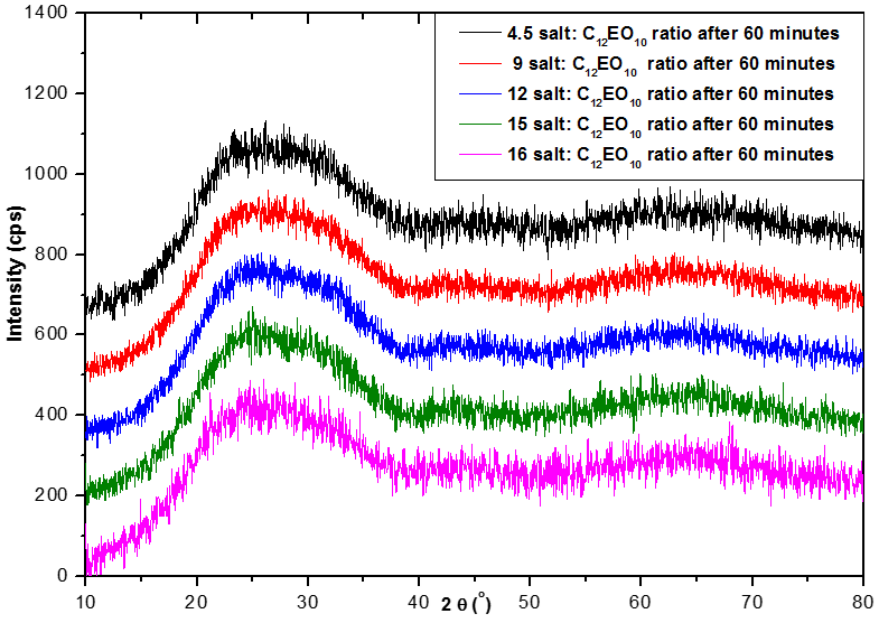

Figure 8: High angle XRD patterns of the as prepared samples containing different salt: surfactant ratios aged for 60 minutes.

The XRD patterns of the aged samples exhibited no diffraction lines and it is clearly shown that no salt or CTAB crystals were observed even after 60 minutes aging of the films. The mesophases, in all compositions, were stable long enough and ready for further heat treatments. It means that all the salt is in molten state in the media of each sample. However; since there was no diffraction of the 17 mole ratio in the small angle XRD pattern, likely the mesophase is not ordered. Hence;

the salt uptake of the LLC system has been determined as high as 16 salt:surfactant ratio to obtain an ordered mesostructure after calcination.

3.1.2 The effect of the solvent on the formation of the $LiCoO_2$ mesostructure.

To investigate the effect of the second solvent, two different solvents have been used. The clear solutions of the ingredients were prepared in both water and ethanol with and without CTAB as the charged surfactant. The thin films were obtained first by spin coating above clear solutions over a silicon wafer and glass slide and then calcined to collect the Raman spectra and XRD patterns, respectively. The Raman spectra of the samples from both water and ethanol are shown in Figure 9.

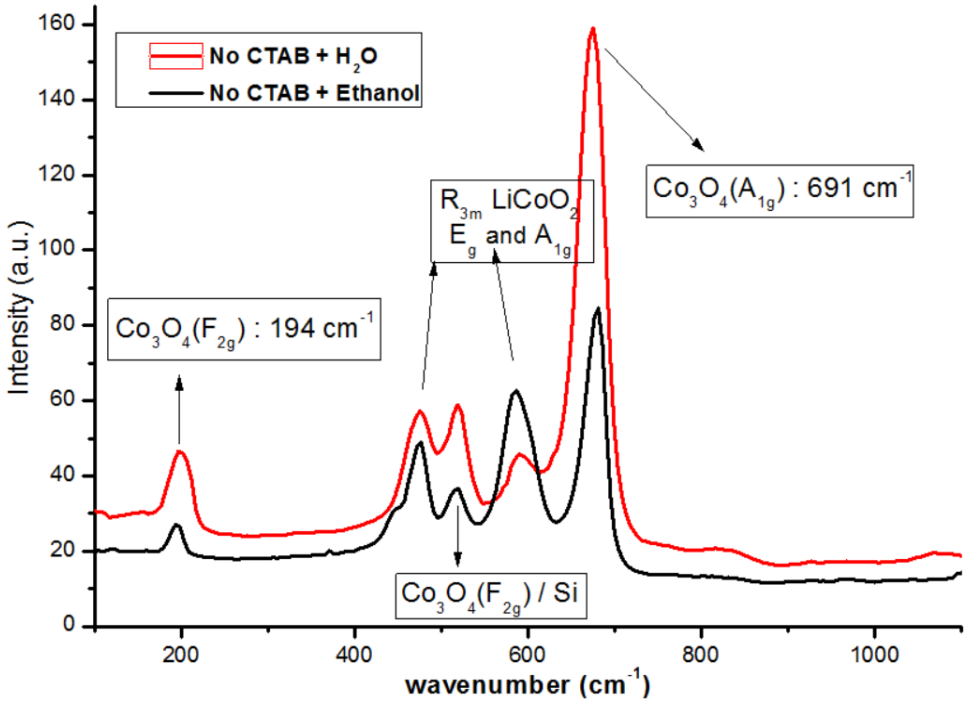

Figure 9: Raman spectra of the powders obtained by using H_2O and ethanol on Si wafer.

Briefly, the hexagonal $LiCoO_2$ with R-3m symmetry has two Raman active modes at 486 and 597 cm^{-1}, arising from the E_g and A_{1g} modes, respectively[95]. Spinel $LiCoO_2$ exhibits peaks at 483, 525, 621, and 690 cm^{-1} that are correspond to the $2T_g$, E_g, and A_{1g} modes, respectively[95]. Spinel Co_3O_4 has five Raman modes at 194, 488, 522, 618 and 691 cm^{-1}[96]. The Raman spectra of the powders obtained without CTAB is given in Figure 9. The sample prepared by H_2O has distinctive Co_3O_4 peaks arising at 194 and 691 cm^{-1} compared to the one prepared by ethanol and it has weak peaks of $LiCoO_2$ at 486 and 597 cm^{-1} compared to the one prepared with H_2O. The peak at 522 cm^{-1} is due to Si wafer and T_{2g} mode of Co_3O_4.

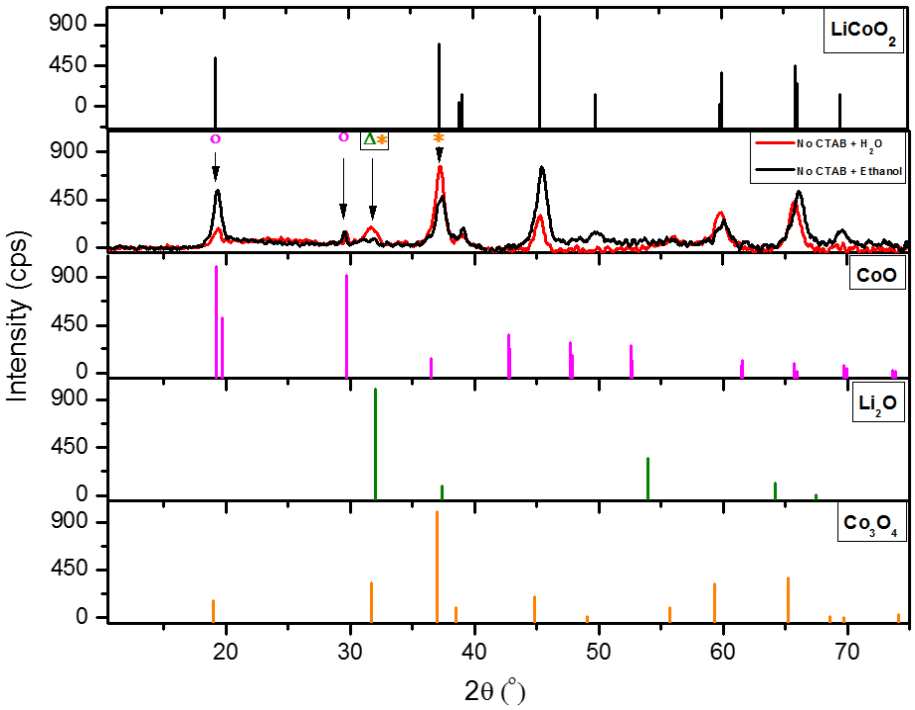

Figure 10: XRD pattern of the powders obtained by using H_2O and ethanol as solvents. Assignments of the diffraction patterns were performed (JCPDS 044-0145, 043-1003, 01-080-4682. 04-006-3706). o: line of CoO, Δ: line of Li_2O and *: lines of CO_3O_4 are the assignments of side products.

The XRD pattern of the same samples, in Figure 10, also confirms the Raman data. The most intense line of $LiCoO_2$ originates from the (104) plane and the most intense line of Co_3O_4 having Fd3m symmetry is due to (311) plane, according to the JCPDS 044-0145 and 043-1003 PDF cards, respectively. The sample obtained by using ethanol has more intense lines, which correspond to R-3m $LiCoO_2$ only. The lines arising from possible side products of Co_3O_4, Li_2O and CoO are more intense in the case of the sample obtained by using H_2O.

The samples containing CTAB prepared using water and ethanol as the solvents also gave the similar results, see Figures 11(A) and (B).

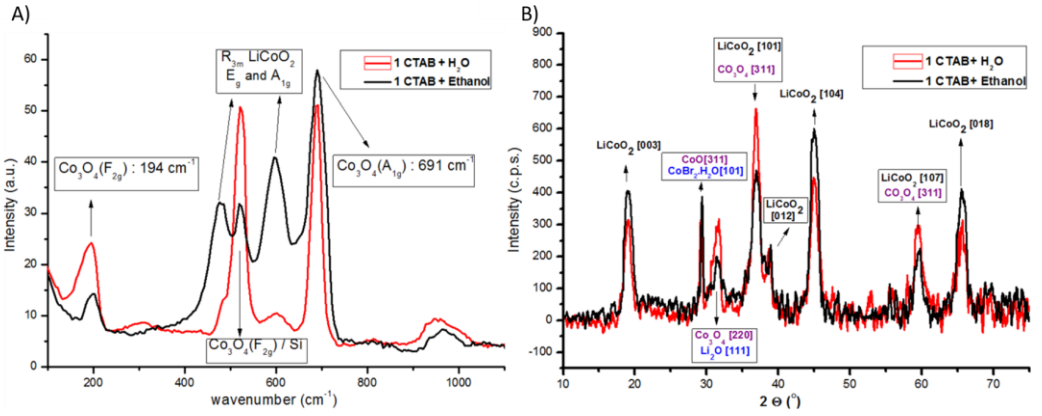

Figure 11: A) Raman spectra of the powders obtained by using H_2O and ethanol on Si wafer. B) XRD pattern of the powders obtained by using H_2O and ethanol as solvents. Assignments of the diffraction patterns were performed (JCPDS 044-0145, 043-1003, 01-080-4682, 04-006-3706, 023-0182).

On the Raman spectra; the broad peak appeared at around 941 cm^{-1} could be due to Si wafer or $CoBr_2$ side product, since there appears the most intense Raman peak at the same position in the bulk $CoBr_2$ [97]. Other peaks of the bulk $CoBr_2$ are relatively weak and appear at 87 cm^{-1}, 154 cm^{-1}, 242 cm^{-1} and 463 cm^{-1} [97]. Intensity of the line at 29.7° in the XRD pattern increased, compared to the

sample prepared without CTAB. The reason might be due to presence of Br^- ion coming from CTAB that may produce $CoBr_2.H_2O$ crystals as a side product during aging and calcination of the sample; it is the most intense line at 29.7 ^{o} of $CoBr_2.H_2O$ crystals, according to the JCPDS 023-0182 PDF card. As all the data obtained from XRD and Raman measurements were examined, since the samples prepared with ethanol have less side products than the ones prepared with H_2O for both of the sample sets with/without CTAB, it could be concluded that the ethanol is an efficient solvent to synthesize the mesoporous $LiCoO_2$.

3.1.3 Determination of spin rate (LLC film thickness)

We also investigated the role of spin coating rate that pre-determines the thickness of the films. The thickness is important for various reason and also for the synthesis. This step ensures if the film thickness is an important parameter for obtaining the same pore system in all thicknesses. Therefore, calcined films were obtained at three different spin rate, namely 1000, 1500, and 2000 rpm.

High angle XRD patterns of the powder samples containing no CTAB prepared by using 3 different spin rates and JCPDS cards of the possible side products are given in Figure 12.

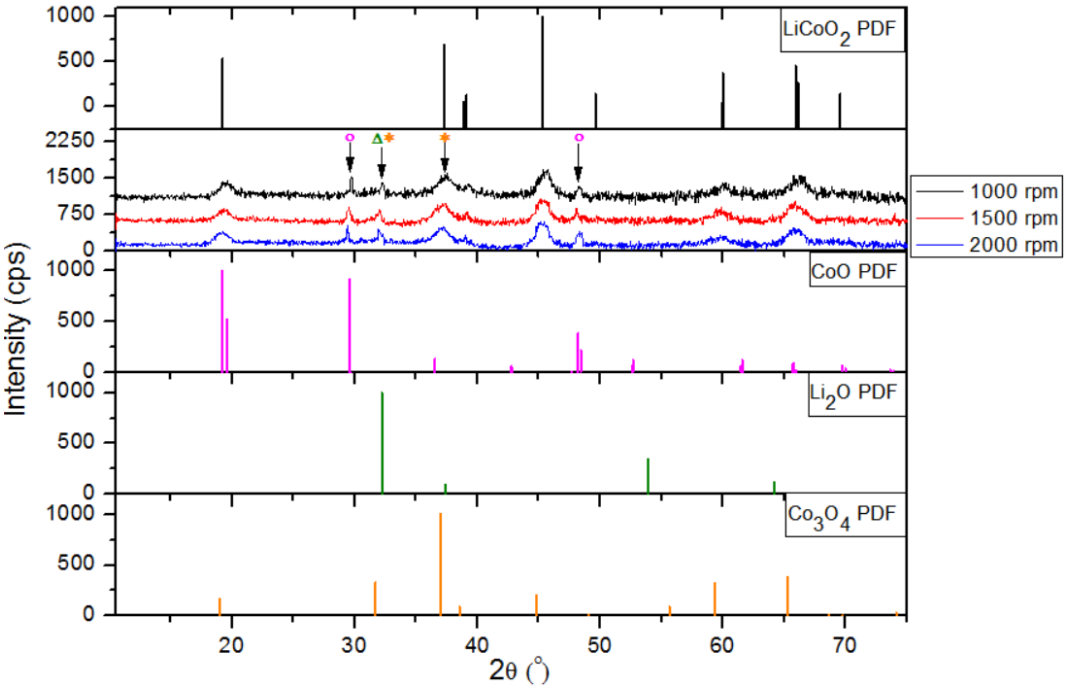

Figure 12: High angle XRD pattern of the samples obtained by different spin rates. o: lines of CoO, Δ: line of Li_2O and *: lines of CO_3O_4 are the assignments of side products.

There is no visible difference observed between the patterns by changing spin rate. The preparation of the powders from the thinner films did not prevent side product formation. These data show that there is no thickness dependent side product formation among the thicknesses investigated in this thesis work. This is important to show that mesophase before calcination must be the same in all thickness investigated. However, much thicker samples show differences, see next section.

3.1.4 Determination of the method (drop casting vs spin coating)

The effect of the method of coating on the formation of side products were investigated by comparing high angle XRD patterns of the samples coated by two methods (drop casting and spin coating), Figure 13.

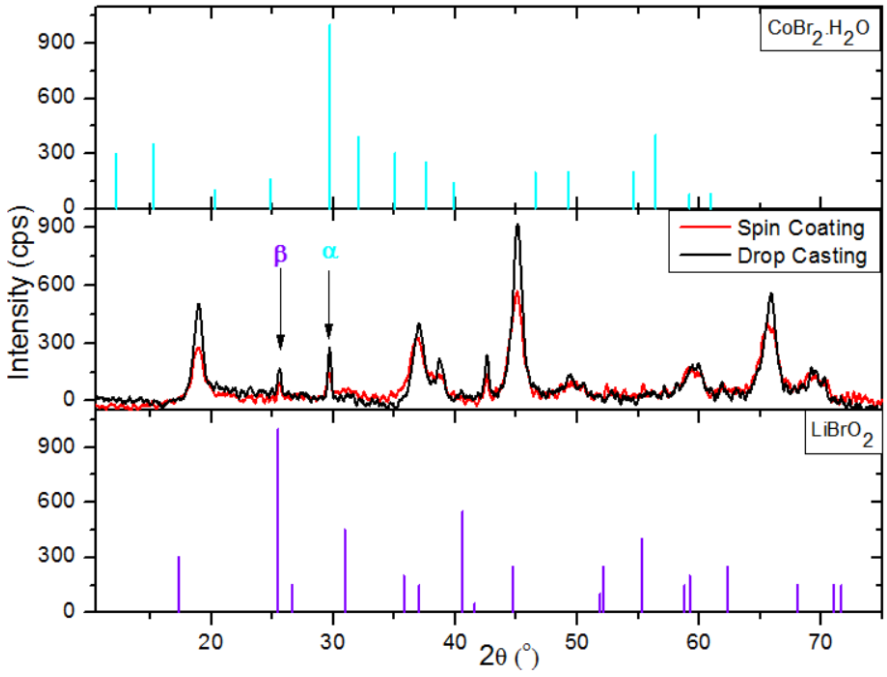

Figure 13: High angle XRD patterns of the samples obtained by drop casting and spin coating and JCPDS cards of the possible Br^- containing side products. α: line of $CoBr_2.H_2O$ and β: line of $LiBrO_2$ are the assignments of side products

The samples were prepared at 9 salt/surfactant mole ratio. The sample obtained by drop casting has relatively sharper and more intense lines for both target material and side products. N_2 sorption data are also consistent with the XRD data, Figure 14.

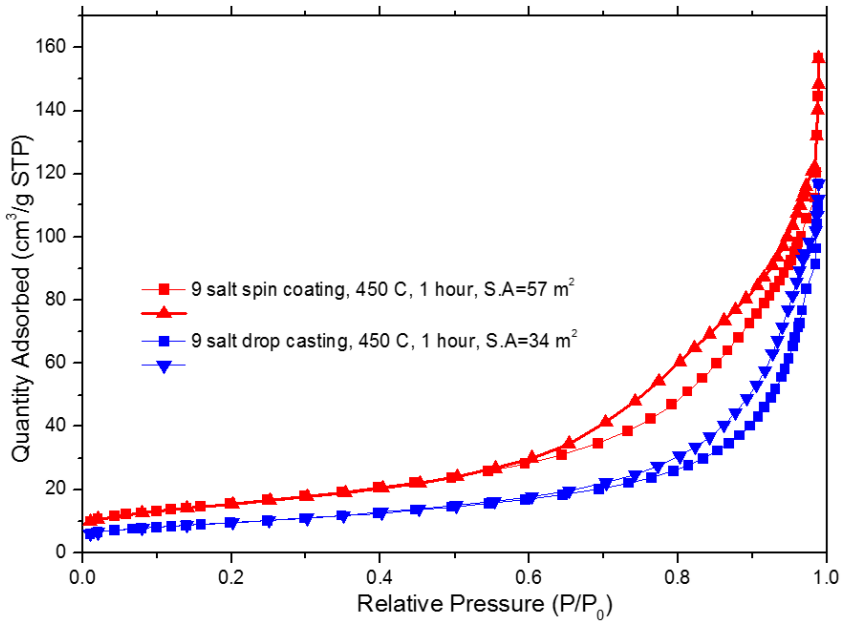

Figure 14: N_2 (77.4 K) sorption isotherms of the samples calcined at 450 ^oC for 1-hour.

It can be easily seen from the Figure 14 that the isotherms are type IV (characteristic for mesoporous materials) with hysteresis. The BET surface area decrease from 57 m^2/g to 34 m^2/g which can be attributed to the excessive crystallization with the change of method. Desorption BJH pore size also increased from 16 nm to 21 nm by changing the method to drop casting. The changes in the pore volume are coherent with the pore size, as 0.24 cm^3/g and 0.18 cm^3/g from spin coating to drop casting, respectively. This confirms the consistency of the XRD data with the N_2 sorption data and also proved that the mesoporous walls grow in size and further crystalize with increasing thickness of the film. It is important to note that the thicker films usually have more disordered region between the two interfaces, the interface between the substrate and the gel and gel and air. In between these two ordered regions, there is a more disordered region in the middle. With increasing thickness; the disordered region in the middle increases and during calcination the sample gets more non-uniform

structure with crystallization. Figure 15 shows the pore size distribution plots of the same samples. The pore size distribution is broader for the sample prepared by drop casting as expected. Since obtaining an ordered mesostructure is important for various reasons, drop casting method has been considered as not appropriate for the production of $LiCoO_2$ ordered mesostructures.

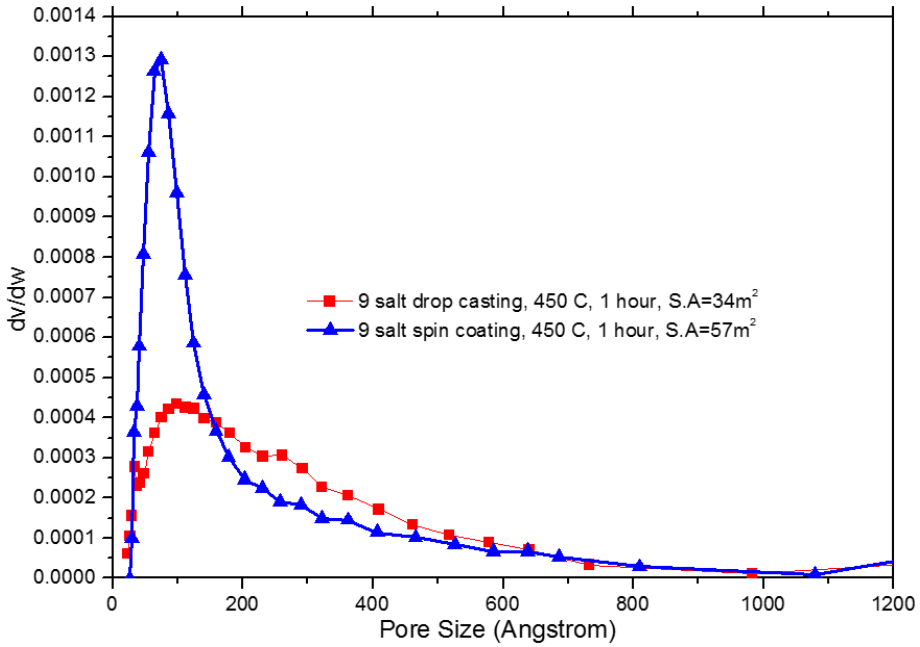

Figure 15: Pore size distribution plot of the samples prepared with different methods.

3.1.5 Determination of the amount of concentrated nitric acid

As of the last parameter, we also checked the role of acid in the synthesis media. In order to obtain pure $LiCoO_2$ mesostructure, all Co^{2+} ions in the solution must be oxidized to Co^{3+} and react with Li^+ ions. HNO_3 is a strong oxidizing agent and could oxidize Co^{+2} to Co^{+3} and decrease the formation of Co_xO_y species. 6 set of samples containing different amount of acid with and without CTAB have been synthesized and their high angle XRD patterns were obtained.

The samples were prepared at 6 salt/surfactant mole ratio. The effect of amount of concentrated nitric acid on the formation of products has been illustrated in Figure 16.

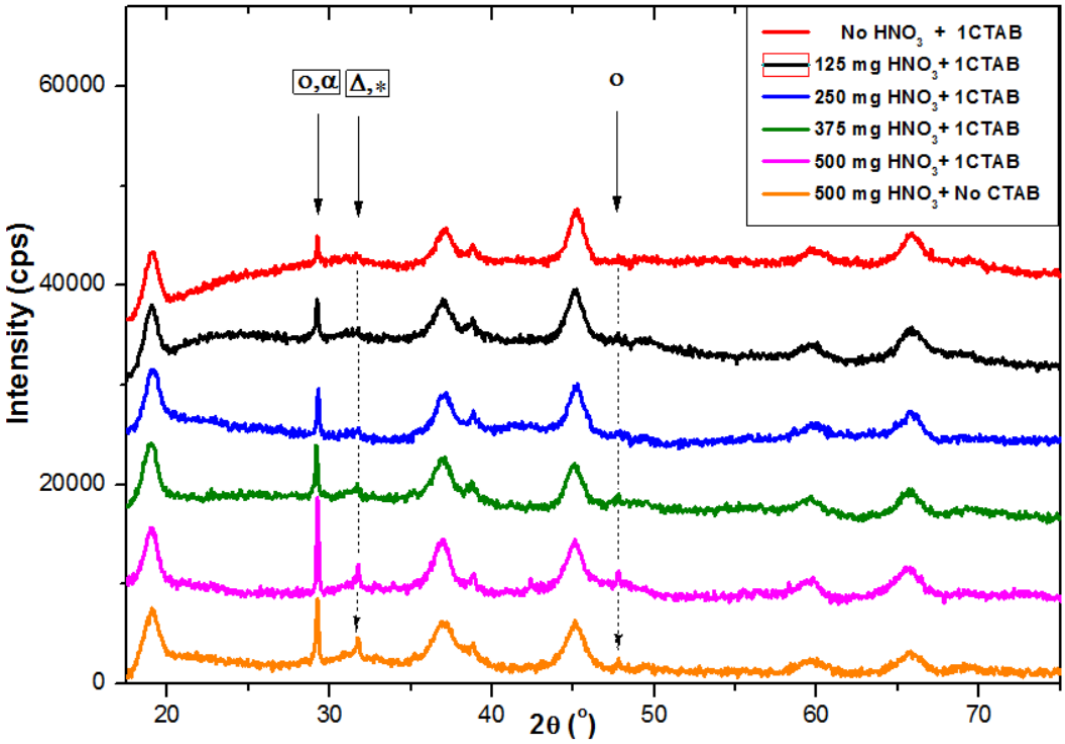

Figure 16: XRD pattern of the powders obtained using different amounts of HNO_3 with/without CTAB-calcined at 300 ºC for 3 hours. (o: lines of CoO, α: line of $CoBr_2.H_2O$, *: line of $CO_3O_4$and Δ: line of Li_2O are the assignments of side products)

As it is shown in Figure 16, contrary to the expectations, with increasing acid amount the intensity of the lines of side products are also slightly increasing and removal of CTAB also did not cause a distinctive change on the peak intensities. This could be due to H_2O in the concentrated HNO_3 solution. As mentioned before, the samples prepared using H_2O as solvents form side products more than the ones prepared using ethanol. Presence of H_2O somehow might trigger the formation of Co_xO_y species. Since no positive effect has been measured with the

addition of acid to the media, the HNO_3 addition was excluded from the preparation of solutions.

3.1.6 Optimization of the calcination temperature

In this section, the calcination process will be discussed to investigate the effect on the structure and pore size of the target material and formation of the side products. Calcination process is important since all volatile and burnable raw materials (surfactants, metal nitrates, and ethanol) are processed at this step. During calcination, the organic species burn in air and form CO_2 and CO gases, metal nitrates decompose to M_xO_y and NO_x and the target material is obtained by further reactions. Determining the optimum calcination temperature is important since the temperature must be high enough to get rid of all the organic molecules and to complete all the reactions in order to eliminate formation of side products. However, it must also be kept at a certain temperature to preserve the mesoporous structure of the target material without collapsing due to further crystallization and growth.

To determine the formation temperature of $LiCoO_2$ mesostructure, a solution was prepared at 9 salt/surfactant mole ratio and spin coated on a Si wafer. The Raman and IR spectra of a heat-treated sample from 50 ^oC to 300 ^oC have been collected, Figure 17 and 18.

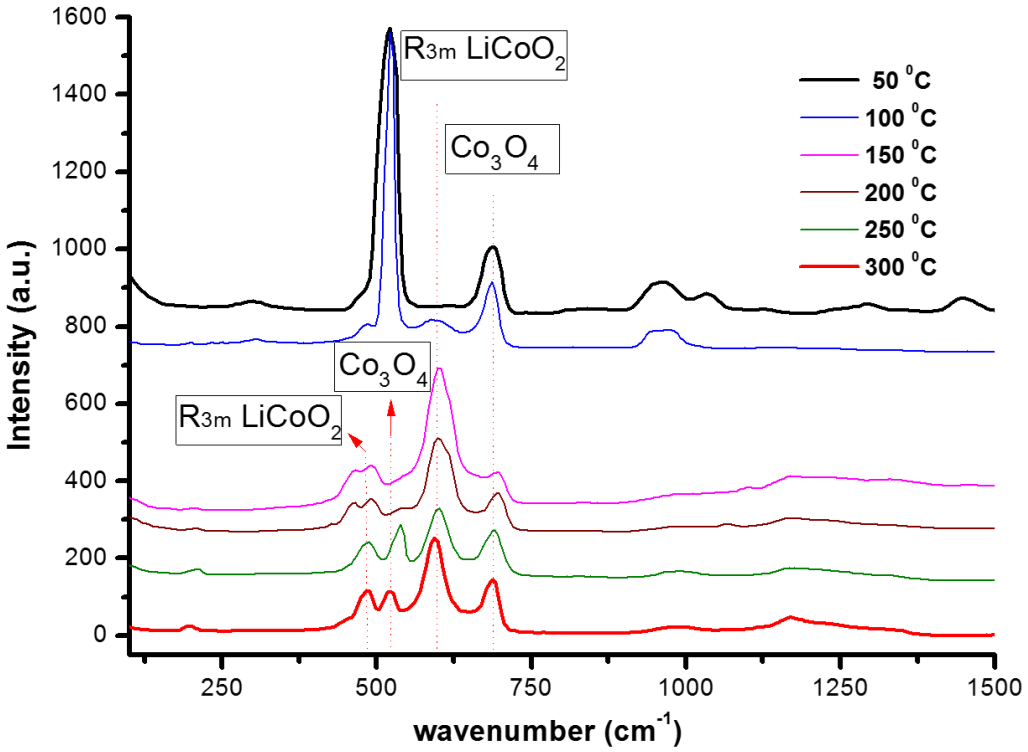

Figure 17: Raman spectra of LiCoO2 sample calcined at different temperatures

It is seen in Figure 17 that the peaks located at 521 cm^{-1} and 940 cm^{-1} are from Si substrate and no other significant peaks from the sample at 50 ºC. It means the sample is still in the liquid crystalline form and salts do not leach out of the mesophase. At 100-150 ºC, the broad peak appeared around 690 cm^{-1} and the shoulder appeared at 488 cm^{-1} are attributed to the most intense A_{1g} mode and Eg mode of Co_3O_4 respectively [96]. Note that the most intense T_{2g} mode of Li_2O and T_{2g} mode of Co_3O_4 are also located at 521 cm^{-1} [98]. At 200 ºC, a new peak formed at 468 cm^{-1} and the shoulder at 672 cm^{-1} could be attributed to the Raman active modes of CoO[98]. The broad peak located at around 590-620 cm^{-1} could be due to the most intense Raman active mode of R3m $LiCoO_2$ (597 cm^{-1}), T_{2g} mode of Co_3O_4 (618 cm^{-1}) and CoO (605 cm^{-1}) [95]. At 300 ºC, the peak located

at 468 cm^{-1} from CoO disappeared and the others became more distinctive. According to Figure 17, it could be concluded that the formation temperature of $LiCoO_2$ is around 200 ^oC. However, in order to minimize the formation of side products, the temperature must be increased further.

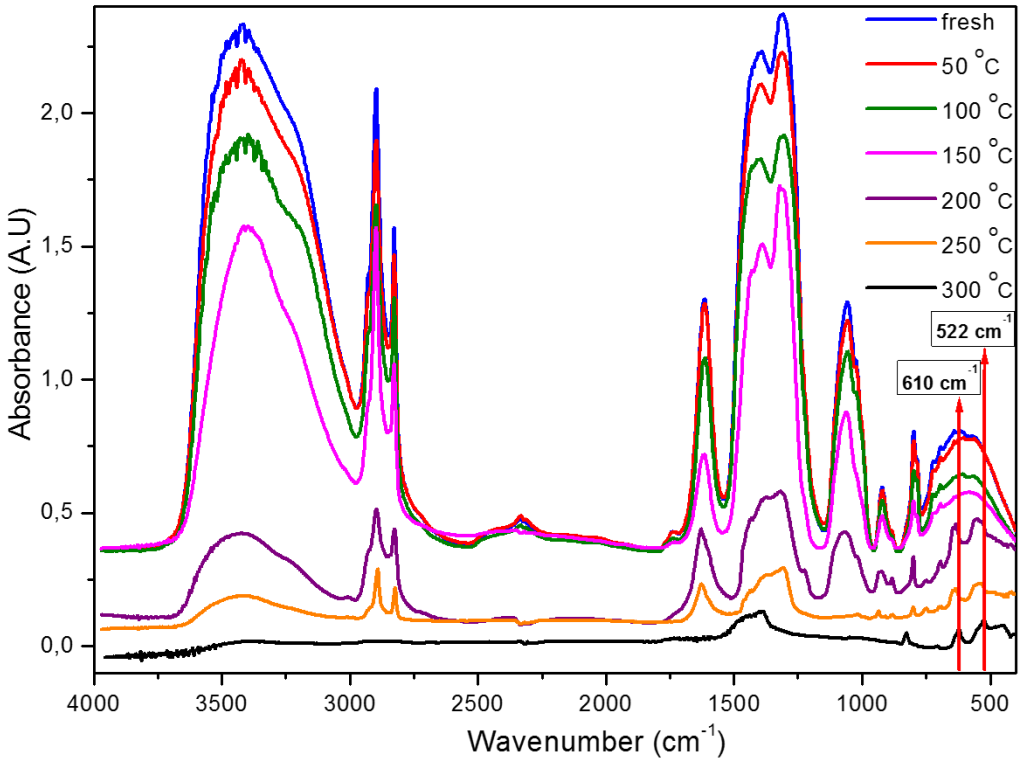

Figure 18: IR spectra of the heat-treated sample coated on Si wafer

In Figure 18; IR spectra also confirms the formation temperature of $LiCoO_2$ starts at around 200 ^oC due to the characteristic peaks of $LiCoO_2$ raised around 522 cm^{-1} and 610 cm^{-1} [99]. However; the peaks due to presence of surfactants, H_2O and NO_3^- ion disappear at 300 ^oC. Therefore; the minimum calcination temperature for the synthesis has been set to 300 ^oC for $LiCoO_2$.

3.1.7 Optimization of the pore size and surface area with respect to the amount of the salt

In order to examine the change in pore size and surface area of the $LiCoO_2$ mesostructure with increasing precursors, the high angle XRD and BET measurements of the samples have been recorded. The salt amounts were set to 4.5, 6, 9, 12, and 15 (Li + Co):$C_{12}EO_{10}$ mole ratios.

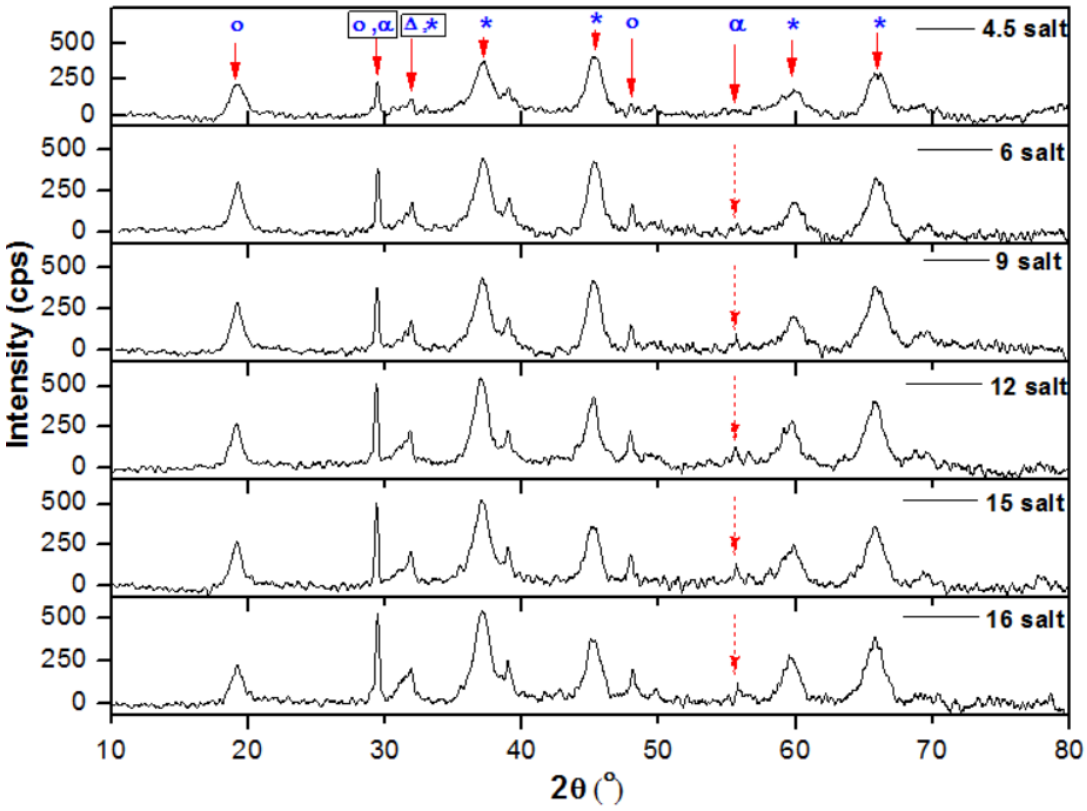

Figure 19: High angle XRD patterns of the samples with increasing salt amounts. o: lines of CoO, α: line of $CoBr_2.H_2O$, Δ: line of Li_2O and *: lines of CO_3O_4
The sample sets were spin coated and calcined at 300 ^oC for 3 hours.

In Figure 19; all the lines of side products are getting sharper and more intense which points out an increase in the formation of side products and larger crystals. Increasing intensity of the line at 29.7^o could be due to excessive CoO

formation. The lines of Co_3O_4 assigned with " * " and the line located at 32.2° from Li_2O also increased in intensity. The lines of the possible side products are assigned by using o, α, Δ and * signs.

The Raman spectra of the samples in Figure 20 also confirms the outcomes of XRD patterns. As it is seen in the figure; with increasing salt amounts, the peak located at 691 cm^{-1} (attributed to Co_3O_4) slightly broadens and red-shifts with a shoulder around 672 cm^{-1}, which is attributed to Raman active mode of CoO. Notice also that the peak located at 468 cm^{-1} is also another strong Raman active mode of CoO.

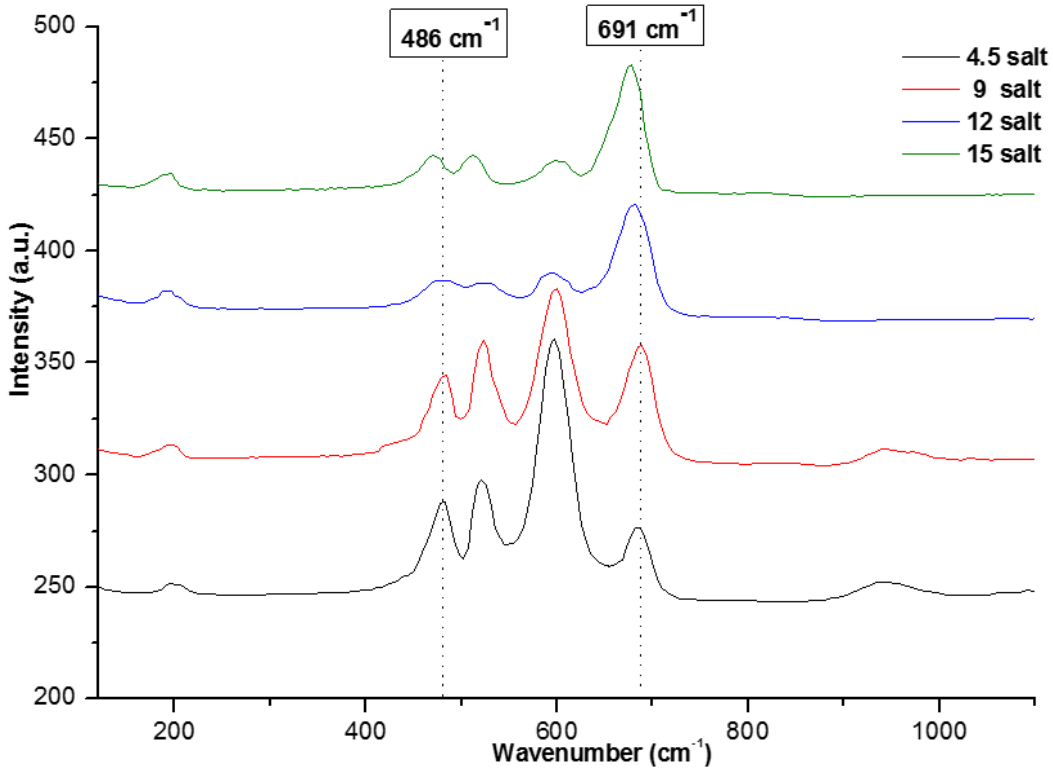

Figure 20: Raman spectra of the samples prepared with increasing salt amounts

The N_2 sorption data of the same samples were examined. The specific surface areas of the samples were measured as 44 m^2/g, 48 m^2/g, 57 m^2/g, 9 m^2/g and 3 m^2/g with increasing salt ratio from 4.5 to 15, respectively, see Figure 21.

The surface area of the mesostructures increase from 4.5 to 9 salt ratio since up to this salt amount formation of side products are limited and much less crystals form. For 12 and 15 salt:surfactant ratios, the reason might be both the over formation of side products and higher quantity of precursors that might lead a thicker pore walls and uncontrollable crystal growth of the target material. According to Raman spectra; the peaks of target material are getting weaker which means the second case is unlikely to happen.

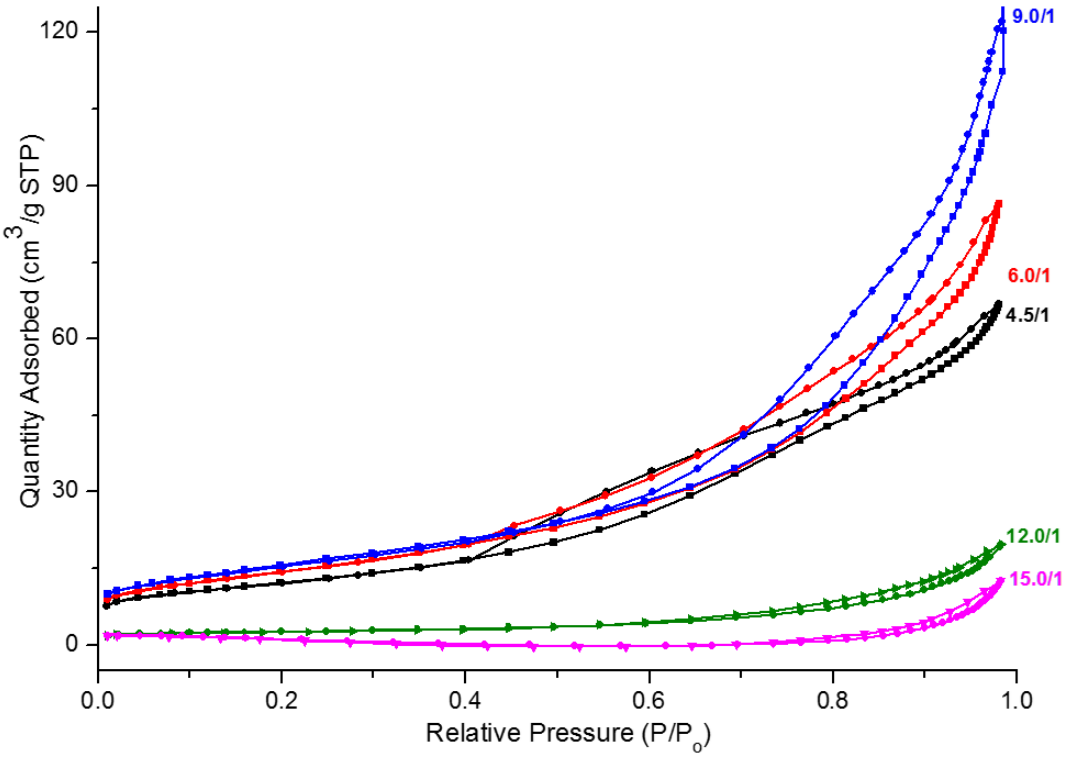

Figure 21: Isotherms of samples with increasing precursors

The pore size distribution of the samples is shown in Figure 22. The desorption BJH pore sizes were measured as 6, 9, 15, 16, and 20 nm from the same samples with pore volumes of 0.10, 0.11, 0.24, 0.03 and 0.02 cm^3/g, respectively.

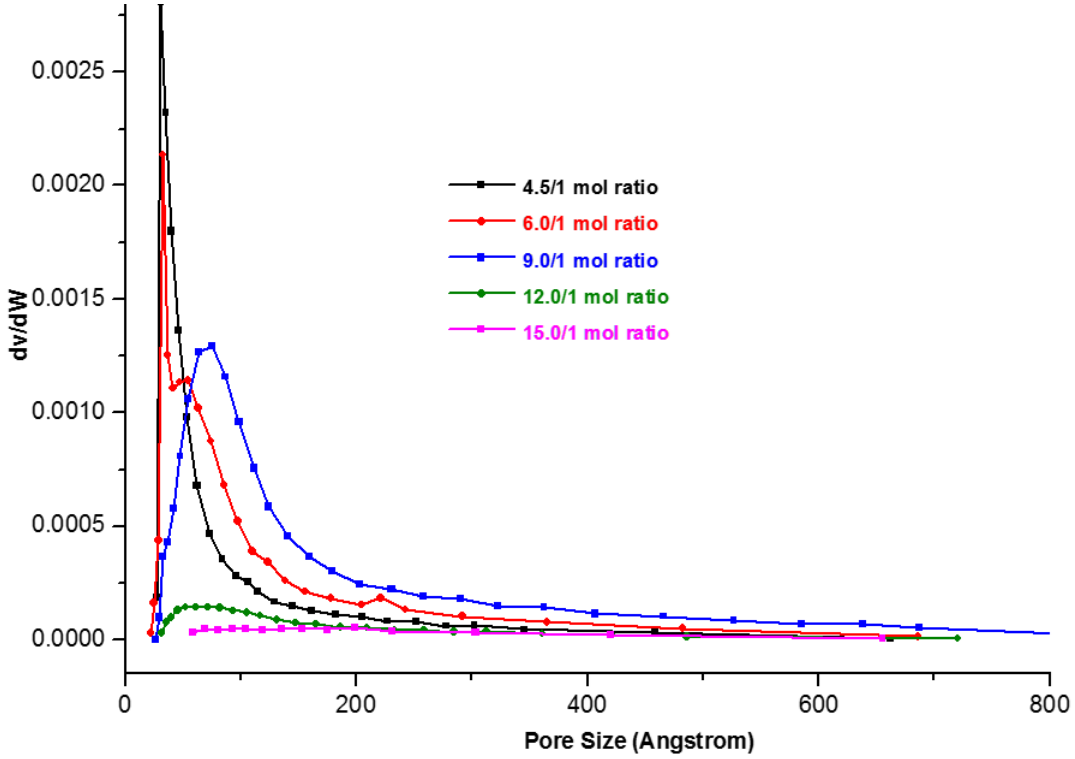

Figure 22: Pore size distribution of the samples with increasing salt amounts

According to Figure 22; the pore size is more uniform at lower salt compositions since there are less amount of side products. With increasing salt amounts the pore size distribution gets broader due to excessive formation of bulky side products. As a result; although fresh films of the higher salt:surfactant compositions don't leach out any salt for a long time, formation of the side products directly proportional with the salt:surfactant ratio.

3.1.8 Effect of calcination temperature on the pore size and surface area

The samples of 9 salt/surfactant mole ratio were calcined at different temperatures to investigate the effect of calcination temperature on structural properties and pore size/ surface area of the mesoporous $LiCoO_2$. Raman spectra

of the samples coated on Si substrate and calcined at different temperatures are seen in Figure 23.

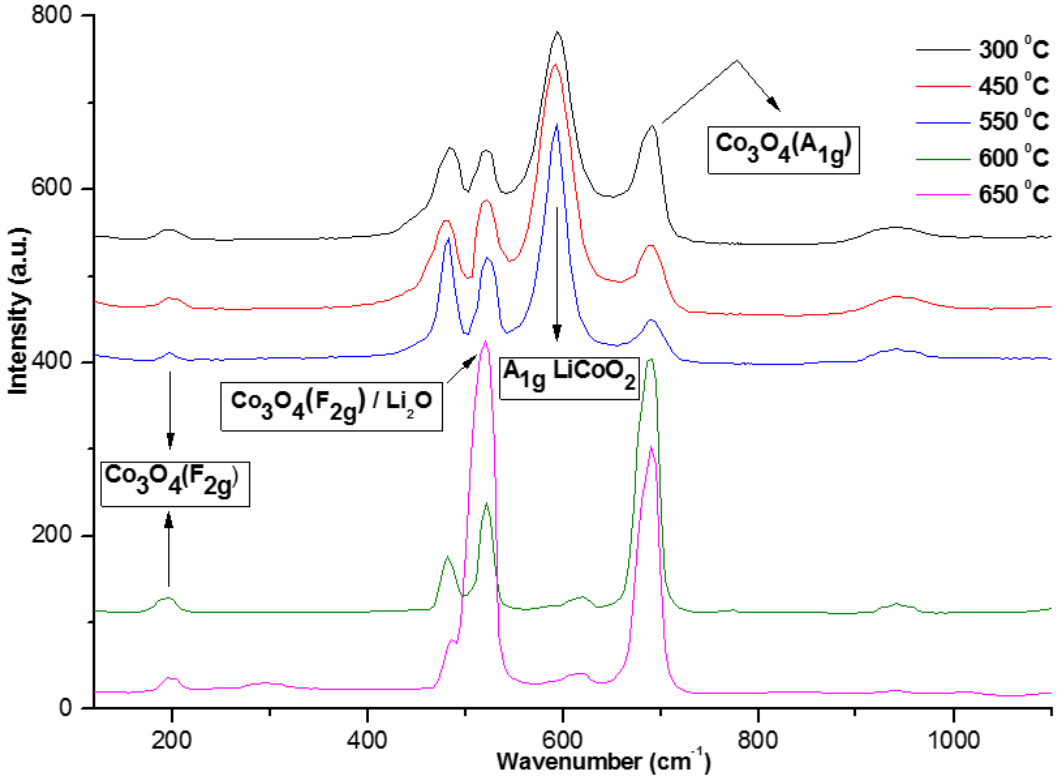

Figure 23: Raman spectra of the samples coated on Si substrate and calcined at different temperatures**.**

With increasing calcination temperature, the Raman peaks of mesoporous $LiCoO_2$ get stronger and sharper pointing out the formation of larger crystalline structures meanwhile the peaks of Co_3O_4 and the peak located at 941 cm^{-1} (might be due to $CoBr_2$ as mentioned before) are getting weaker, indicating the decrease in amount of foregoing side products up to 550 ^oC, see Figure 24. After this temperature, the peaks of $LiCoO_2$ (483cm^{-1} and 597cm^{-1}) are getting weaker and the ones attributed to Co_3O_4 and Li_2O (521 cm^{-1} and 691 cm^{-1}) are getting more intense. The reason could be due to decomposition of the $LiCoO_2$ to Li_2O and Co_3O_4. The decomposition temperature of bulk R_{3m} $LiCoO_2$ is $\geq$ 900 ^oC.

However, this temperature could be suppressed to lower temperatures for nanocrystalline structures.

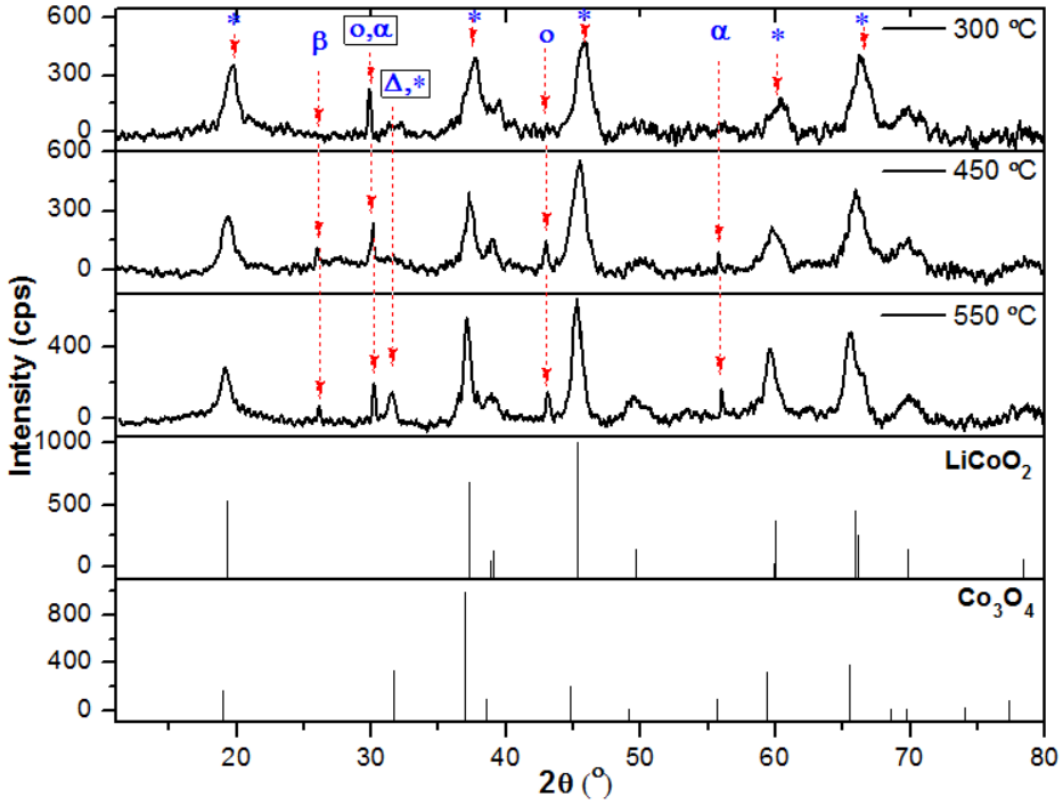

Figure 24: High angle XRD patterns of the samples calcined at different temperatures. o: line of CoO, Δ: line of Li_2O, *: line of CO_3O_4, α: line of $CoBr_2.H_2O$ and β: line of $LiBrO_2$ are the assignments of side products.

The high angle XRD patterns of the samples calcined at 300 °C, 450 °C and 550 °C were also collected, see Figure 24. The XRD data also confirm the similar outcomes. All the lines are getting sharper and more intense implying further crystallization. The lines that assigned to side products are getting weaker but not disappeared. In other words; increasing calcination temperature did not prevent formation of side products.

Then, N_2 sorption measurements of the same samples have been carried to monitor the effect of temperature on pore size, wall thickness and surface area of the samples, Figure 24.

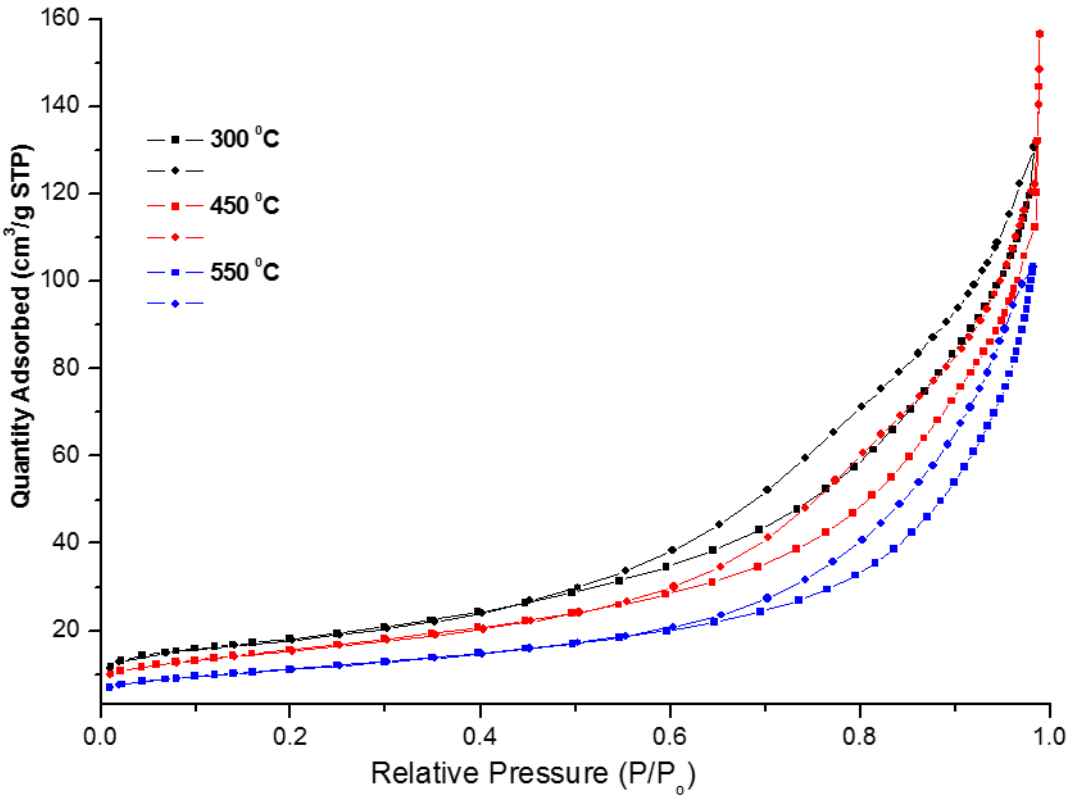

Figure 25: Temperature dependent isotherms of mesoporous $LiCoO_2$.

The specific surface area changes from 60 m^2 /g to 56 m^2/g and to 41m^2/g with increasing calcination temperature which is ascribed to formation of larger crystals at higher temperatures. The pore size increased with calcination temperature and given as 10, 15 and 16 nm at 300, 450, and 550 ^oC, respectively. The corresponding pore volumes are 0.24, 0.20 and 0.16 cm^3/g at 300, 450, and 550 ^oC respectively. This reverse trend between pore size and pore volume indicates that while the pores are expanding, the walls of the mesostructure are getting thicker. The pore size distribution of the same samples is shown in Figure 26.

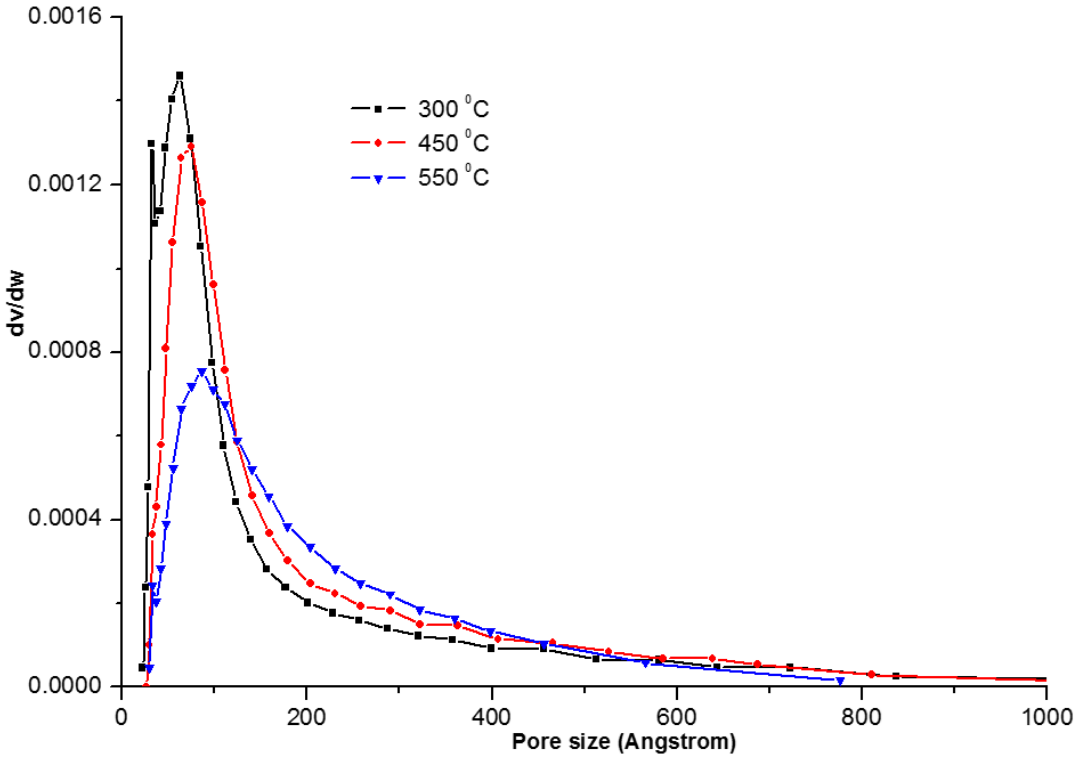

Figure 26: Pore size distribution of the samples calcined at different temperatures.

As it is illustrated in the Figure 26, the pore size distribution plot gets broader with increasing temperature. In other words; the calcination temperature and uniformity of the pore size are inversely proportional which shows some of the pores coalesce with neighboring ones and form larger pores with increasing wall thickness of the mesostructure. As a result; the mesostructure synthesized by using MASA method is stable up to 550 ^{o}C and less uniform and disordered mesostructures with higher crystallinity are synthesized via higher calcination temperatures.

3.1.9 CTAB effect on pore size distribution

As mentioned before, being a charged surfactant, CTAB; stabilizes the charge distribution and increases the salt uptake of the mesophase in the fresh

samples. In order to analyze the effect of CTAB on pore size distribution of the mesoporous $LiCoO_2$, 6 different samples containing 4.5, 6, and 9 salt ratios with/without CTAB have been calcined at 450 ^oC for 1 hour. In Figure 27, the pore size distribution plots of these samples are given.

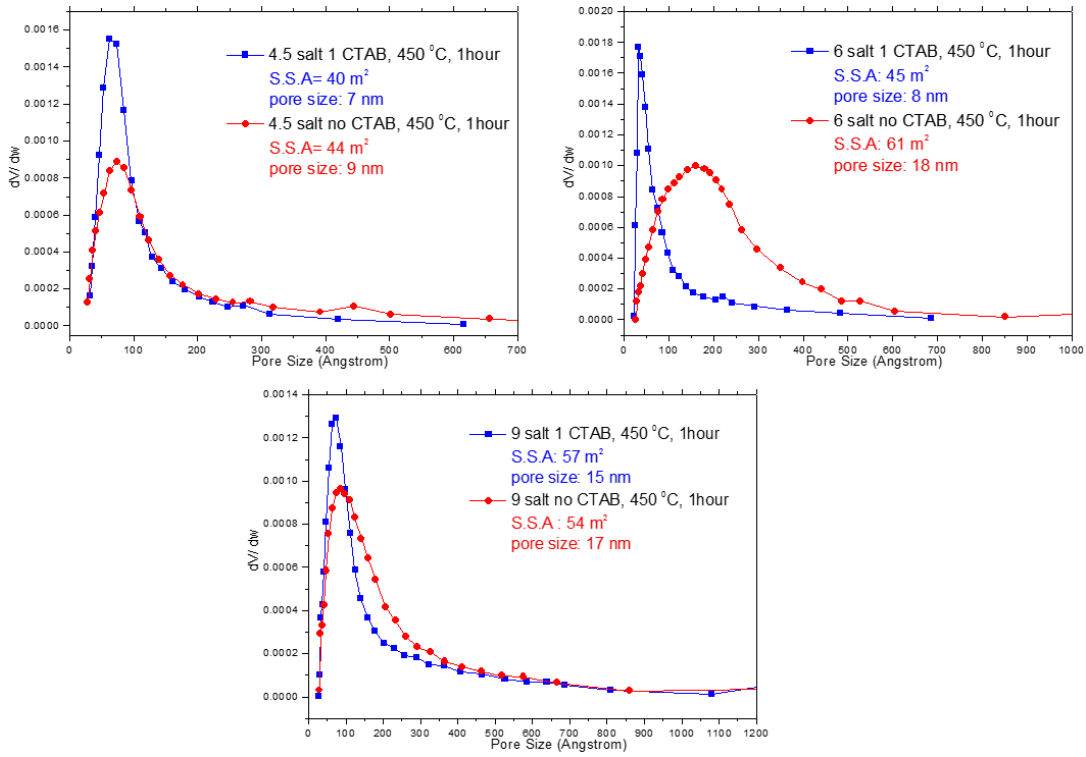

Figure 27: Pore size distribution plots of the samples having 4.5, 6, and 9 salt compositions (as indicated in the plots).

In the figure, the samples with the same mole ratios, the pore size decreases and size uniformity increases with the addition of CTAB. In other words; using CTAB helps the formation of ordered and uniform structures that are important for various applications of the mesoporous materials. Therefore, presence of a charged surfactant is crucial to obtain more ordered target materials.

3.1.10 Br^- effect on side product formation

In order to analyze the effect of Br^- ion on the formation of side products, the solutions prepared with/without CTAB have been examined. In Figure 28; a wine-colored solution prepared without CTAB and a violet colored solution prepared with CTAB could be seen. Usually, the wine color appears due to formation of hexaaqua complexes of Co(II) ions. The violet color of the other solution attributed to the contamination of blue color due to tetrahedral symmetry of Co(II) coordinated to halogens like Br^-, Cl^- etc together with hexaaqua complexes.

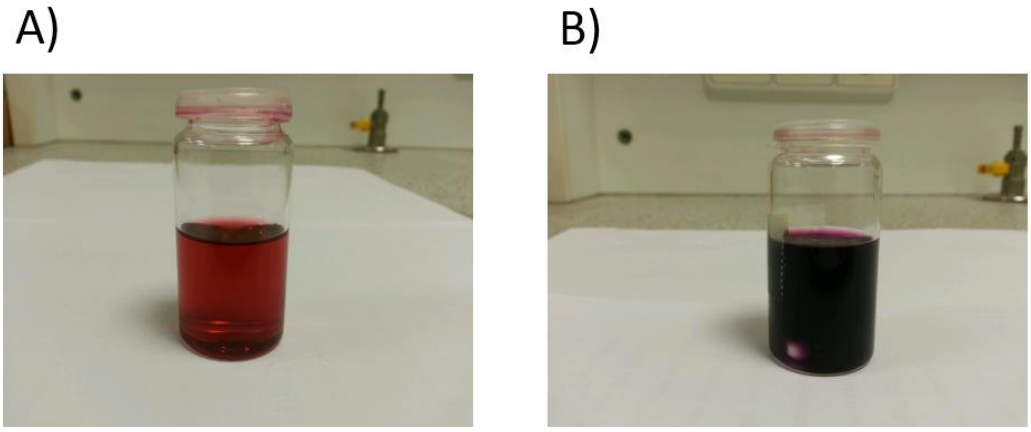

Figure 28: A) Solution prepared without CTAB and B) Solution prepared with CTAB

UV-Vis spectra of the same solutions is shown in Figure 29; in both samples there are broad absorption peaks in the range of 450 to 600 nm due to octahedral symmetry of $[Co(H_2O)_6]^{2+}$. However, in the case of the sample containing CTAB, there are also fingerprint absorption bands of tetrahedral $[CoBr_4]^{2-}$ ion in between 550 to 750 nm which points out the formation of the complex $[CTA]_2CoBr_4$ in the mesophase.

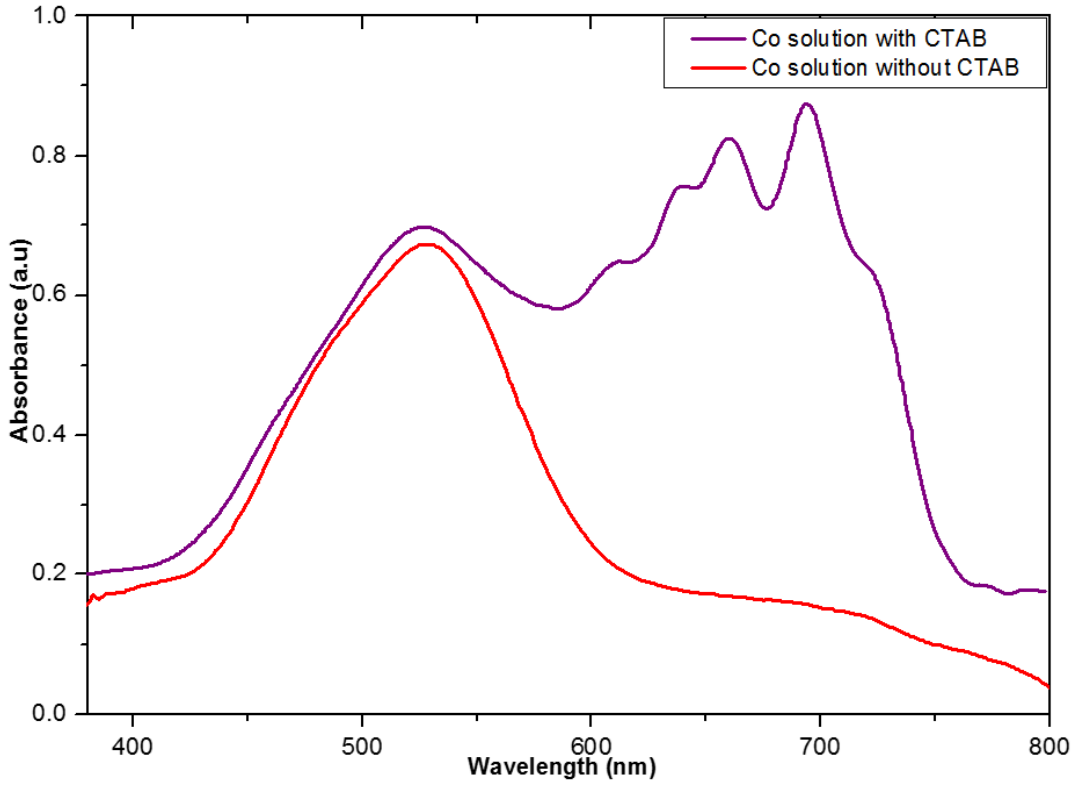

Figure 29: UV-Vis spectra of the fresh samples prepared with/ without CTAB

Then, Br^- amount was increased 4 times by using $CoBr_2$ as Co source and samples of 9 salt/surfactant mole ratios with/without CTAB, see the compositions in Table 1. These samples were calcined at 400 ^oC for 3 hours to determine the effect of the formation of $[CTA]_2CoBr_4$ complex.

	$CoBr_2$:$C_{12}EO_{10}$ mole ratio	**$Co(NO_3)_2.H_2O$:$C_{12}EO_{10}$ mole ratio**	**CTAB:$C_{12}EO_{10}$ mole ratio**	**Co :$C_{12}EO_{10}$ mole ratio**
S1	**0**	**4.5**	**1**	**4.5**
S2	**2**	**2.5**	**0**	**4.5**

Table 1: The composition of the samples S1 and S2

Upon XRD measurements, the powders were washed with distilled water by suction, dried samples have been examined once more and the results have been compared.

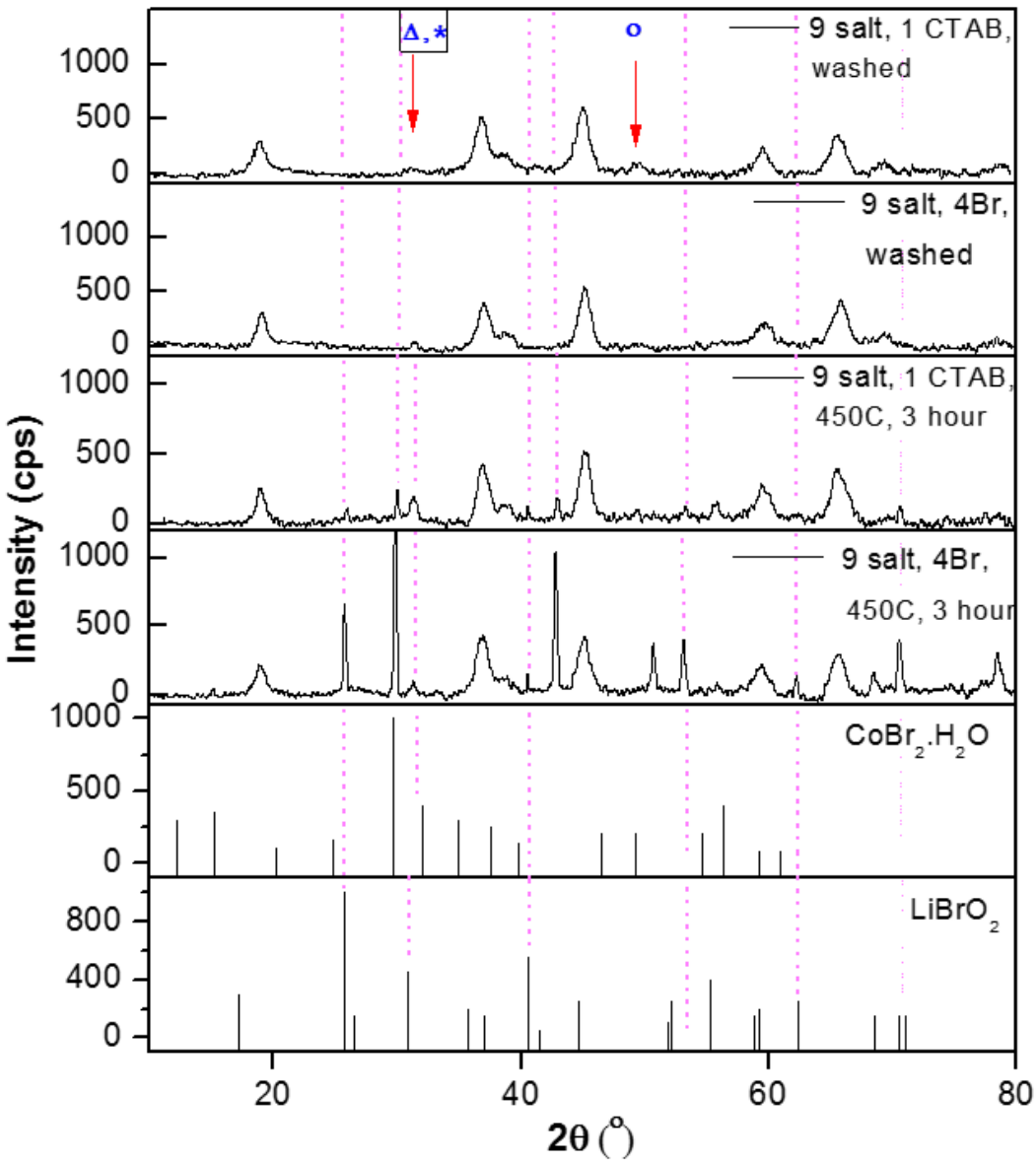

Figure 30: XRD pattern of the powders with different compositions o: line of CoO, Δ: line of Li_2O and *: line of CO_3O_4 are the assignments of side products.

According to the XRD pattern shown in Figure 30, there are sharp lines belong to unknown products in the sample containing CTAB. It could be seen that the intensity of these sharp lines increased and some others formed with

ascending Br^- amount in the sample containing $CoBr_2$. In other words, presence of Br^- ion caused formation of bulk crystals of water soluble side products like $CoBr_2.H_2O$, $LiBrO_2$ etc. Moreover; bulk $CoBr_2$ does not react under air even at 678 ^oC[100].

However; due to soft confinement effect; this temperature might be suppressed to the lower values leaving oxide forms of relevant metals behind as side products. After washing the samples, the sharp peaks due to these side products have been disappeared, clearly indicating that these side products are unreacted salt species. However; some other peaks which are consistent with Li_2O, Co_3O_4 and CoO are still present for both the samples after washing.

A)

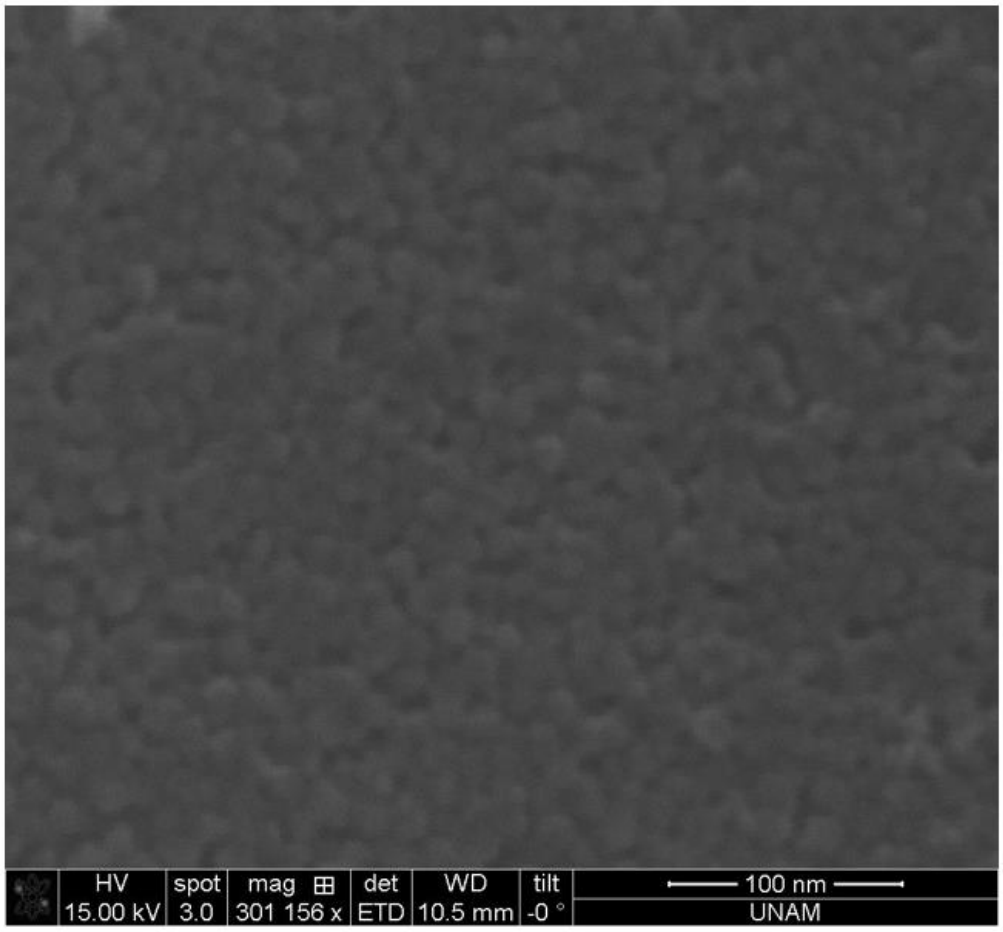

B)

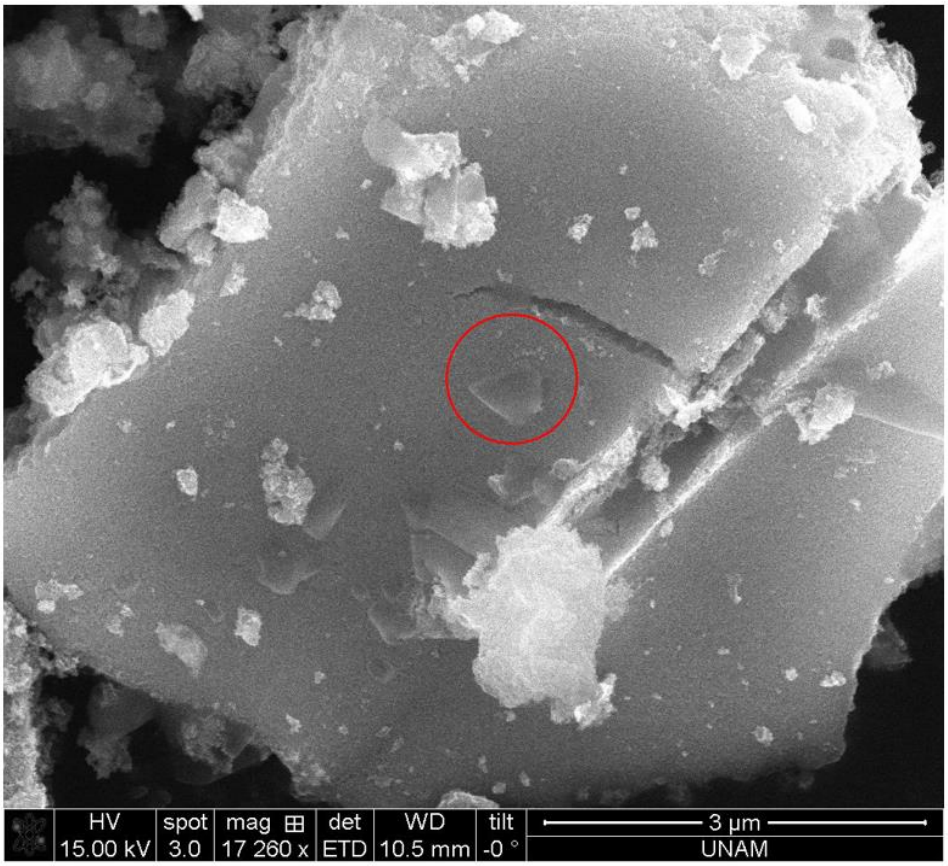

C)

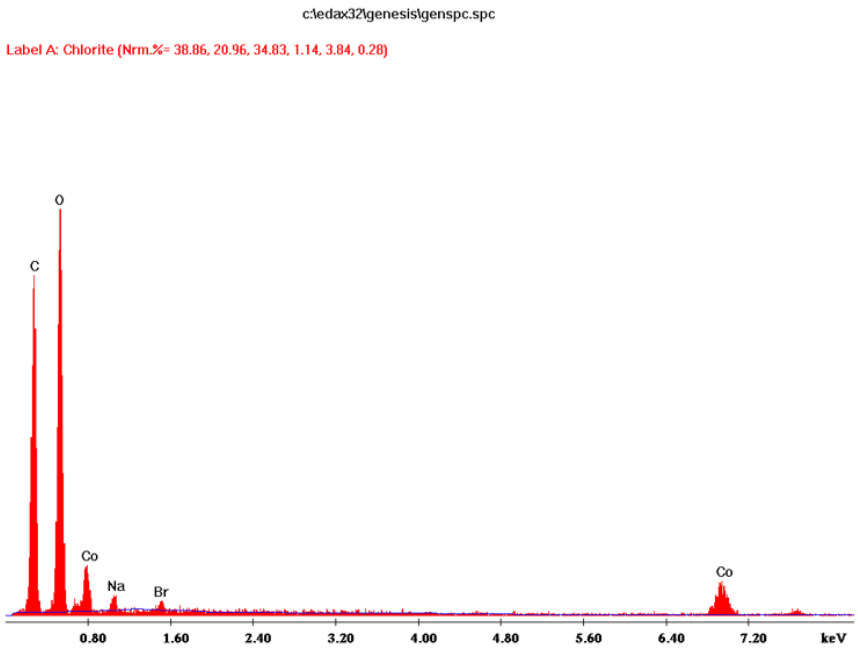

Figure 31: A), B) are SEM images of the sample having 4.5 salt ratio prepared with CTAB and C) EDAX of the area shown in red circle in B).

The SEM images of the sample having 4.5 salt amount prepared using CTAB are shown in Figure 31(A and B). In Figure 31(A), it is clearly shown that the sample is composed of spherical particulates and it is mesoporous. In Figure 31(B), there are small unknown side products having different crystalline structures and distinctive shapes on the uniform mesoporous film of $LiCoO_2$. In Figure 31(C), the EDAX of the area shown in red circle has been given to make it easy to identify the unknown crystals. As it is shown, a small amount of Br is also in the structure of the crystal which verifies the results obtained via XRD measurements.

3.1.11 Samples prepared using CTAN

The necessity of using charged surfactant have been discussed in section 3.12. In order to eliminate the effect of Br^- ion on side product formation, CTAN (cetyl trimethyl ammonium nitrate) has been synthesized by changing Br^- ion with NO_3^- ion as described in experimental part. The IR spectra of CTAN and CTAB is shown in Figure 32.

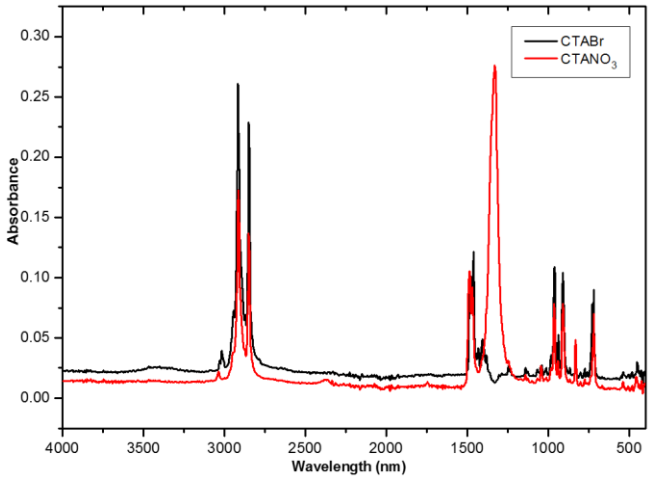

Figure 32: IR Spectra of CTAN and CTAB

In the figure; the absorption peak of NO_3^- around 1324 cm^{-1} could be seen distinctively and there are XRD patterns of CTAB and CTAN in Figure 33. XRD patterns show that both crystals have the same crystal structure that display a very similar diffraction patterns with a slight change on the unit cell parameters.

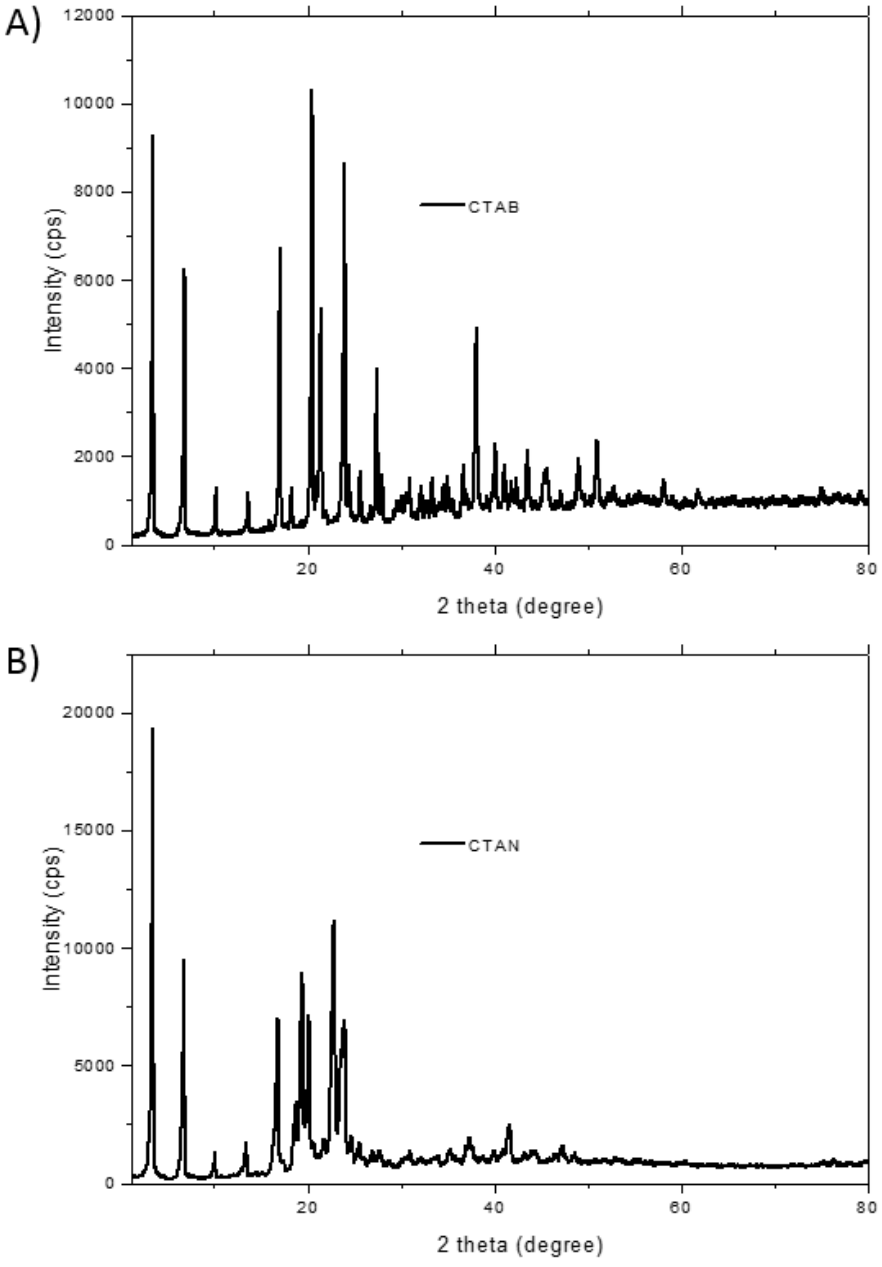

Figure 33: XRD Pattern of CTAB and CTAN

A set of samples were prepared using CTAN in place of CTAB to identify the side products. In Figure 34(A); 2D hexagonal POM texture of the fresh

sample of 6 salt ratio prepared with CTAN have been calcined and the image in Figure 34B) has been obtained. As it is shown the texture of the film could be preserved during calcination and diffraction on the small angle XRD pattern seen in Figure 35 also verifies that calcined films have an order in their structures.

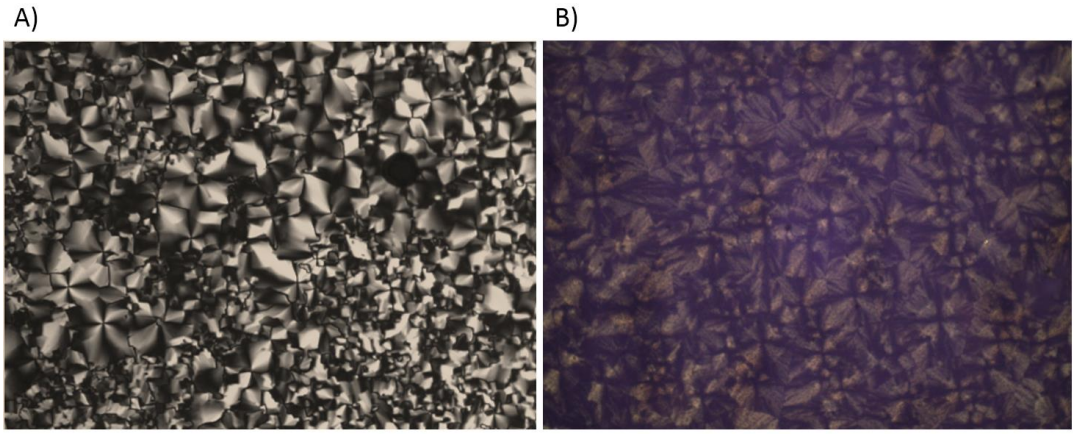

Figure 34: POM images of the 2D hexagonal (A) fresh film and (B) a calcined film of the sample prepared using CTAN.

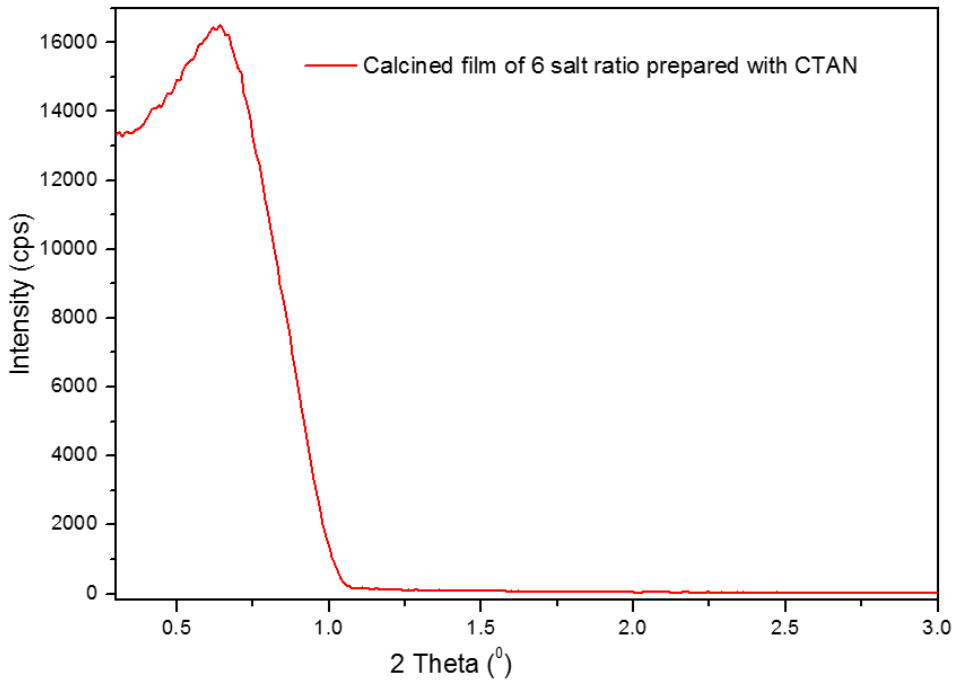

Figure 35: XRD pattern of a calcined film of a 6: 1 sample prepared with CTAN.

In order to understand the effectiveness of CTAN for the synthesis of $LiCoO_2$, a set of samples having the same salt ratios (9 salt ratio) but different or no ionic surfactants have been compared in Figure 36.

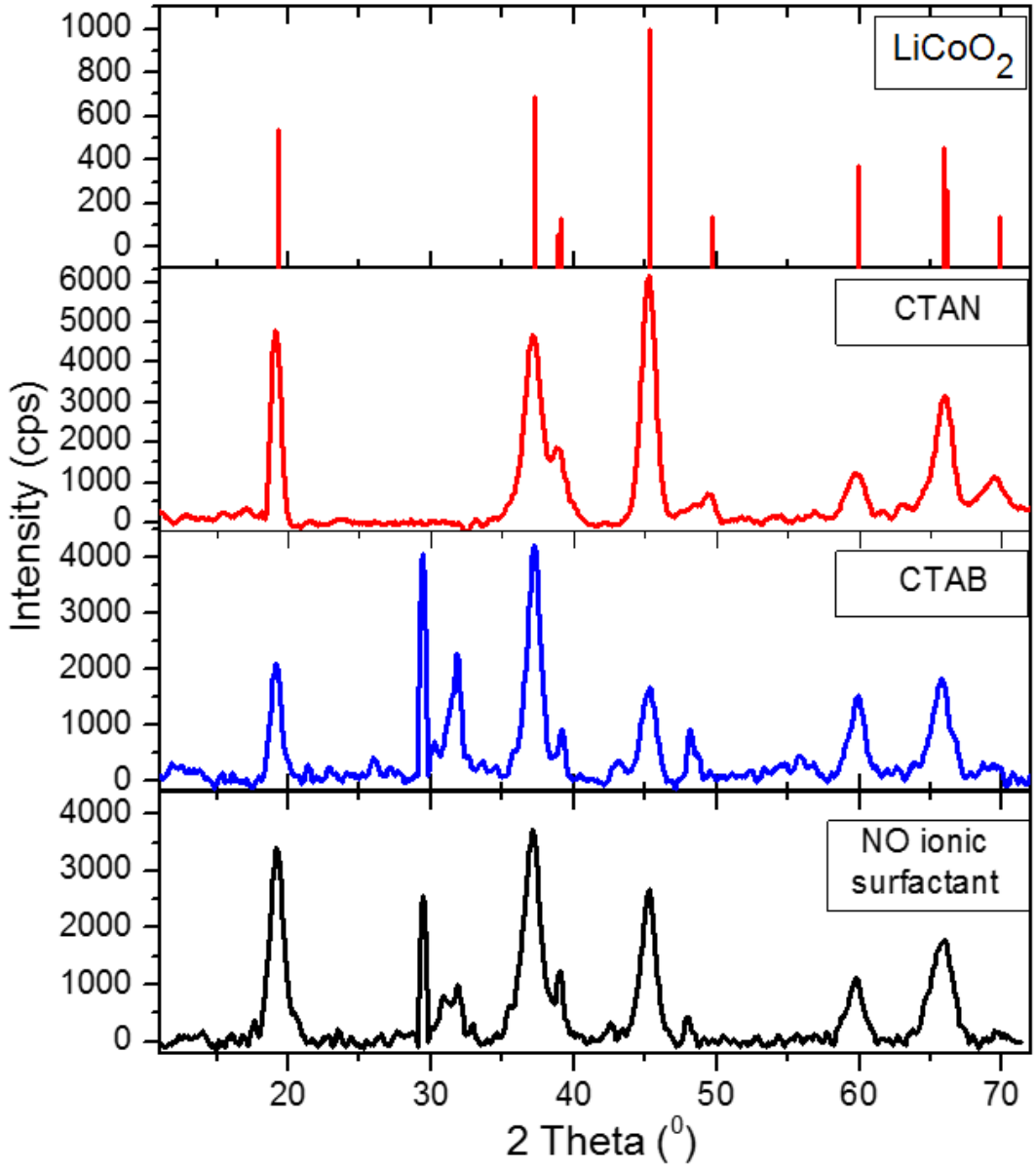

Figure 36: XRD pattern of different 9 salt ratio samples prepared with CTAB, CTAN and without an ionic surfactant calcined at 350 ^oC for 3 hours.

According to Figure 36; the samples prepared using CTAB or without any ionic surfactants have extra lines coming from the side products and the lines of $LiCoO_2$ have different intensities than the ones on the JCPDS PDF card.

However; the sample prepared using CTAN has only lines coming from the targeted material and their intensities accords with the ones on the JCPDS PDF card.

Presence of the bulk side products would be expected to decrease the specific surface area of the samples. Figure 37 shows the pore size distribution plots of the samples prepared with CTAB, CTAN and without any ionic surfactant, calcined at 450 ^{0}C for 1 hour. It could be seen that the sample having no ionic surfactant has a nonuniform pore size distribution and the lowest surface area compared to others. In the case of the sample prepared with CTAN; the slight increase of the surface area from 57 m^2 to 65 m^2 might be due to lack of bulk crystals.

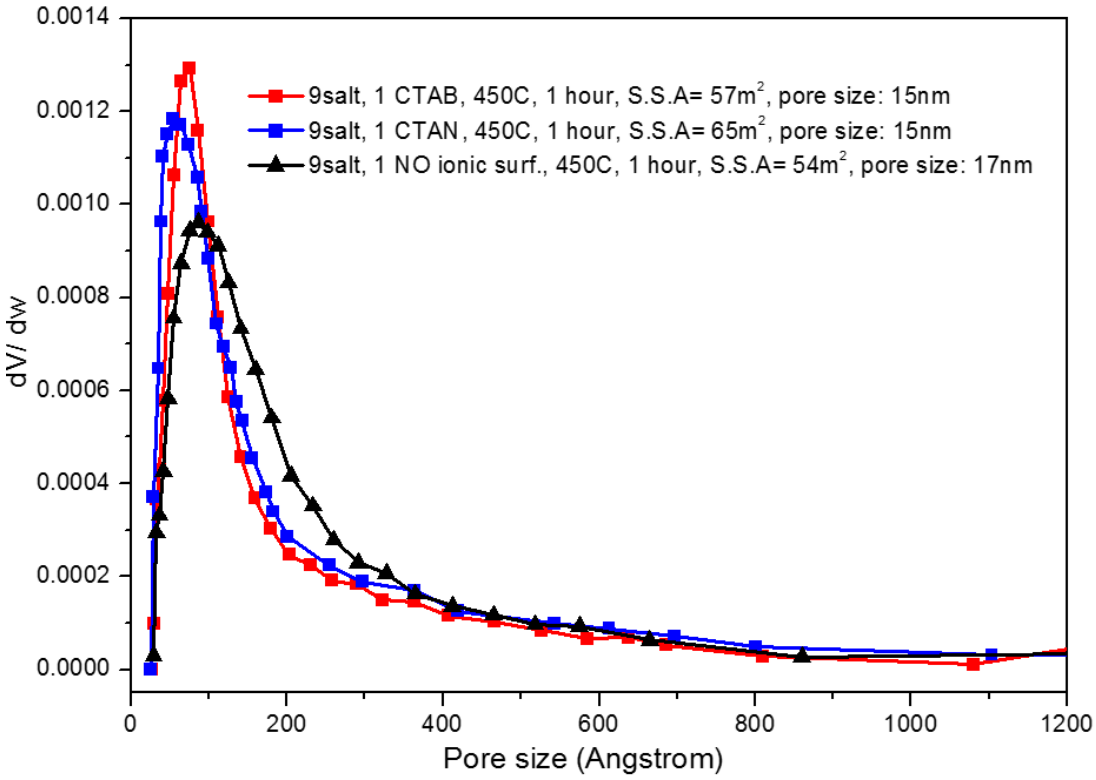

Figure 37: Pore size distribution plots of the samples prepared with CTAB, CTAN and without any ionic surfactant.

Furthermore; both CTAN and CTAB have similar roles on pore size distribution, building more ordered and uniform pores on the mesoporous material.

The TEM and STEM images of the samples (having 9 salt ratio, calcined at 450 ^{o}C for 1 hour) are shown in the Figures 38, 39(A-C). Crystalline structure of the $LiCoO_2$ is clearly visible in the images. Each crystalline domain is around 4-5 nm size.

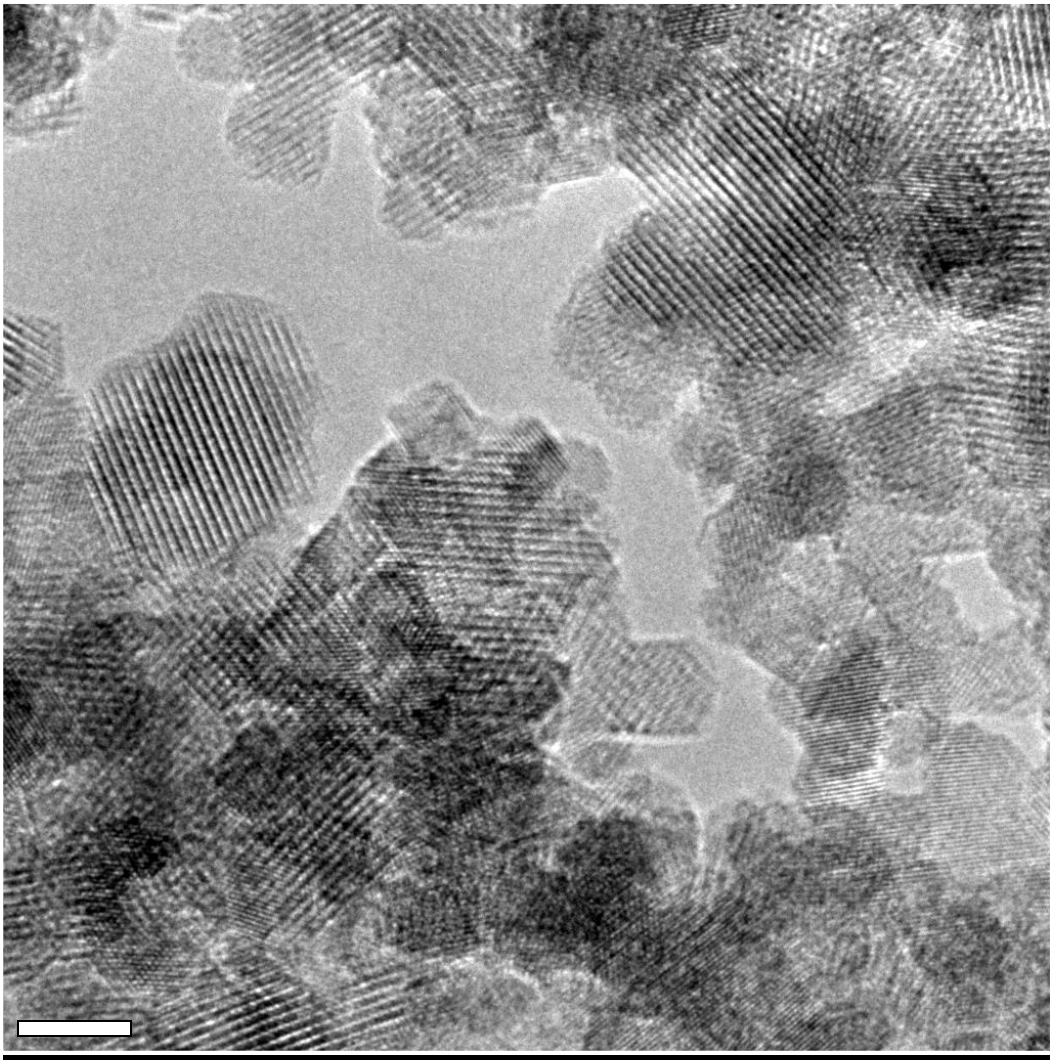

Figure 38: TEM image of the sample prepared at 9 salt ratio, calcined at 450^{0}C for 1 hour (scale bar is 5 nm).

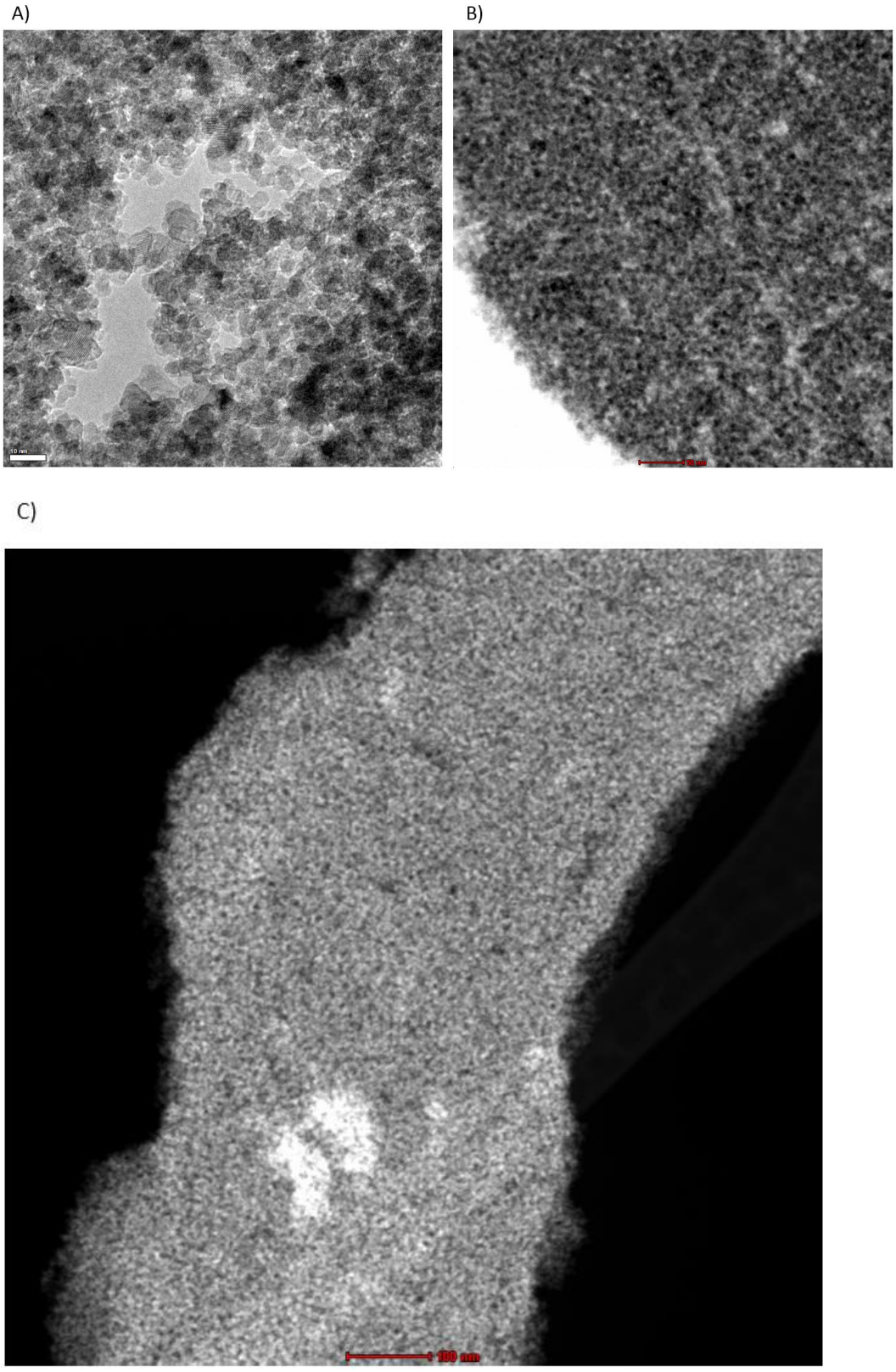

Figure 39: TEM image of the sample prepared at 9 salt ratio, calcined at 450 ^{o}C for 1 hour with a scale bar of (A) 10 nm (B) 50 nm and (C) STEM image of the same mesoporous $LiCoO_2$ film scraped from the substrate (scale bar is 20 nm).

Figure 39(A) shows the same area with a larger scale bar to identify the dimensions of the mesopores which is around 20-25 nm pore size. In figure 39(B), a higher magnification TEM image is seen to examine that the structure exhibits homogeneity and a sponge like formation throughout the film. The STEM image of the film scraped from the substrate is shown in Figure 39(C), also confirms both film like and sponge-like uniform structure of the sample.

3.1.12 Optimization of the calcination temperature of the $LiCoO_2$ prepared with CTAN

In order to identify the effect of temperature on formation of side products and pore size and surface area of the mesoporous $LiCoO_2$; 3 samples of 9 salt composition were calcined at 350, 400 and 450 ^oC for 10 hours respectively. The thin films were scraped form the substarates and their powders were analzed by XRD measurement,Figure 40. The duration of the calcination has been kept long to obtain visible bulk crystals of side products.

As it is shown in Figure 40; the samples start decomposing (to Li_2O and Co_3O_4) when the calcination temperature raised to 400 ^oC and the lines of side products became more distinctive when it increased to 450 ^oC. All the lines of the XRD patterns get sharper with increasing temperature as an outcome of increasing crystallinity, see Figure 40. As a result, in contrast with CTAB; in the case of CTAN; the temeprature should be decreased down to 350 ^oC's to obtain pure mesoporous $LiCoO_2$.

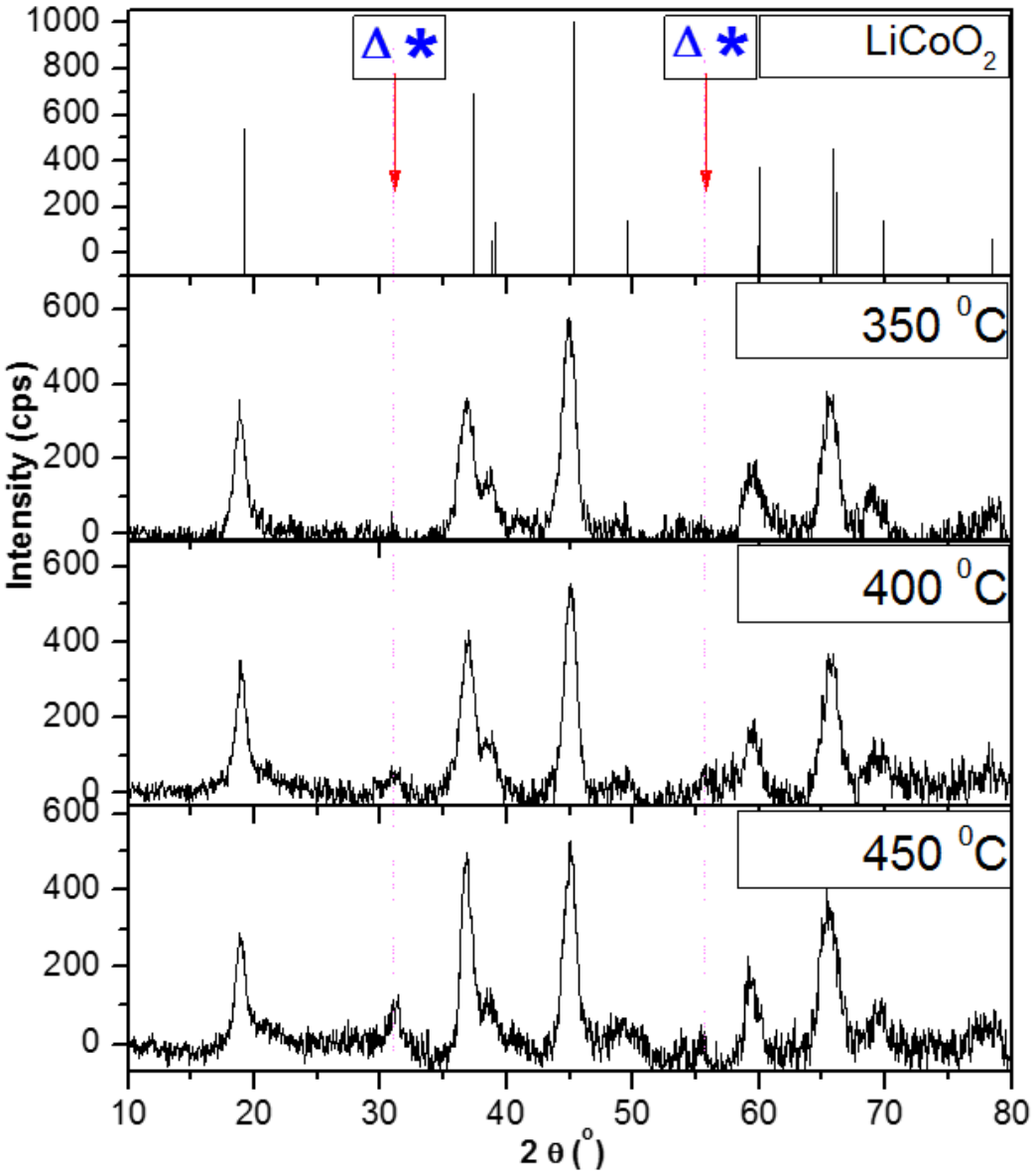

Figure 40: XRD Patterns of the samples having 9 salt composition, calcined at 350, 400 and 450 ^{0}C for 10 hours. Δ: line of Li_2O and *: line of CO_3O_4 are the assignments of side products.

Then, N_2 sorption measurements of the same samples have been examined to analyze the effect of temperature on pore size, wall thickness and surface area of the samples, Figure 41(A) and (B).

As it is seen; with increasing temperature, the specific surface are decreased from 58 to 48 and to 34 m^2/g, respectivelty.

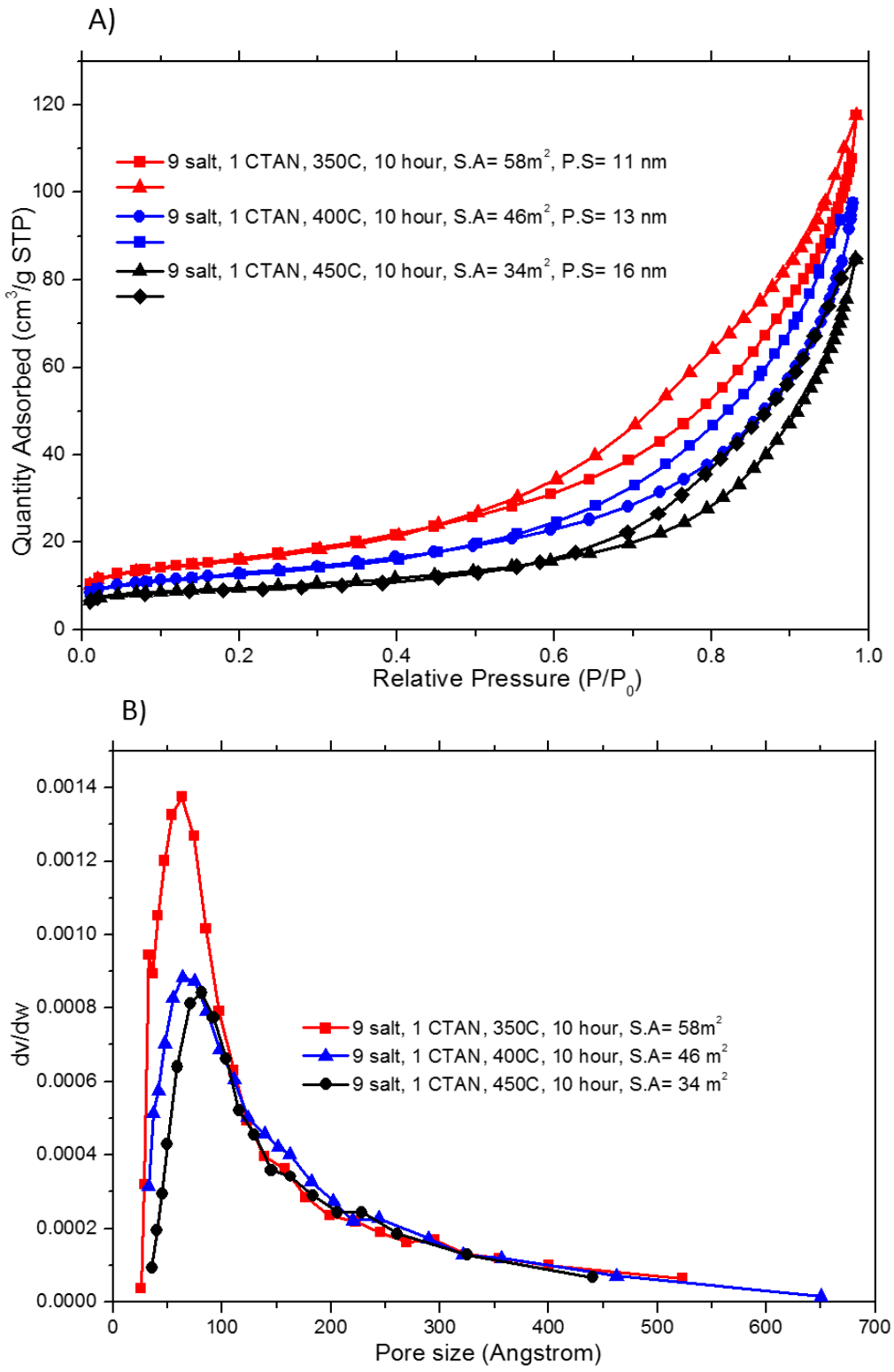

Figure 41: (A) N_2-sorption isotherms (B) pore size distribution plots of the mesoporous $LiCoO_2$.samples having same composition calcined at different temperatures prepared with CTAN.

Moreover; the pore size increased from 11 to 13 and to 16 nm by increasing the calcination temperature to 350, 400, to 450 ^{o}C, respectively. It points out further crystallization in the structure also confirms the XRD measurements.

3.2 The general synthesis method for the mesoporous $LiMn_2O_4$ thin films.

Certain amount of CTAB is dissolved in ethanol and the clear solution is stirred for 2 hours. Then; a mixture of salts ($LiNO_3$ and $[Mn(H_2O)_4](NO_3)_2$), HNO_3 and $C_{12}EO_{10}$ are dissolved in the same solution and stirred on a magnetic stirrer at least 12 hours until is a clear homogeneous solution that is spin coated on glass substrates to obtain a thin LLC mesophase on the substrates. The small angle XRD patterns and POM images of the fresh samples are recorded to determine the liquid crystalline order. These fresh LLC films are then calcined at 300 ^{o}C for 1-2 or 3 hours to obtain mesoporous $LiMn_2O_4$ monolith and powder. The small angle XRD measurements and POM images of the calcined films are also collected to determine the order of the mesostructure. Powder of these samples are obtained by scraping 60-80 slides of calcined films over the glass substrates. The powder is used to collect the high angle XRD patterns, Raman spectra, TEM images and N_2 sorption data for the characterization of the samples.

During the synthesis, several parameters that control the features like purity, pore size, surface area and crystallinity of the $LiMn_2O_4$ mesostructure have been optimized. These parameters are salt uptake, addition of acid, calcination temperature, calcination time and surfactant used for the synthesis.

In the next section; determination of salt uptake of the LLC fresh films of the solutions will be discussed briefly.

3.2.1 Determination of salt uptake of LLC fresh films of $LiMn_2O_4$

As it was mentioned in section 3.2, order and uniformity of the structure is important for various application of the mesoporous materials. Hence, the small angle XRD measurement and POM measurement were used to determine maximum salt uptake of the liquid crystalline order and the order of the mesostructure of $LiMn_2O_4$ films. Figure 42 illustrates the small angle XRD patterns, POM images and calculated d-spacing values of the samples with increasing salt:surfactant ratios.

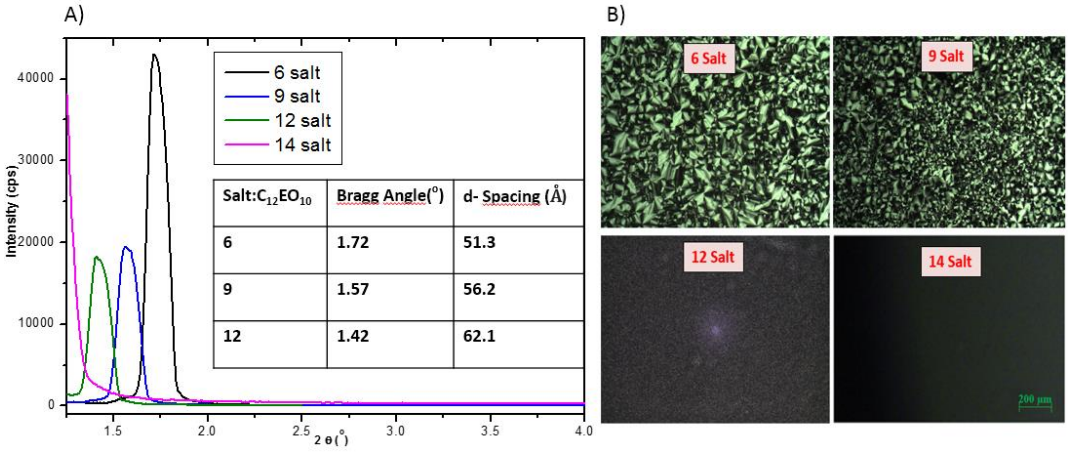

Salt:$C_{12}EO_{10}$	Bragg Angle(°)	d- Spacing (Å)
6	1.72	51.3
9	1.57	56.2
12	1.42	62.1

Figure 42: A) Small angle XRD pattern of the fresh samples and the Bragg angle and the d-spacing values of the samples and B) POM images of the fresh samples prepared using different salt:$C_{12}EO_{10}$ mole ratios (compositions are in the figures).

The diffraction patterns of the fresh samples up to 12 mole ratio display highly intense lines, indicating a long range mesoorder in the samples. Hence, Cu blocks have been inserted in between the source and detector in order to protect the detector of the diffractometer. Bragg's law has been used to calculate d-spacing values of each sample, tabulated in inset of Figure 42(A). The XRD

patterns and the calculated d-spacing values confirmed the increase in the lattice parameters of the fresh samples with ascending amount of salt in the media. The last sample containing 14 salt:surfactant ratio did not diffract since there is no ordered stable mesophase formed due to excess amount of salt loaded to the media. The POM images of the fresh samples shown in Figure 42(B) are also consistent with the XRD data. First 3 samples exhibit hexagonal geometry with fan like texture and the sample containing 14 salt:surfactant ratio display a dark image.

3.2.2 The effect of the solvent during solution preparation

To investigate the effect of solvent, two different solvents have been used. The solutions of the ingredients were prepared in both water and ethanol with CTAB as the charged surfactant. First of all; CTAB was added to the particular solvents and stirred for 2 hours to obtain clear solutions. The mixture prepared with ethanol formed a yellow clear solution after the addition of all other ingredients and used after 12 hours of extra stirring. However, the mixture prepared with H_2O formed yellow precipitate with addition of the $[Mn(H_2O)_4](NO_3)_2$ salt to the media and did not dissolve back even after 1 week of stirring. Yellow precipitate could be seen at the bottom of the vial in Figure 43(A).

It is known that the strong interactions between hydrophobic tail groups of CTAB with ethanol make the formation of CTAB micelle difficult in ethanol. Hence; the CMC (critical micelle concentration) value of CTAB is 0.0009 mol/L in water, while it is up to 0.24 mol/L in ethanol [101]. In other words; there are more micelles in water solution. Since the micelles of the CTAB-$C_{12}E_{10}$ have high

negative charges on them, they might attract positively charged Mn^{2+} cations and could be the reason of formation of yellow $[CTA]_2MnBr_4$ precipitate in the solution prepared with H_2O.

The yellow $[CTA]_2MnBr_4$ precipitate has been removed and dried and its XRD patten is recordes then the patterns of $[CTA]_2MnBr_4$ and CTAB have been analyzed for the comparison, see Figure 42(C).

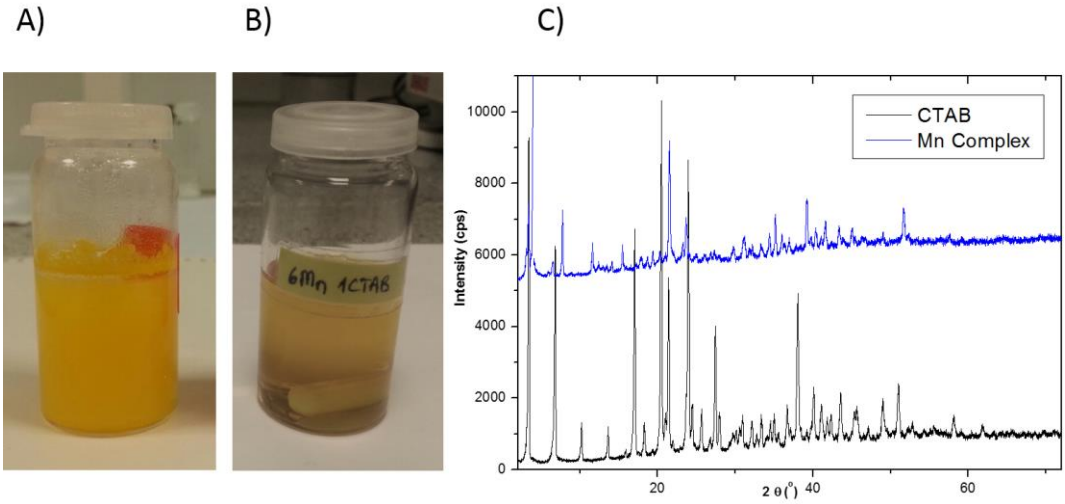

Figure 43: Mixture prepared (A) with H_2O, (B) with ethanol and XRD pattern of CTAB and the yellow precipitate.

Since, a clear solution could not be obtained via using H_2O; ethanol was determined to be used as a solvent for further experimentation.

3.2.3 The effect of HNO_3 during solution preparation

Initially solutions were prepared without addition of acid. However; after around 2 hours the solution started changing color from yellow to brown as shown in Figure 44(A and B). It is known that aqueous solutions of metal ions attract water molecules and form hexaaqua ions, which act as a Lewis acid and donates H^+ to neighboring H_2O molecules. As this typical reaction goes one step further,

forming a new $[Mn(OH)_2(H_2O)_4]$ complex that is a brown solid and gives the brownish color to the solution. The common reaction mechanism includes the following steps;

Step 1: $[Mn(H_2O)_6]^{2+}(aq) + H_2O \rightarrow [Mn(OH)(H_2O)_5]^{+}(aq) + H_3O^{+}$,

Step 2: $[Mn(OH)(H_2O)_5]^{+}(aq) + H_2O \rightarrow [Mn(OH)_2(H_2O)_4](s) + H_3O^{+}$

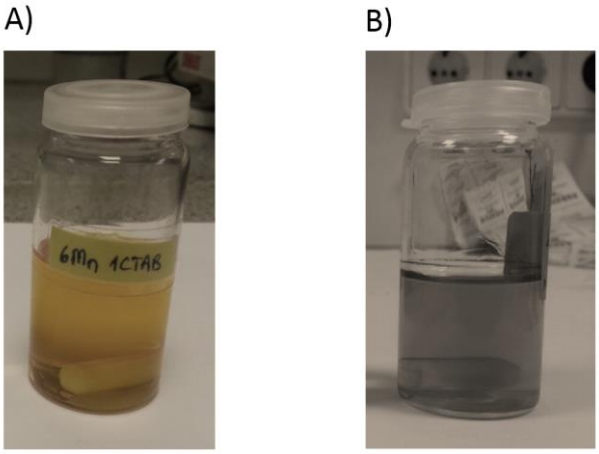

Figure 44: Solutions containing (A) with HNO_3, (B) without HNO_3**.**

Addition of acid might reverse these reactions and hexaaqua ions could be preserved. That's why; HNO_3 is added during the preparation of solutions and amount is set to 1:1 ratio of Mn:HNO_3 by changing the salt amounts.

3.2.4 Optimization of the calcination temperature for $LiMn_2O_4$

In this section, the calcination process will be discussed to investigate the effect on the formation of the side products. As discussed in section 3.1, calcination process is important since all volatile and burnable raw materials (surfactants, metal nitrates, and ethanol) are processed at this step. During calcination, the organic molecules burn in air and form CO_2 and CO gases, metal

nitrates decompose to M_xO_y and NO_x and the target material is obtained by further reactions. Determining the optimum calcination temperature is important since the temperature must be high enough to get rid of all the organic molecules and to complete all the reactions in order to eliminate formation of side products. However, it must also be kept at a certain temperature to preserve the mesoporous structure of the target material without collapsing.

To determine the formation temperature of $LiMn_2O_4$ mesostructure[102], a solution was prepared at 9 salt/surfactant mole ratio and spin coated on a Si wafer. The IR spectra of a heat-treated sample from fresh to 300 ^oC have been collected, Figure 45(A and B). The sample was kept at each temperature for 1 hour. As it is shown in Figure 45(A), up to 160 ^oC; the amounts of H_2O (the broad band around 3404 and 1600 cm^{-1}) and NO_3^- ion (broad bands between 1500 and 1250 cm^{-1} , a sharp one around 1100 cm^{-1} are distinctive ones) decreases accordingly.

The two absorption bands at 518 cm^{-1} and 617 cm^{-1} are identified as spectral feature of cubic nano $LiMn_2O_4$ spinel in the literature [3]. It could be shown that the $LiMn_2O_4$ species start forming around 160 ^oC.

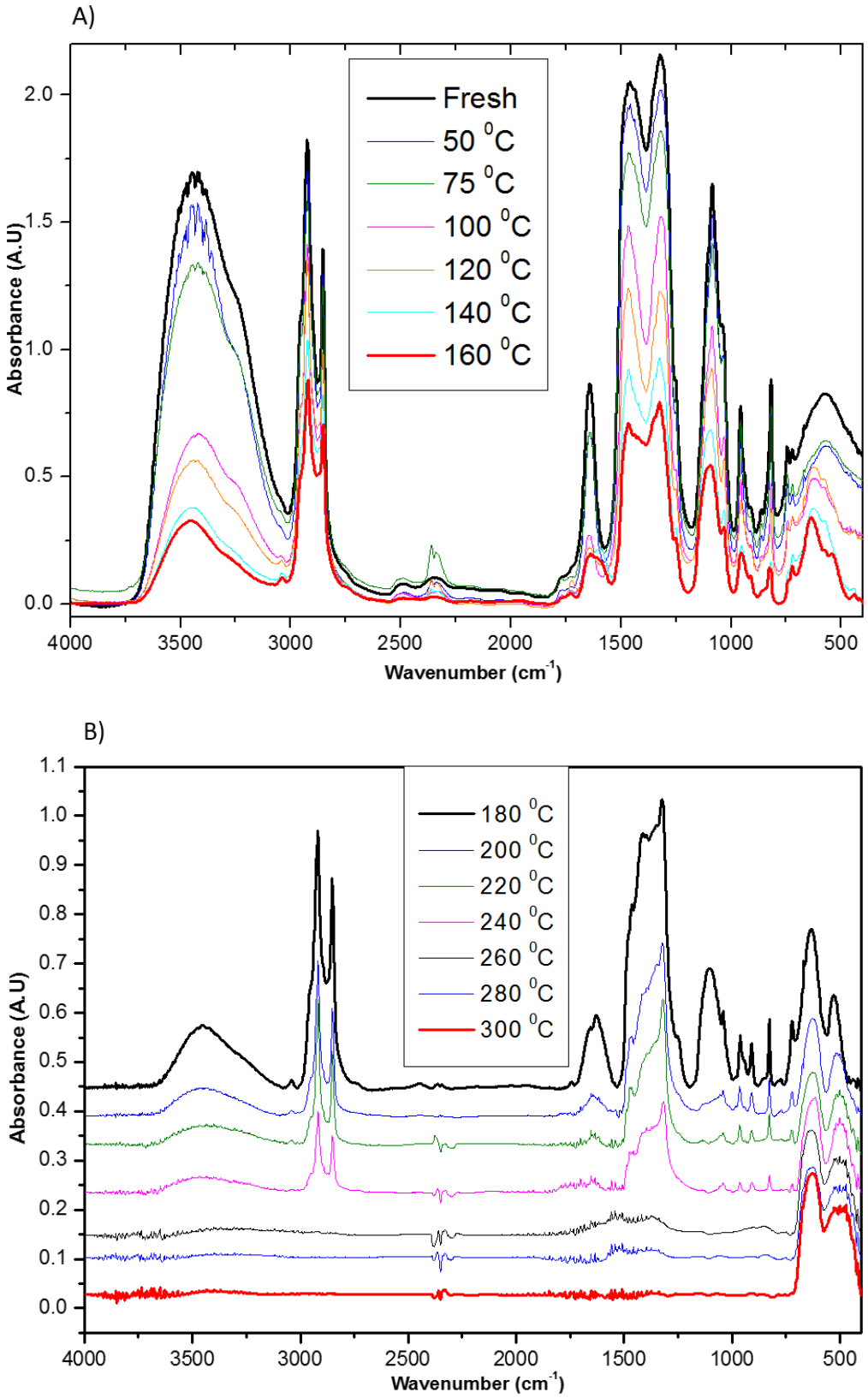

Figure 45: A) IR spectra of the heat-treated sample coated on Si wafer from as prepared to 160 ºC and B) IR spectra of the heat-treated sample coated on Si wafer from 180 ºC to 300 ºC

However; the peaks of nitrate, water, and surfactants completely disappear at around 300 ^{o}C. Therefore; minimum calcination temperature for the synthesis also has been set to 300 ^{o}C for the $LiMn_2O_4$ samples.

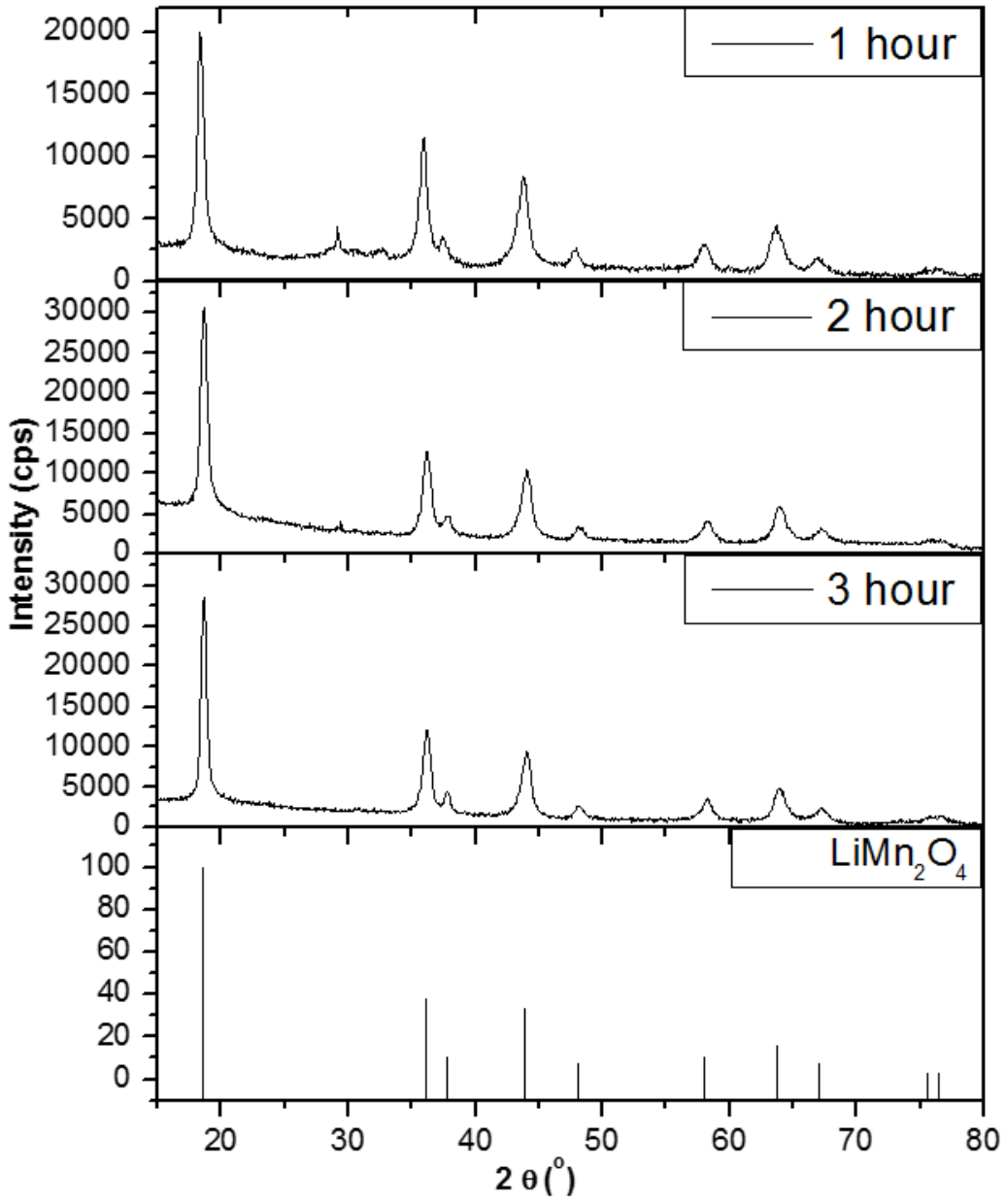

Figure 46: XRD pattern of the powder obtained by using 9 salt composition calcined at 300 ^{o}C for 1, 2 and 3 hours. Assignment of the diffraction pattern of $LiMn_2O_4$ was performed JCPDS 035-0782.

In order to set the duration and verify the temperature, the sample 9 salt ratio have been calcined 3 times at 300 ^{o}C for 1hour and the XRD patterns of the sample have been recorded after each calcination step, Figure 46.

As it is clearly shown in Figure 46; the patterns of the sample, calcined for 1 hour and 2 hours, there appears a line around 29.2^{o}, which does not belong to $LiMn_2O_4$. This peak disappears after 3 hours of calcination. In other words; 3 hours of calcination is necessary for all ingredients to give reaction and form the targeted material. That's why calcination duration has been set to 3 hours for further experimentation.

3.2.5 Br^- effect in solution and on the formation of mesoporous $LiMn_2O_4$

In order to investigate whether Br^- ion has a similar effect like side product formation as it was discussed in section 3.1; we prepared 2 solutions having the same salt ratios but with different ionic surfactants (CTAN or CTAB), see Figure 47.

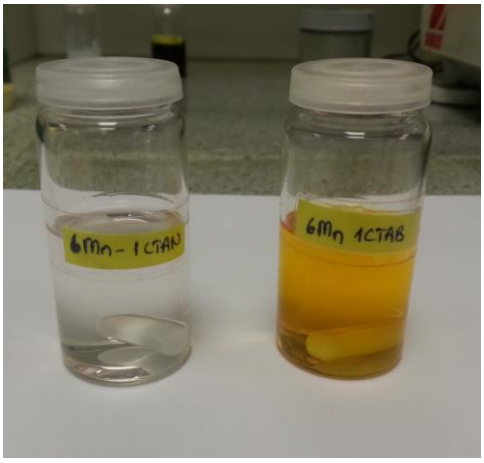

Figure 47: Solutions prepared with CTAN and CTAB.

The solution prepared using CTAN is not yellow due to lack of Br^- ion. Then, both solutions have been calcined at 300 ^oC for 12 hours so that any side product might form large crystals and become visible in the XRD pattern, Figure 48. As it is shown in Figure 48; there is no distinctive difference in between the patterns of the samples and both forms $LiMn_2O_4$.

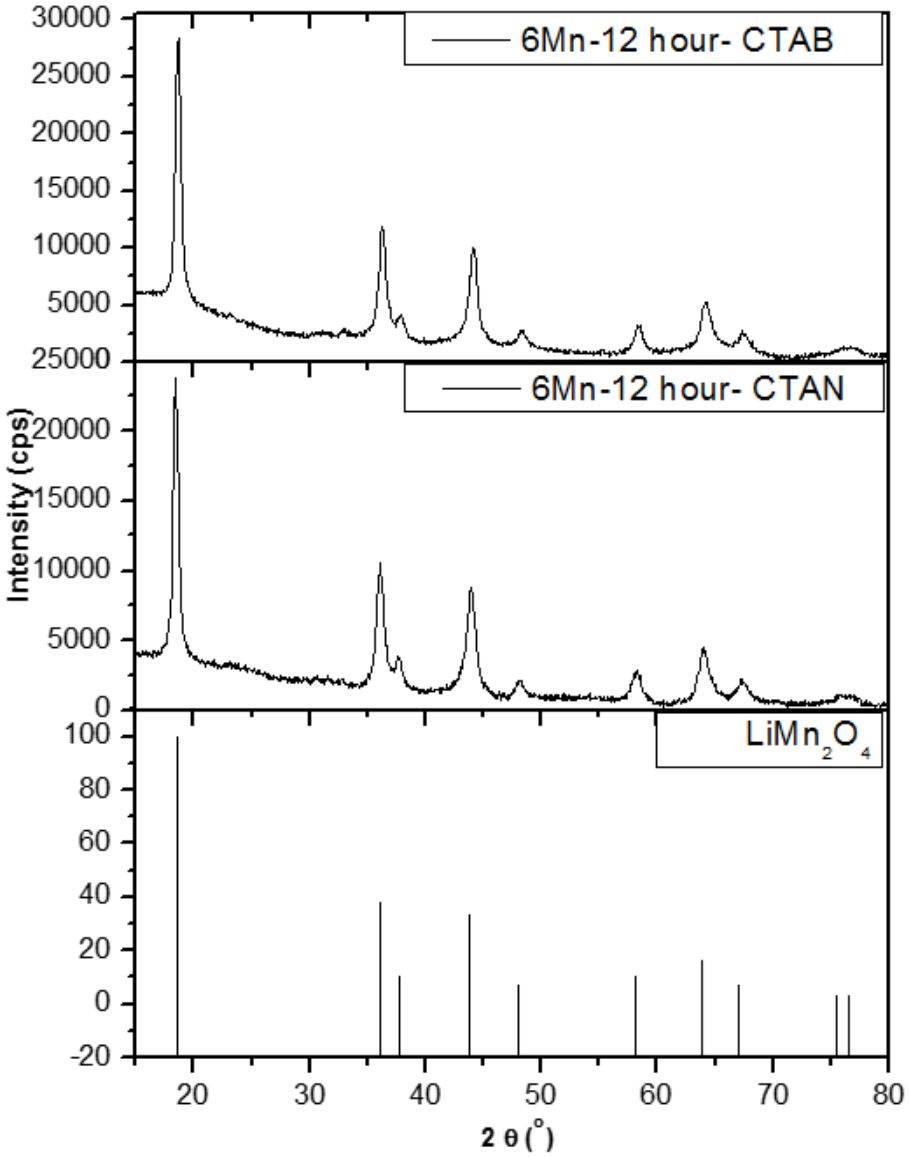

Figure 48: XRD pattern of the samples prepared with CTAB and CTAN.

Raman spectra of the samples also confirmed the outcomes of XRD measurement, Figure 49. The Raman band located around 625 cm^{-1} is attributed

the symmetric Mn–O stretching vibration of MnO_6 groups and there are a group of bands between 200 and 500 cm $^{-1}$ with a weaker intensity. The weak peak located at 382 cm^{-1} has T2g symmetry and the peak at 300 cm^{-1} could be due to the cationic disorder that induces a breakdown of the translation symmetry, respectively[103]. Both samples have a similar Raman spectrum that indicates, none of the samples has any side product.

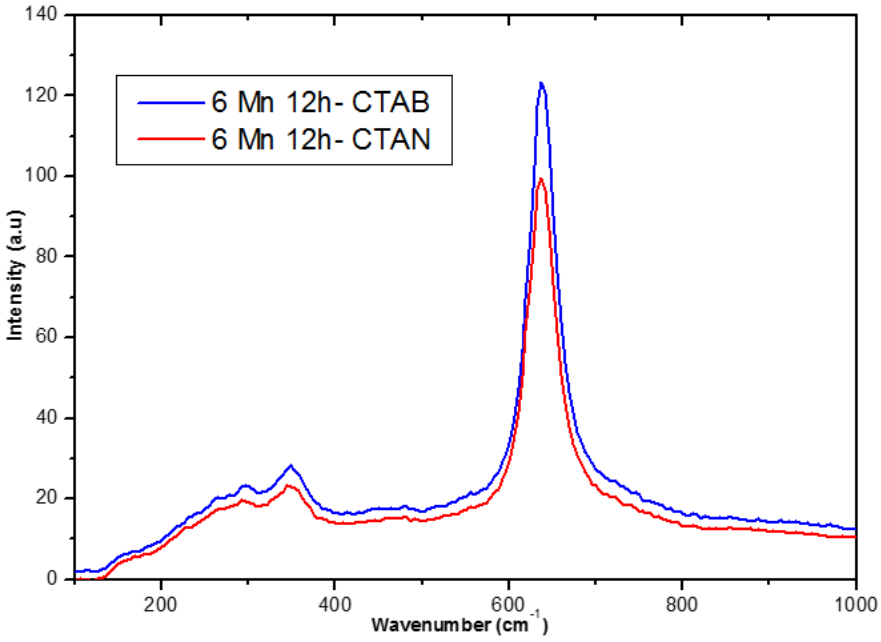

Figure 49: Raman Spectra of the samples prepared with CTAN and CTAB.

As of the last; isotherms and pore size distribution plots have also been examined in Figure 50 and 51, respectively. Both the isotherms and pore size distribution plots show pretty similar results as expected. The specific surface area of the one prepared using CTAN was 55 m^2/g, while the other one prepared using CTAB gave 54 m^2/g with a pore size of 9 and 11 nm, respectively. Therefore; it could be concluded that on the contrary of the synthesis of $LiCoO_2$; CTAB or Br^- ion do not cause any side product formation during the preparation of mesoporous $LiMn_2O_4$

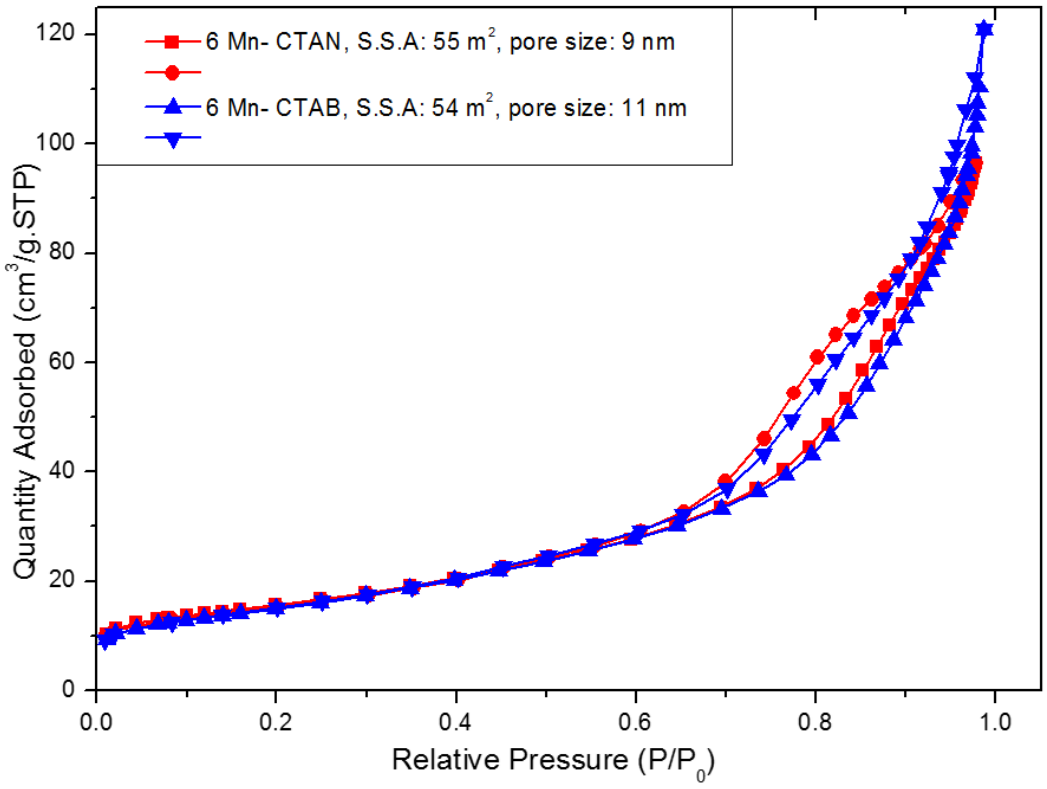

Figure 50: N_2 (77.4 K) sorption isotherms of the samples prepared with CTAB and CTAN and calcined at 300 ^oC for 3-hour.

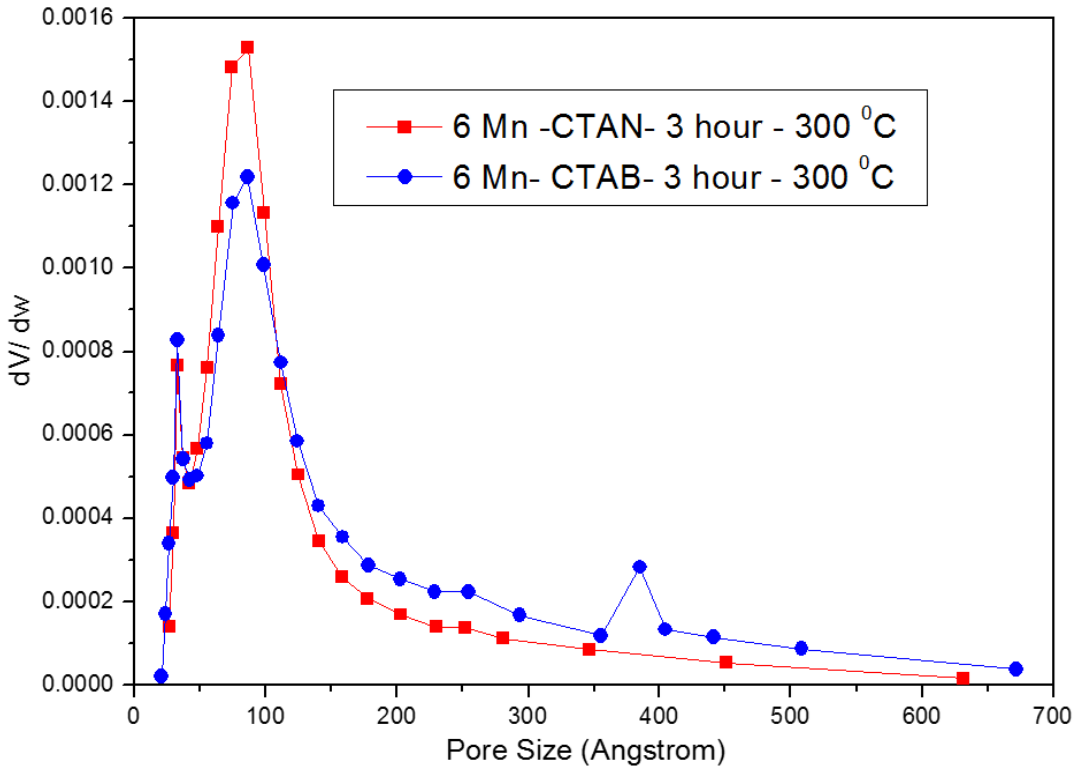

Figure 51: Pore size distribution of the samples prepared with CTAB and CTAN.

3.2.6 Optimization of the pore size and surface area with respect to salt amounts

In order to examine the change in pore size and surface area of the $LiMn_2O_4$ mesostructure with increasing precursors, the high angle XRD, Raman and N_2 sorption data of the samples have been recorded. The salt amounts were set to 4.5, 6, 9, 12, and 14 (Li + Mn):$C_{12}EO_{10}$ mole ratios.

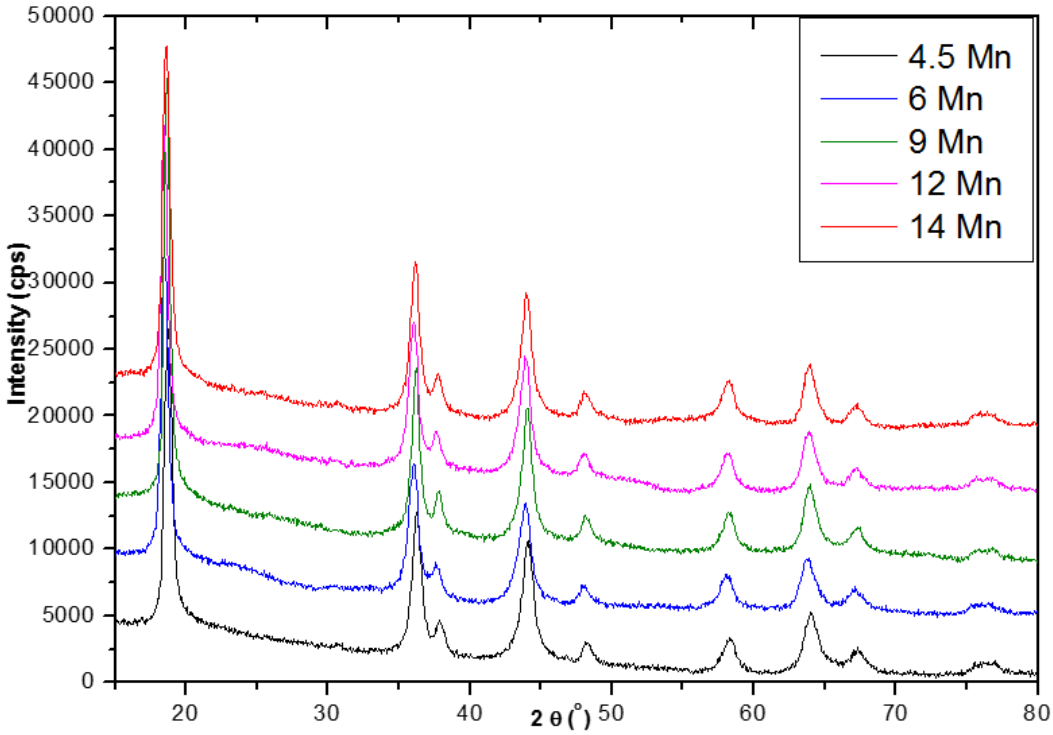

Figure 52: High angle XRD patterns of the samples with increasing salt amounts.

The sample sets were spin coated and calcined at 300 ^oC for 3 hours. There are no visible change in intensities of the lines and no extra lines due to side product formation on the XRD patterns of the samples, see Figure 52. The Raman spectra of the samples in Figure 53 also confirms the outcomes of XRD patterns. As it is shown in Figure 53; with increasing salt amounts, the peaks located at 625 cm^{-1} and the other weaker ones (all belong to $LiMn_2O_4$) slightly broaden around

their location which is attributed to nano-crystalline behavior and there is no sign of side product formation.

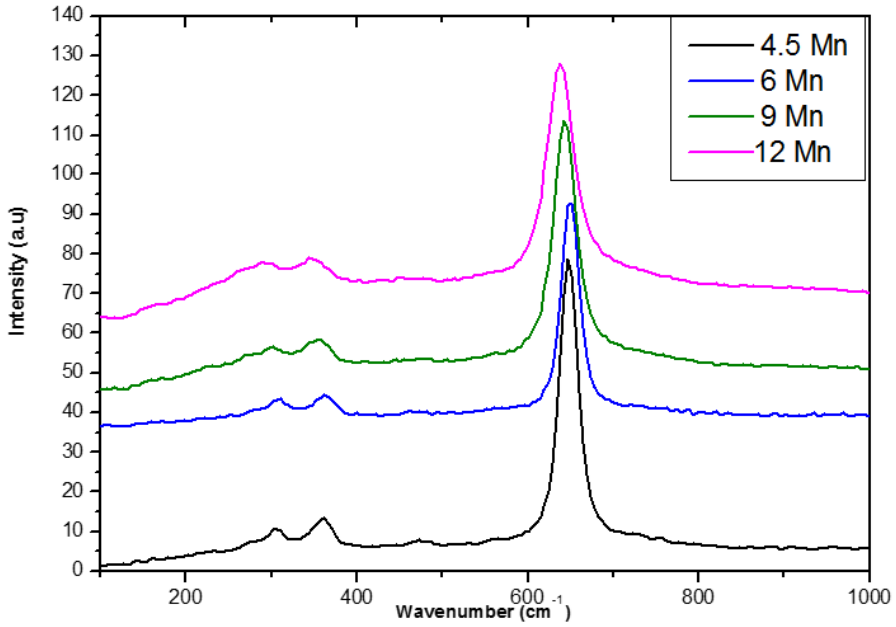

Figure 53: Raman spectra of the samples prepared with increasing salt amounts**.**

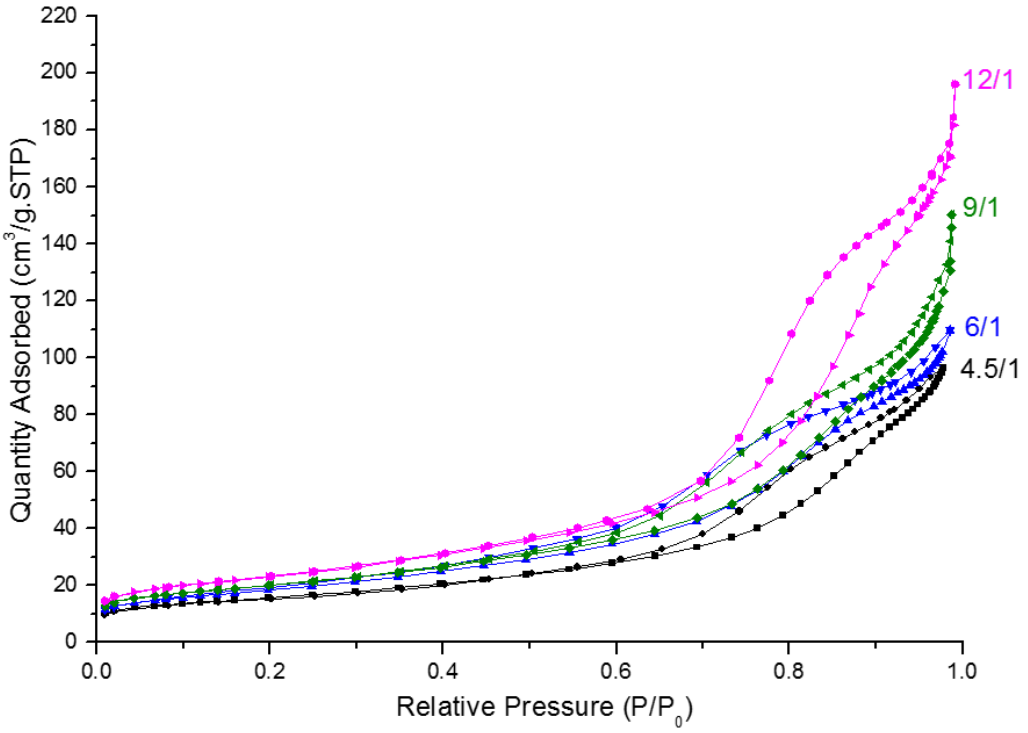

Figure 54: Isotherms of samples with increasing precursors.

Then, N_2 sorption isotherms of the same samples were examined, see Figure 54. The specific surface area of the samples were measured as 55, 66, 71, and 82 m^2/g from the samples obtained from 4.5, 6, 9, and 12 salt ratio, respectively. Since there are no bulk crystals in the samples, it is reasonable to conclude that the surface area of the mesostructures increase with increasing salt amounts.

The pore size distribution of the samples is shown in Figure 55 The BJH desorption pore sizes are 7, 9, 11, and 11 nm, respectively, for the same samples with pore volumes of 0.15, 0.16, 0.24, 0.29 cm^3/g, respectively.

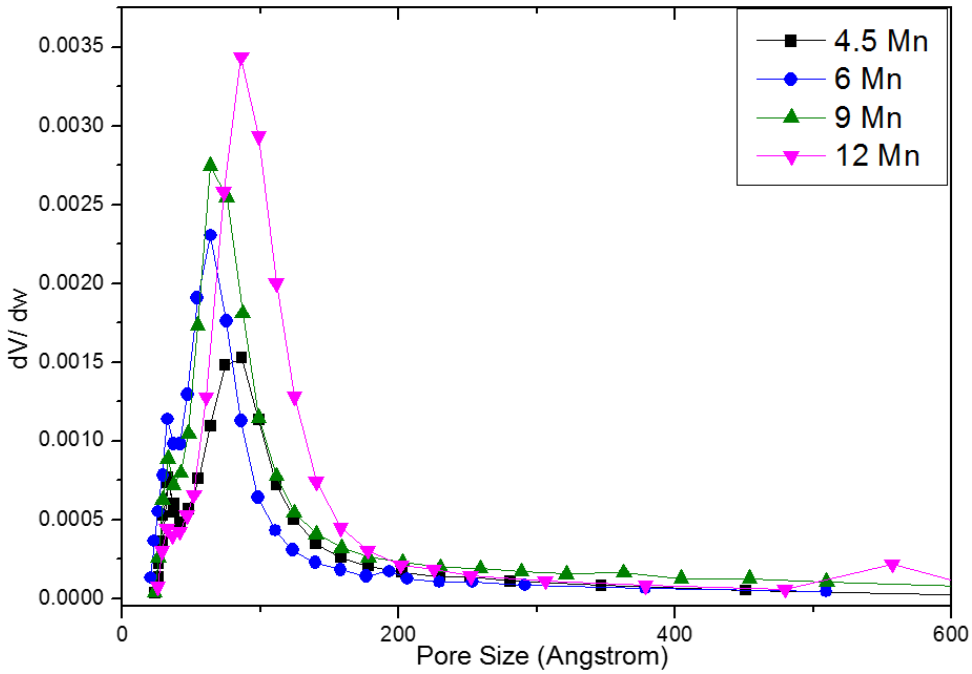

Figure 55: Pore size distribution of the samples with increasing salt amounts

According to Figure 55; the pore size is more uniform at lower salt compositions. With increasing salt amounts, the distribution of pore size is getting broader. It could be due to uncontrollable crystallization of the structure during calcination that might lead to nonuniform pore formation. As a result; it could be concluded that although the fresh films of the higher salt: surfactant compositions don't leach out any crystals, during calcination uncontrollable crystallization

might lead decrease in the uniformity of the pores and formation of the less ordered structures.

The TEM images of the mesoporous thin films of $LiMn_2O_4$ with 2 and 5 nm scale bars are shown in Figures 56 and 57. 15-20 nm sized highly crystalline particulates and 20-25 nm pore size could be identified clearly from these images. A uniform film like structure and pores of the $LiMn_2O_4$ films are shown in Figure 58(A and B). In Figure 59; STEM image of a spongy film of $LiMn_2O_4$ is shown with 200 nm scale bar.

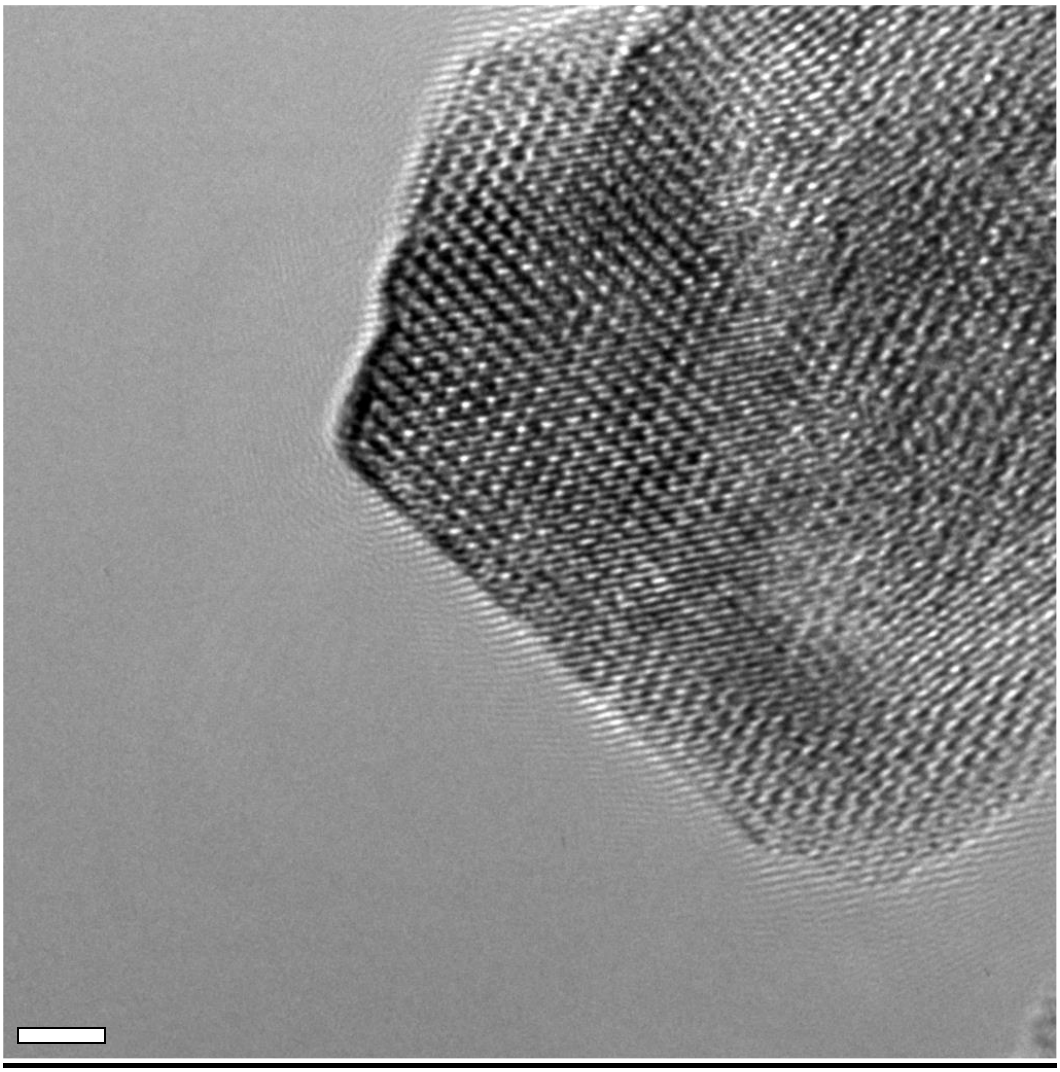

Figure 56: TEM micrograph of $LiMn_2O_4$ with a 2 nm scale bar.

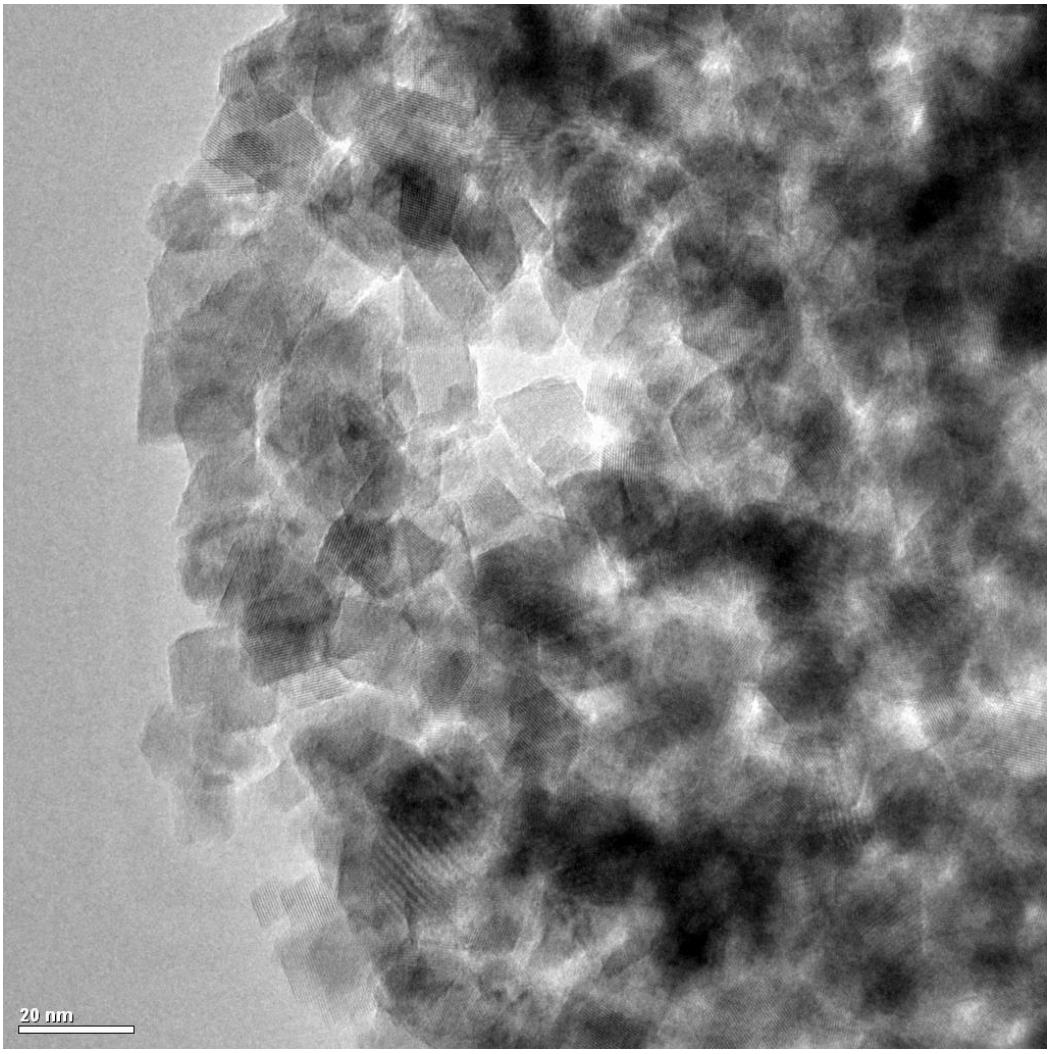

Figure 57: TEM micrograph of $LiMn_2O_4$ with a 20 nm scale bar.

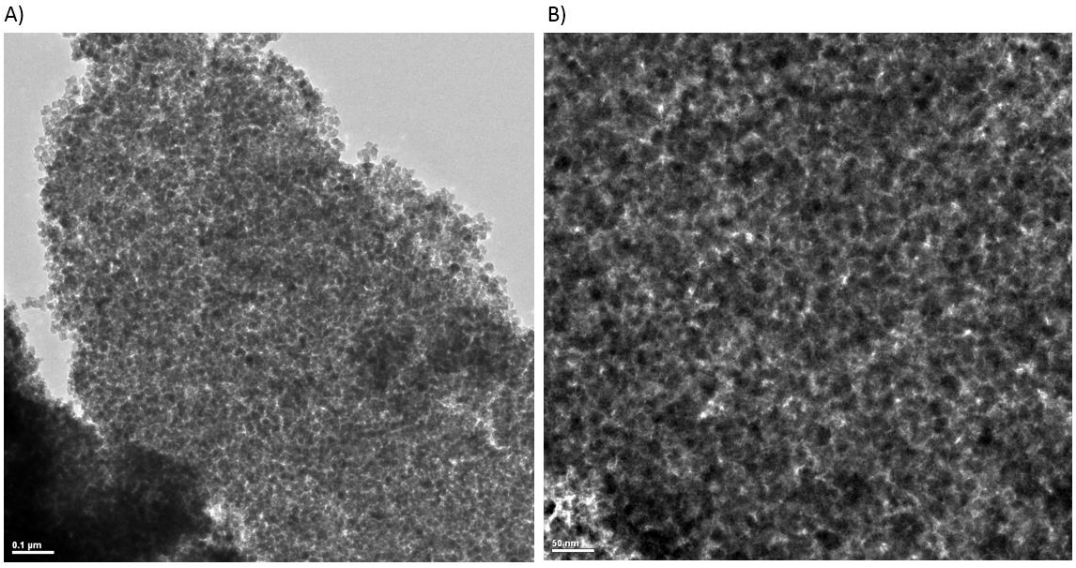

Figure 58: TEM images of $LiMn_2O_4$ with scale bar of (A) 0.1µm and (B) 50 nm.

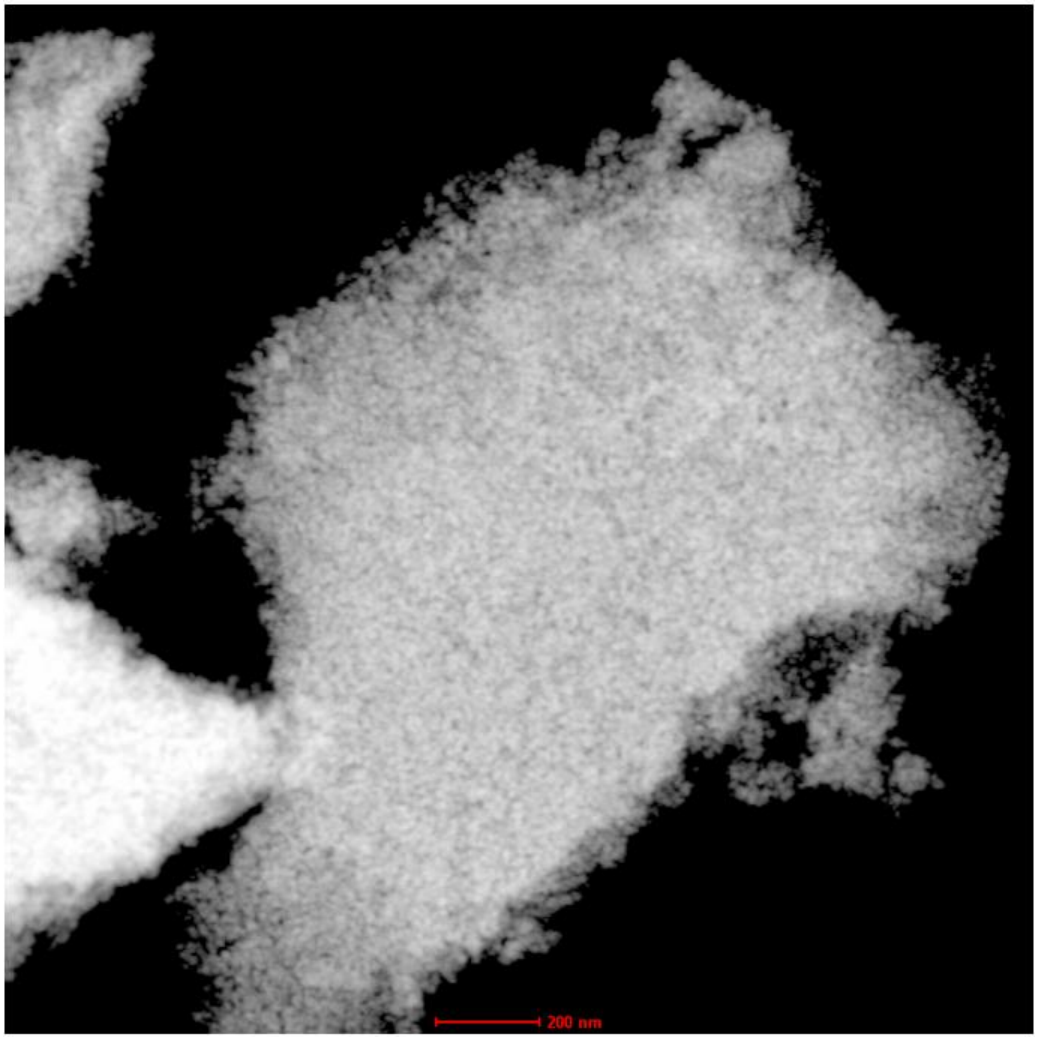

Figure 59: STEM image of $LiMn_2O_4$ with a 200 nm scale bar.

Chapter 4

Conclusion

In this study, it has been demonstrated that the molten salt assisted self-assembly (MASA) method could be used for the synthesis of mesoporous $LiMn_2O_4$ and $LiCoO_2$ materials without a polymerizing agent in the media.

It has been established that the purity, pore size, surface area and crystallinity of the $LiCoO_2$ and $LiMn_2O_4$ mesostructures can be controlled by determining the solvent type, thickness of the LLC film, acid amount, salt uptake, calcination temperature, calcination time and surfactant used for the synthesis. In the case of solution preparation of both $LiCoO_2$ and $LiMn_2O_4$; ethanol is determined to be effective solvent due to low solubility of ingredients and efficiency of the synthesis. HNO_3 has no effect on the synthesis of $LiCoO_2$ but is crucial in the case of $LiMn_2O_4$ to prevent formation of $[Mn(OH)_2(H_2O)_4](s)$ complex during and/or before the assembly process. The method of spin coating gave better results than drop casting to obtain uniform pore size distribution and less side product formation. $LiCoO_2$ samples prepared with CTAB are semicrystalline at lower temperatures, mesostructure is stable up to 550 ^oC but then it undergoes decomposition to Co_3O_4 and Li_2O. Pore size and specific surface area of the samples could be tuned by changing the calcination temperature and duration. In the case of mesoporous $LiCoO_2$; with increasing temperature from 300 to 550 ^oC, the specific surface area changes from 60 to 56 and to 41 m^2/g, respectively. The desorption BJH pore size increased with calcination temperature as 10, 15 and 16

nm and the corresponding pore volumes are 0.24, 0.20 and 0.16 cm^3/g. This reverse trend between pore size and pore volume indicates that while the pores are expanding, the walls of the mesostructure are getting thicker. The positive effect of CTAB to obtain uniform pore size for the synthesis of $LiCoO_2$ have been examined in detail. However; due to role of Br^- ion on formation of side products, CTAN is found to be a more effective charged surfactant in the MASA process. The thin films of calcined samples preserved order of the mesophase during calcination. Mesoporous pure HT- $LiCoO_2$ synthesized with MASA is the first example in the literature since calcination temperature decreased from 900 to 350 ^oC. The mesoporous $LiCoO_2$ films have 65 m^2/g specific surface area and a 15 nm pore size. Moreover; the mesoporous pure $LiMn_2O_4$ could be obtained using both CTAB and CTAN with 82 m^2/g specific surface area and 11 nm pore size.

Bibliography

[1] C. T. Kresge, M. E. Leonowicz, W. J. Roth, J. C. Vartuli, and J. S. Beck, "Ordered mesoporous molecular sieves synthesized by a liquid-crystal template mechanism," *Nature*, vol. 359, no. 6397, pp. 710–712, 1992.

[2] Zhao, Feng, Huo, Melosh, Fredrickson, Chmelka, and Stucky, "Triblock copolymer syntheses of mesoporous silica with periodic 50 to 300 angstrom pores," *Science*, vol. 279, no. 5350, pp. 548–52, 1998.

[3] W. Li and D. Zhao, "An overview of the synthesis of ordered mesoporous materials," *Chem. Commun.*, vol. 49, no. 10, pp. 943–946, 2013.

[4] F. Schüth, "Non-siliceous Mesostructured and Mesoporous Materials †," *Chem. Mater.*, vol. 13, no. 10, pp. 3184–3195, 2001.

[5] M. E. Davis, "Ordered porous materials for emerging applications.," *Nature*, vol. 417, no. 6891, pp. 813–21, 2002.

[6] P. G. Bruce, B. Scrosati, and J.-M. Tarascon, "Nanomaterials for rechargeable lithium batteries.," *Angew. Chem. Int. Ed. Engl.*, vol. 47, no. 16, pp. 2930–46, 2008.

[7] A. Corma, "From Microporous to Mesoporous Molecular Sieve Materials and Their Use in Catalysis.," *Chem. Rev.*, vol. 97, no. 6, pp. 2373–2420, 1997.

[8] A. Taguchi and F. Schüth, "Ordered mesoporous materials in catalysis," *Microporous Mesoporous Mater.*, vol. 77, no. 1, pp. 1–45, 2005.

[9] W. Yue and W. Zhou, "Crystalline mesoporous metal oxide," *Prog. Nat. Sci.*, vol. 18, no. 11, pp. 1329–1338, 2008.

[10] D. Gu and F. Schüth, "Synthesis of non-siliceous mesoporous oxides," *Chem. Soc. Rev.*, vol. 43, no. 1, pp. 313–344, 2014.

[11] H. Yang, D. Zhao, C. T. Kresge, M. E. Leonowicz, W. J. Roth, J. C. Vartuli, J. S. Beck, “Synthesis of replica mesostructures by the nanocasting strategy,” *J. Mater. Chem.*, vol. 15, no. 12, pp. 710–1231, 2005.

[12] B. Smarsly and M. Antonietti, “Block Copolymer Assemblies as Templates for the Generation of Mesoporous Inorganic Materials and Crystalline Films,” *Eur. J. Inorg. Chem.*, vol. 2006, no. 6, pp. 1111–1119, 2006.

[13] M. Tiemann, “Repeated Templating †,” *Chem. Mater.*, vol. 20, no. 3, pp. 961–971, 2008.

[14] G. D. Stucky, P. Yang, D. Zhao, D. I. Margolese, and B. F. Chmelka, “Yang, P. D., Zhao, D. Y., Margolese, D. I., Chmelka, B. F. & Stucky, G. D. Generalized syntheses of large-pore mesoporous metal oxides with semicrystalline frameworks. Nature 396, 152-155,” *Nature*, vol. 396, no. 6707, pp. 152–155, 1998.

[15] S. Che, K. Lund, T. Tatsumi, S. Iijima, S. H. Joo, R. Ryoo, and O. Terasaki, “Direct Observation of 3D Mesoporous Structure by Scanning Electron Microscopy (SEM): SBA-15 Silica and CMK-5 Carbon,” *Angew. Chemie Int. Ed.*, vol. 42, no. 19, pp. 2182–2185, 2003.

[16] R. Ryoo, S. H. Joo, and S. Jun, “Synthesis of Highly Ordered Carbon Molecular Sieves via Template-Mediated Structural Transformation,” *J. Phys. Chem. B*, vol. 103, no. 37, pp. 7743–7746, 1999.

[17] M. Kruk, M. Jaroniec, R. Ryoo, and S. H. Joo, “Characterization of Ordered Mesoporous Carbons Synthesized Using MCM-48 Silicas as Templates,” *J. Phys. Chem. B*, vol. 104, no. 33, pp. 7960–7968, 2000.

[18] K. Zhu, B. Yue, W. Zhou, and H. He, “Preparation of three-dimensional chromium oxide porous single crystals templated by SBA-15,” *Chem. Commun.*, vol. 0, no. 1, pp. 98–99, 2003.

[19] D. Grosso, C. Boissière, B. Smarsly, T. Brezesinski, N. Pinna, P. A. Albouy, H. Amenitsch, M. Antonietti, and C. Sanchez, “Periodically ordered nanoscale islands and mesoporous films composed of nanocrystalline multimetallic oxides,” *Nat. Mater.*, vol. 3, no. 11, pp. 787–792, 2004.

[20] Yu Ren, Zhen Ma, Peter G. Bruce, “Ordered Mesoporous Metal Oxides :

Synthesis and Applications," *Chem. Soc. Rev.*, vol. 41, no. August, pp. 4909–4927, 2012.

[21] R. A. Caruso, "Nanocasting and Nanocoating," Springer Berlin Heidelberg, 2003, pp. 91–118.

[22] G. J. A. A. Soler-Illia and O. Azzaroni, "Multifunctional hybrids by combining ordered mesoporous materials and macromolecular building blocks," *Chem. Soc. Rev.*, vol. 40, no. 2, p. 1107, 2011.

[23] C. Sanchez, L. Rozes, F. Ribot, C. Laberty-Robert, D. Grosso, C. Sassoye, C. Boissiere, and L. Nicole, "'Chimie douce': A land of opportunities for the designed construction of functional inorganic and hybrid organic-inorganic nanomaterials," *Comptes Rendus Chim.*, vol. 13, no. 1–2, pp. 3–39, 2010.

[24] N. D. Petkovich, A. Stein, R. A. Caruso, "Controlling macro- and mesostructures with hierarchical porosity through combined hard and soft templating," *Chem. Soc. Rev.*, vol. 42, no. 9, pp. 3721–3739, 2013.

[25] Y. Yamauchi and K. Kuroda, "Rational Design of Mesoporous Metals and Related Nanomaterials by a Soft-Template Approach," *Chem. – An Asian J.*, vol. 3, no. 4, pp. 664–676, 2008.

[26] W.-C. Yoo and J.-K. Lee, "Field-Dependent Growth Patterns of Metals Electroplated in Nanoporous Alumina Membranes," *Adv. Mater.*, vol. 16, no. 13, pp. 1097–1101, 2004.

[27] C. M. Zelenski and P. K. Dorhout, "Template Synthesis of Near-Monodisperse ^{1} Microscale Nanofibers and Nanotubules of MoS_2," *J. Am. Chem. Soc.*, vol. 120, no. 4, pp. 734–742, 1998.

[28] P. Banerjee, I. Perez, L. Henn-Lecordier, S. B. Lee, and G. W. Rubloff, "Nanotubular metal–insulator–metal capacitor arrays for energy storage," *Nat. Nanotechnol.*, vol. 4, no. 5, pp. 292–296, 2009.

[29] H. J. Shin, R. Ryoo, Z. Liu, and O. Terasaki, "Template Synthesis of Asymmetrically Mesostructured Platinum Networks," *J. Am. Chem. Soc.*, vol. 123, no. 6, pp. 1246–1247, 2001.

[30] S. Jun, S. H. Joo, R. Ryoo, M. Kruk, M. Jaroniec, Z. Liu, T. Ohsuna, and O. Terasaki, “Synthesis of New, Nanoporous Carbon with Hexagonally Ordered Mesostructure,” *J. Am. Chem. Soc.*, vol. 122, no. 43, pp. 10712–10713, 2000.

[31] B. Yue, H. Tang, Z. Kong, K. Zhu, C. Dickinson, W. Zhou, and H. He, “Preparation and characterization of three-dimensional mesoporous crystals of tungsten oxide,” *Chem. Phys. Lett.*, vol. 407, no. 1, pp. 83–86, 2005.

[32] A. Rumplecker, F. Kleitz, E.-L. Salabas, and F. Schüth, “Hard Templating Pathways for the Synthesis of Nanostructured Porous Co_3O_4,” *Chem. Mater.*, vol. 19, no. 3, pp. 485–496, 2007.

[33] Y. Ren, A. R. Armstrong, F. Jiao, and P. G. Bruce, “Influence of Size on the Rate of Mesoporous Electrodes for Lithium Batteries,” *J. Am. Chem. Soc.*, vol. 132, no. 3, pp. 996–1004, 2010.

[34] E. Ramasamy and J. Lee, “Ordered Mesoporous SnO_2 −Based Photoanodes for High-Performance Dye-Sensitized Solar Cells,” *J. Phys. Chem. C*, vol. 114, no. 50, pp. 22032–22037, 2010.

[35] G. Wang, H. Liu, J. Horvat, B. Wang, S. Qiao, J. Park, and H. Ahn, “Highly Ordered Mesoporous Cobalt Oxide Nanostructures: Synthesis, Characterisation, Magnetic Properties, and Applications for Electrochemical Energy Devices,” *Chem. - A Eur. J.*, vol. 16, no. 36, pp. 11020–11027, 2010.

[36] H. Liu, G. Wang, J. Liu, S. Qiao, and H. Ahn, “Highly ordered mesoporous NiO anode material for lithium ion batteries with an excellent electrochemical performance,” *J. Mater. Chem.*, vol. 21, no. 9, p. 3046, 2011.

[37] F. Jiao, J.-C. Jumas, M. Womes, A. V. Chadwick, A. Harrison, and P. G. Bruce, “Synthesis of Ordered Mesoporous Fe_3O_4 and γ-Fe_2O_3 with Crystalline Walls Using Post-Template Reduction/Oxidation,” *J. Am. Chem. Soc.*, vol. 128, no. 39, pp. 12905–12909, 2006.

[38] F. Jiao, A. Harrison, A. H. Hill, and P. G. Bruce, “Mesoporous Mn2O3 and Mn3O4 with Crystalline Walls,” *Adv. Mater.*, vol. 19, no. 22, pp. 4063–4066, Nov. 2007.

[39] H. Tüysüz, Y. Liu, C. Weidenthaler, and F. Schüth, “Pseudomorphic Transformation of Highly Ordered Mesoporous Co 3 O 4 to CoO via Reduction with Glycerol,” *J. Am. Chem. Soc.*, vol. 130, no. 43, pp. 14108–14110, 2008.

[40] J. Fan, S. W. Boettcher, C.-K. Tsung, Q. Shi, M. Schierhorn, and G. D. Stucky, “Field-Directed and Confined Molecular Assembly of Mesostructured Materials: Basic Principles and New Opportunities †,” *Chem. Mater.*, vol. 20, no. 3, pp. 909–921, 2008.

[41] Q. Huo, D. I. Margolese, U. Ciesla, D. G. Demuth, P. Feng, T. E. Gier, P. Sieger, A. Firouzi, and B. F. Chmelka, “Organization of Organic Molecules with Inorganic Molecular Species into Nanocomposite Biphase Arrays,” *Chem. Mater.*, vol. 6, no. 8, pp. 1176–1191, 1994.

[42] D. M. Antonelli and J. Y. Ying, “Synthesis of Hexagonally Packed Mesoporous TiO2 by a Modified Sol–Gel Method,” *Angew. Chemie Int. Ed. English*, vol. 34, no. 18, pp. 2014–2017, 1995.

[43] D. M. Antonelli, A. Nakahira, and J. Y. Ying, “Ligand-Assisted Liquid Crystal Templating in Mesoporous Niobium Oxide Molecular Sieves,” *Inorg. Chem.*, vol. 35, no. 11, pp. 3126–3136, 1996.

[44] M. S. Wong, D. M. Antonelli, and J. Y. Ying, “Synthesis and characterization of phosphated mesoporous zirconium oxide,” *Nanostructured Mater.*, vol. 9, no. 1–8, pp. 165–168, 1997.

[45] P. Liu, I. L. Moudrakovski, J. Liu, and A. Sayari, “Mesostructured Vanadium Oxide Containing Dodecylamine ⊥,” *Chem. Mater.*, vol. 9, no. 11, pp. 2513–2520, 1997.

[46] D. M. Antonelli, “Synthesis and Mechanistic Studies of Sulfated Meso- and Microporous Zirconias with Chelating Carboxylate Surfactants,” *Adv. Mater.*, vol. 11, no. 6, pp. 487–492, 1999.

[47] D. M. Antonelli, “Synthesis of macro-mesoporous niobium oxide molecular sieves by a ligand-assisted vesicle templating strategy,” *Microporous Mesoporous Mater.*, vol. 33, no. 1, pp. 209–214, 1999.

[48] P. Yang, D. Zhao, D. I. Margolese, B. F. Chmelka, and G. D. Stucky, “Block Copolymer Templating Syntheses of Mesoporous Metal Oxides

with Large Ordering Lengths and Semicrystalline Framework," *Chem. Mater.*, vol. 11, no. 10, pp. 2813–2826, 1999.

[49] C. J. Brinker, Y. Lu, A. Sellinger, and H. Fan, "Evaporation-Induced Self-Assembly: Nanostructures Made Easy." *Adv. Mater.*, vol. 11, no. 7, pp. 579–585, 1999.

[50] G. J. de A. A. Soler-Illia, C. Sanchez, B. Lebeau, and J. Patarin, "Chemical Strategies To Design Textured Materials: from Microporous and Mesoporous Oxides to Nanonetworks and Hierarchical Structures," *Chem. Rev.*, vol. 102, no. 11, pp. 4093–4138, 2002.

[51] D. Grosso, G. J. de A.A. Soler-Illia, E. L. Crepaldi, B. Charleux, and C. Sanchez, "Nanocrystalline Transition-Metal Oxide Spheres with Controlled Multi-Scale Porosity," *Adv. Funct. Mater.*, vol. 13, no. 1, pp. 37–42, 2003.

[52] F. Jiao, A. Harrison, J.-C. Jumas, A. V. Chadwick, W. Kockelmann, and P. G. Bruce, "Ordered Mesoporous Fe_2O_3 with Crystalline Walls," *J. Am. Chem. Soc.*, vol. 128, no. 16, pp. 5468–5474, 2006.

[53] L. Ye, S. Xie, B. Yue, L. Qian, S. Feng, S. C. Tsang, Y. Li, and H. He, "Crystalline three-dimensional cubic mesoporous niobium oxide," *CrystEngComm*, vol. 12, no. 2, pp. 344–347, 2010.

[54] H. Gao, R. Zhu, X. Yang, S. Mao, S. Zhao, J. Yu, and Y. Du, "Properties of polyethylene glycol (23) lauryl ether with cetyltrimethylammonium bromide in mixed aqueous solutions studied by self-diffusion coefficient NMR," *J. Colloid Interface Sci.*, vol. 273, no. 2, pp. 626–631, 2004.

[55] T. Sato, D. P. Acharya, M. Kaneko, K. Aramaki, Y. Singh, M. Ishitobi, and H. Kunieda, "Oil-Induced Structural Change of Wormlike Micelles in Sugar Surfactant Systems," *J. Dispers. Sci. Technol.*, vol. 27, no. 5, pp. 611–616, 2006.

[56] H. Kunieda, G. Umizu, and K. Aramaki, "Effect of Mixing Oils on the Hexagonal Liquid Crystalline Structures," *J. Phys. Chem. B*, vol. 104, no. 9, pp. 2005–2011, 2000.

[57] A. F. Demirörs, B. E. Eser, and Ö. Dag, "Liquid Crystalline Mesophases of Pluronics (L64, P65, and P123) and Transition Metal Nitrate Salts ($[M(H_2O)_6](NO_3)_2$)," *Langmuir*, vol. 21, no. 9, pp. 4156–4162, 2005.

[58] C. Albayrak, G. Gülten, and Ö. Dag, “Phase Separation in Liquid Crystalline Mesophases of [Co(H 2 O) 6]X 2 :P65 Systems (X = NO 3 - , Cl - , or ClO 4 -),” *Langmuir*, vol. 23, no. 2, pp. 855–860, 2007.

[59] N. M. Selivanova, V. S. Lobkov, V. P. Barabanov, K. M. Salikhov, W. Haase, and Y. G. Galyametdinov, “Lyotropic metal mesogens based on a nonionic surfactant and lanthanide nitrates,” *Dokl. Chem.*, vol. 401, no. 1–3, pp. 51–54, 2005.

[60] Ö. Dag, A. Verma, G. A. Ozin, and C. T. Kresge, “Salted mesostructures: salt-liquid crystal templating of lithium triflate-oligo(ethylene oxide) surfactant-mesoporous silica nanocomposite films and monoliths,” *J. Mater. Chem.*, vol. 9, no. 7, pp. 1475–1482, 1999.

[61] Ö. Çelik and Ö. Dag, “A New Lyotropic Liquid Crystalline System: Oligo(ethylene oxide) Surfactants with [M(H2O)n]Xm Transition Metal Complexes,” *Angew. Chemie*, vol. 113, no. 20, pp. 3915–3919, 2001.

[62] Ö. Dag, S. Alayoğlu, C. Tura, and Ö. Çelik, “Lyotropic Liquid-Crystalline Phase of Oligo(ethylene oxide) Surfactant/Transition Metal Salt and the Synthesis of Mesostructured Cadmium Sulfide,” *Chem. Mater.*, vol. 15, no. 14, pp. 2711–2717, 2003.

[63] Ö. Dag, S. Alayoğlu, and İ. Uysal, “Effects of Ions on the Liquid Crystalline Mesophase of Transition-Metal Salt:Surfactant (C $_n$ EO $_m$),” *J. Phys. Chem. B*, vol. 108, no. 24, pp. 8439–8446, 2004.

[64] V. Percec, D. Tomazos, J. Heck, H. Blackwell, and G. Ungar, “Self-assembly of taper-shaped monoesters of oligo(ethylene oxide) with 3,4,5-tris(n-dodecan-1-yloxy)benzoic acid and of their polymethacrylates into tubular supramolecular architectures displaying a columnar hexagonal mesophase,” *J. Chem. Soc. Perkin Trans. 2*, vol. 0, no. 1, p. 31, 1994.

[65] M. Lee and B.-K. Cho, “Induction of Thermotropic Liquid Crystalline Phases in Coil−Rod−Coil Triblock Molecules Containing Poly(propylene oxide) through Complexation with LiCF 3 SO 3,” *Chem. Mater.*, vol. 10, no. 7, pp. 1894–1903, Jul. 1998.

[66] T. Ohtake, M. Ogasawara, K. Ito-Akita, N. Nishina, S. Ujiie, H. Ohno, and T. Kato, “Liquid-Crystalline Complexes of Mesogenic Dimers Containing Oxyethylene Moieties with LiCF 3 SO 3 : Self-Organized Ion Conductive Materials,” *Chem. Mater.*, vol. 12, no. 3, pp. 782–789, Mar. 2000.

[67] B. Donnio, “Lyotropic metallomesogens,” *Curr. Opin. Colloid Interface Sci.*, vol. 7, no. 5, pp. 371–394, 2002.

[68] C. Albayrak, A. M. Soylu, and Ö. Dag, “The role of charged surfactants in the thermal and structural properties of lyotropic liquid crystalline mesophases of [Zn(H2O)6](NO3)2–CnEOm–H2O,” *J. Colloid Interface Sci.*, vol. 341, no. 1, pp. 109–116, 2010.

[69] C. Albayrak, A. M. Soylu, and O. Dag, “Lyotropic Liquid-Crystalline Mesophases Systems,” *Langmuir*, vol. 24, no. 19, pp. 10592–10595, 2008.

[70] C. Karakaya, Y. Türker, C. Albayrak, and Ö. Dag, “Assembly of Molten Transition Metal SaltÀSurfactant in a Confined Space for the Synthesis of Mesoporous Metal Oxide-Rich Metal OxideÀSilica Thin Films,” | *Chem. Mater*, vol. 23, pp. 3062–3071, 2011.

[71] Y. Türker, C. Karakaya, and Ö. Dag, “Fabrication of Mesoporous Metal Chalcogenide Nanoflake Silica Thin Films and Spongy Mesoporous CdS and CdSe,” *Chem. - A Eur. J.*, vol. 18, no. 12, pp. 3695–3705, 2012.

[72] C. Karakaya, Y. Türker, and Ö. Dag, “Molten-Salt-Assisted Self-Assembly (MASA)-Synthesis of Mesoporous Metal Titanate-Titania, Metal Sulfide-Titania, and Metal Selenide-Titania Thin Films,” *Adv. Funct. Mater.*, vol. 23, no. 32, pp. 4002–4010, 2013.

[73] S. H. Tolbert, “Mesoporous silica: Holey quasicrystals,” *Nat. Publ. Gr.*, vol. 11, 2012.

[74] P. Kalyani, R. Jagannathan, S. Gopukumar, and C.-H. Lu, “Luminescence in some lithiated transition metal oxide cathodes,” *J. Power Sources*, vol. 109, no. 2, pp. 301–307, 2002.

[75] T. Maiyalagan, K. A. Jarvis, S. Therese, P. J. Ferreira, and A. Manthiram, “Spinel-type lithium cobalt oxide as a bifunctional electrocatalyst for the oxygen evolution and oxygen reduction reactions,” *Nat. Commun.*, vol. 5, May 2014.

[76] Y. Xu, L. Ding, T. Zhong, X. Han, L. Jiao, H. Yuan, and Y. Wang, “Novel application of $LiCoO_2$ as a high-performance candidate material for supercapacitor,” *J. Energy Chem.*, vol. 24, no. 2, pp. 193–198, 2015.

[77] S. Yamaguchi, N. Nakamura, H. Yamamoto, H. Inokawa, T. Ichikawa, Y. Kojima, and H. Miyaoka, “Thermochemical Water-splitting Reaction by Alkali Metal-Cobalt Oxide,” *J. Japan Inst. Energy*, vol. 92, no. 9, pp. 909–912, 2013.

[78] S. Chen, Z. Chen, and C. Cao, “Mesoporous Spinel $LiMn_2O_4$ Cathode Material by a Soft-templating Route,” *Electrochim. Acta*, vol. 199, pp. 51–58, 2016.

[79] Y. Wang, J. Guo, T. Wang, J. Shao, D. Wang, and Y.-W. Yang, “Mesoporous Transition Metal Oxides for Supercapacitors,” *Nanomaterials*, vol. 5, no. 4, pp. 1667–1689, 2015.

[80] J. Rosen, G. S. Hutchings, and F. Jiao, “Ordered Mesoporous Cobalt Oxide as Highly Efficient Oxygen Evolution Catalyst,” *J. Am. Chem. Soc.*, vol. 135, no. 11, pp. 4516–4521, 2013.

[81] C. W. Cady, G. Gardner, Z. O. Maron, M. Retuerto, Y. B. Go, S. Segan, M. Greenblatt, and G. C. Dismukes, “Tuning the Electrocatalytic Water Oxidation Properties of AB_2O_4 Spinel Nanocrystals: A (Li, Mg, Zn) and B (Mn, Co) Site Variants of $LiMn_2O_4$,” *ACS Catalysis.*, vol. 5, no. 6, pp. 3403–3410, 2015.

[82] Z. Wu, Y. Zhu, X. Ji, and C. E. Banks, “Transition Metal Oxides as Supercapacitor Materials,” Springer International Publishing, pp. 317–344, 2016.

[83] B. Han, D. Qian, M. Risch, H. Chen, M. Chi, Y. Shirley Meng, and Y. Shao-Horn, “Role of LiCoO2 Surface Terminations in Oxygen Reduction and Evolution Kinetics.” *J. Phys. Chem. Lett*, vol. 107, no. 24, pp. 5806–5811, 2015.

[84] V. Subramanian, C. L. Chen, H. S. Chou, G. T. K. Fey, “Microwave-assisted solid-state synthesis of $LiCoO_2$ and its electrochemical properties as a cathode material for lithium batteries,” *J. Mater. Chem.*, vol. 11, no. 12, pp. 3348–3353, 2001.

[85] P. Ghosh, S. Mahanty, M. W. Raja, R. N. Basu, and H. S. Maiti, “Structure and optical absorption of combustion-synthesized nanocrystalline $LiCoO_2$,” *J. Mater. Res.*, vol. 22, no. 5, pp. 1162–1167, 2007.

[86] H. Xia, L. Lu, Y. S. Meng, and G. Ceder, “Phase Transitions and High-Voltage Electrochemical Behavior of $LiCoO_2$ Thin Films Grown by Pulsed Laser Deposition,” *J. Electrochem. Soc.*, vol. 154, no. 4, p. A337–A342, 2007.

[87] F. Jiao, K. M. Shaju, and P. G. Bruce, “Synthesis of Nanowire and Mesoporous Low-Temperature $LiCoO_2$ by a Post-Templating Reaction,” *Angew. Chemie Int. Ed.*, vol. 44, no. 40, pp. 6550–6553, 2005.

[88] E. Hosono, T. Kudo, I. Honma, H. Matsuda, and H. Zhou, “Synthesis of Single Crystalline Spinel $LiMn_2O_4$ Nanowires for a Lithium Ion Battery with High Power Density,” *Nano Lett.*, vol. 9, no. 3, pp. 1045–1051, 2009.

[89] J. He, Y. Chen, P. Li, F. Fu, J. Liu, Z. Wang, “Facile fabrication of RGO wrapped $LiMn_2O_4$ nanorods as a cathode with enhanced specific capacity,” *RSC Adv.*, vol. 5, no. 97, pp. 80063–80068, 2015.

[90] A. Manthiram, “Materials Challenges and Opportunities of Lithium Ion Batteries,” *J. Phys. Chem. Lett.*, vol. 2, no. 3, pp. 176–184, 2011.

[91] J. Luo, Y. Wang, H. Xiong, and Y. Xia, “Ordered Mesoporous Spinel $LiMn_2O_4$ by a Soft-Chemical Process as a Cathode Material for Lithium-Ion Batteries,” *Chem. Mater.*, vol. 19, no. 19, pp. 4791–4795, 2007.

[92] F. Jiao, J. Bao, A. H. Hill, and P. G. Bruce, “Synthesis of Ordered Mesoporous Li-Mn-O Spinel as a Positive Electrode for Rechargeable Lithium Batteries,” *Angew. Chemie*, vol. 120, no. 50, pp. 9857–9862, 2008.

[93] B.-M. Hwang, S.-J. Kim, Y.-W. Lee, B. Han, S.-B. Kim, W.-S. Kim, and K.-W. Park, “Mesoporous Spinel $LiMn_2O_4$ Nanomaterial as a Cathode for High-Performance Lithium Ion Batteries,” *Int. J. Electrochem. Sci*, vol. 8, pp. 9449–9458, 2013.

[94] M. L. T. Liveri, R. Lombardo, C. Sbriziolo, G. Viscardi, and P. Quagliotto, “Kinetic evidence for the solubilization of pyridine-2-azo-p-dimethylaniline in alkanediyl-alpha,omega-bis(dimethylcetylammonium nitrate) surfactants. Role of the spacer chain length,” *New J. Chem.*, vol. 28, no. 7, pp. 793–799, 2004.

[95] M. Yoshimura, S.-W. Song, K.-S. Han, “Effect of 20°–200^o C Fabrication Temperature on Microstructure of Hydrothermally Prepared $LiCoO_2$

Films," *Journal of the American Ceramic Society.*, vol. 83, no.11, pp. 2839–2844, 2000.

[96] V. G. Hadjiev, M. N. Iliev, I. V Vergilov, D. P. L. J. and T. G. Bremard C, P. H. and M. J. P, R. W. L, B. R. P. and P. S. P. S. Rousseau D L, and M. Y. and N. I. Shirai H, "The Raman spectra of Co_3O_4," *J. Phys. C Solid State Phys.*, vol. 21, no. 7, pp. L199–L201, 1988.

[97] D. J. Lockwood, G. Mischler, M. C. Schmidt, and I. W. Johnstone, "Raman scattering from electronic excitations and phonons in paramagnetic and antiferromagnetic $CoBr_2$," *J. Phys. C Solid State Phys.*, vol. 12, no. 10, pp. 1955–1975, 1979.

[98] H. C. Choi, Y. M. Jung, I. Noda, and S. Bin Kim, "A Study of the Mechanism of the Electrochemical Reaction of Lithium with CoO by Two-Dimensional Soft X-ray Absorption Spectroscopy (2D XAS), 2D Raman, and 2D Heterospectral XAS−Raman Correlation Analysis," *J. Phys. Chem. B*, vol. 107, no. 24, pp. 5806–5811, 2003.

[99] Z. Wang, X. Huang, and L. Chen, "Performance Improvement of Surface-Modified LiCoO[sub 2] Cathode Materials: An Infrared Absorption and X-Ray Photoelectron Spectroscopic Investigation," *J. Electrochem. Soc.*, vol. 150, no. 2, p. A199, 2003.

[100] (2016). *Vacuum Deposition Techniques and Tables for thin film applications.* Available: https://www.tedpella.com/company_html/Vacuum-Deposition-Techniques-and-Tables.htm

[101] W. Li, M. Zhang, J. Zhang, and Y. Han, "Self-assembly of cetyl trimethylammonium bromide in ethanol-water mixtures," *Front. Chem. China*, vol. 1, no. 4, pp. 438–442, 2006.

[102] A. M. Khedr, M. M. Abou-Sekkina, and F. G. El-Metwaly, "Synthesis, Structure, and Electrochemistry of Sm-Modified $LiMn_2O_4$ Cathode Materials for Lithium-Ion Batteries." *J. of Electronic Materials*, vol. 42, no. 6, pp. 1275–1281, 2013.

[103] C. V. Ramana, M. Massot, and C. M. Julien, "XPS and Raman spectroscopic characterization of $LiMn_2O_4$ spinels," *Surf. Interface Anal.*, vol. 37, pp. 412–416, 2005.